Development of a Wireless MEMS Multifunction Sensor System and Field Demonstration of Embedded Sensors for Monitoring Concrete Pavements

Volume II - Development of a Wireless MEMS Multifunction Sensor (WMS) System for Concrete Pavement Health Monitoring

August 2016

National Concrete Pavement Technology Center

Tech Center

IOWA STATE UNIVERSITY
Institute for Transportation

Sponsored by
Iowa Highway Research Board
(IHRB Project TR-637)
Iowa Department of Transportation
(InTrans Project 12-417)

About ProSPER

The overall goal of the Program for Sustainable Pavement Engineering and Research (ProSPER) is to advance research, education, and technology transfer in the area of sustainable highway and airport pavement infrastructure systems.

About the National CP Tech Center

The mission of the National Concrete Pavement Technology (CP Tech) Center is to unite key transportation stakeholders around the central goal of advancing concrete pavement technology through research, tech transfer, and technology implementation.

About InTrans

The mission of the Institute for Transportation (InTrans) at Iowa State University is to develop and implement innovative methods, materials, and technologies for improving transportation efficiency, safety, reliability, and sustainability while improving the learning environment of students, faculty, and staff in transportation-related fields.

Disclaimer Notice

The contents of this report reflect the views of the authors, who are responsible for the facts and the accuracy of the information presented herein. The opinions, findings and conclusions expressed in this publication are those of the authors and not necessarily those of the sponsors.

The sponsors assume no liability for the contents or use of the information contained in this document. This report does not constitute a standard, specification, or regulation.

The sponsors do not endorse products or manufacturers. Trademarks or manufacturers' names appear in this report only because they are considered essential to the objective of the document.

Non-Discrimination Statement

Iowa State University does not discriminate on the basis of race, color, age, ethnicity, religion, national origin, pregnancy, sexual orientation, gender identity, genetic information, sex, marital status, disability, or status as a U.S. veteran. Inquiries regarding non-discrimination policies may be directed to Office of Equal Opportunity, Title IX/ADA Coordinator, and Affirmative Action Officer, 3350 Beardshear Hall, Ames, Iowa 50011, 515-294-7612, email eooffice@iastate.edu.

Iowa Department of Transportation Statements

Federal and state laws prohibit employment and/or public accommodation discrimination on the basis of age, color, creed, disability, gender identity, national origin, pregnancy, race, religion, sex, sexual orientation or veteran's status. If you believe you have been discriminated against, please contact the Iowa Civil Rights Commission at 800-457-4416 or Iowa Department of Transportation's affirmative action officer. If you need accommodations because of a disability to access the Iowa Department of Transportation's services, contact the agency's affirmative action officer at 800-262-0003.

The preparation of this report was financed in part through funds provided by the Iowa Department of Transportation through its "Second Revised Agreement for the Management of Research Conducted by Iowa State University for the Iowa Department of Transportation" and its amendments.

The opinions, findings, and conclusions expressed in this publication are those of the authors and not necessarily those of the Iowa Department of Transportation.

Technical Report Documentation Page

1. Report No.	2. Government Accession No.	3. Recipient's Catalog No.
IHRB Project TR-637		

4. Title and Subtitle	5. Report Date
Development of a Wireless MEMS Multifunction Sensor System and Field Demonstration of Embedded Sensors for Monitoring Concrete Pavements: Volume II - Development of a Wireless MEMS Multifunction Sensor (WMS) System for Concrete Pavement Health Monitoring	August 2016
	6. Performing Organization Code

7. Author(s)	8. Performing Organization Report No.
Halil Ceylan (orcid.org/0000-0003-1133-0366), Liang Dong (orcid.org/0000-0002-0967-4955), Yueyi Jiao (orcid.org/0000-0002-8264-5771), Seval Yavas (orcid.org/0000-0002-4173-2633), Shuo Yang (orcid.org/0000-0002-2653-5199), Sunghwan Kim (orcid.org/0000-0002-1239-2350), Kasthurirangan Gopalakrishnan (orcid.org/0000-0001-8346-5580), and Peter C. Taylor (orcid.org/0000-0002-4030-1727)	InTrans Project 12-417

9. Performing Organization Name and Address	10. Work Unit No. (TRAIS)
Institute for Transportation Iowa State University 2711 South Loop Drive, Suite 4700 Ames, IA 50010-8664	**11. Contract or Grant No.**

12. Sponsoring Organization Name and Address	13. Type of Report and Period Covered
Iowa Highway Research Board Iowa Department of Transportation 800 Lincoln Way Ames, IA 50010	Final Report Volume II
	14. Sponsoring Agency Code IHRB Project TR-637

15. Supplementary Notes

Visit www.intrans.iastate.edu for color pdfs of this and other research reports.

16. Abstract

This two-pronged study evaluated the performance of commercial off-the-shelf (COTS) micro-electromechanical sensors and systems (MEMS) embedded in concrete pavement (Final Report Volume I) and developed a wireless MEMS multifunctional sensor system for health monitoring of pavement systems (Final Report Volume II).

The Volume I report focused on the evaluation of COTS MEMS sensors embedded in concrete pavement sections. The Volume II report covers the set of MEMS sensors that were developed as single-sensing units for measuring moisture, temperature, strain, and pressure. These included the following sensors: (1) nanofiber-based moisture sensors, (2) graphene oxide (GO)–based moisture sensors, (3) flexible graphene strain sensors with liquid metal, (4) graphene strain and pressure sensors, (5) three-dimensional (3D) planar and helical structured graphene strain sensors, (6) temperature sensors, and (7) water content sensors. In addition, the MEMS temperature sensors and the MEMS water content sensors were integrated into one sensing unit as a multifunctional sensor. A wireless signal transmission system was built for MEMS sensor signal readings. Characterization of the sensors was conducted and sensor responses were analyzed using different applications. The sensors developed were installed and tested inside concrete. The results demonstrated the capability to detect sensor response changes at the installed locations.

17. Key Words	18. Distribution Statement
concrete pavements—pavement health monitoring—MEMS—multifunctional sensor system	No restrictions.

19. Security Classification (of this report)	20. Security Classification (of this page)	21. No. of Pages	22. Price
Unclassified.	Unclassified.	101	NA

Form DOT F 1700.7 (8-72) **Reproduction of completed page authorized**

DEVELOPMENT OF A WIRELESS MEMS MULTIFUNCTION SENSOR SYSTEM AND FIELD DEMONSTRATION OF EMBEDDED SENSORS FOR MONITORING CONCRETE PAVEMENTS: VOLUME II - DEVELOPMENT OF A WIRELESS MEMS MULTIFUNCTION SENSOR (WMS) SYSTEM FOR CONCRETE PAVEMENT HEALTH MONITORING

Final Report
August 2016

Principal Investigator
Halil Ceylan, Professor, Civil, Construction, and Environmental Engineering (CCEE)
Director, Program for Sustainable Pavement Engineering and Research (PROSPER)
Institute for Transportation, Iowa State University

Co-Principal Investigators
Liang Dong, Associate Professor, Electrical and Computer Engineering
Kasthurirangan Gopalakrishnan, Research Associate Professor, CCEE
Sunghwan Kim, Research Scientist, CCEE
Iowa State University

Peter C. Taylor, Director
National Concrete Pavement Technology Center, Iowa State University

Research Assistants
Yueyi Jiao, Seval Yavas, and Shuo Yang

Authors
Halil Ceylan, Liang Dong, Yueyi Jiao, Seval Yavas, Shuo Yang, Sunghwan Kim, Kasthurirangan Gopalakrishnan, and Peter Taylor

Sponsored by
the Iowa Highway Research Board and
the Iowa Department of Transportation (IHRB Project TR-637)

Preparation of this report was financed in part
through funds provided by the Iowa Department of Transportation
through its Research Management Agreement with the
Institute for Transportation (InTrans Project 12-417)

A report from
Institute for Transportation
Iowa State University
2711 South Loop Drive, Suite 4700
Ames, IA 50010-8664
Phone: 515-294-8103 / Fax: 515-294-0467
www.intrans.iastate.edu

TABLE OF CONTENTS

LIST OF FIGURES

LIST OF TABLES

ACKNOWLEDGMENTS

The authors would like to thank the Iowa Highway Research Board (IHRB) and the Iowa Department of Transportation (DOT) for sponsoring this research. The project technical advisory committee (TAC) members from the Iowa DOT and the Federal Highway Administration (FHWA), including Ahmad Abu-Hawash, Chris Brakke, Mark Dunn, Vanessa Goetz, Todd Hanson, Lisa McDaniel, Kevin D. Merryman, and Robert (Bob) Younie, are gratefully acknowledged for their guidance, support, and direction throughout the research.

The research team would also like to thank Bob Steffes with the National Concrete Pavement Technology (CP Tech) Center and many graduate and undergraduate students in the Departments of Electrical and Computer Engineering (ECpE) and Civil, Construction, and Environmental Engineering (CCEE) at Iowa State University for their assistance with the laboratory and field tests. Special thanks go to the Higher Education Council and Anadolu University in Turkey for financial support of Seval Oren throughout her Ph.D. study.

EXECUTIVE SUMMARY

The primary objectives of this two-pronged research study were (1) to deploy some promising commercial off-the-shelf (COTS) micro-electromechanical sensors and systems (MEMS) developed for monitoring concrete pavements in a live field project and (2) to develop a wireless MEMS multifunction sensor (WMS) system capable of real-time remote monitoring of strain, moisture content, and temperature in pavement concrete. Accordingly, two final report volumes have been prepared targeting each of these objectives:

- The Volume I final report focused on the deployment and field evaluation of COTS MEMS sensors.
- This Volume II final report describes the development of a WMS system for concrete pavement health monitoring.

This report (Volume II) describes the design, fabrication, and characterization of MEMS sensors for concrete pavement structural health monitoring to fulfill the second objective of this study: to develop a WMS system capable of real-time remote monitoring of strain, moisture content, and temperature in pavement concrete.

Multiple types of sensors were developed, tested, and demonstrated in the laboratory, and some were installed in concrete/mortar for trial applications. The water content sensor and the temperature sensor were combined to achieve simultaneous multifunctional sensing. Moreover, a graphene-based strain sensor installed in a concrete cylinder for real-time loading testing is described in this report, which comprehensively records the whole process of idea generation, problem solving, and the achievement of the target during the development of the MEMS-based sensors.

Seven types of MEMS sensors were developed during this study and are described in this report:

- The nanofiber-based moisture sensor was constructed using poly(methyl methacrylate) (PMMA) nanofibers to fabricate a planar capacitive moisture sensor that has a quick response time.

- The graphene oxide–based moisture sensor was constructed using the simple fabrication method of forming large-area graphene oxide (GO) thin films.

- The flexible graphene strain sensor took advantage of the high piezoresistance of graphene and the flexibility of liquid metal and polydimethylsiloxane (PDMS) to achieve full sensor flexibility.

- The graphene-based strain sensor and the graphene-based pressure sensor were fabricated by applying patterned graphene to scotch tape and then transferring the patterned graphene to another adhesive tape, which made both sensors capable of application to any flexible object.

- The microfluidic patterned three-dimensional (3D) graphene sensor overcame limitations related to the complexity of fabricating patterned graphene film and did so at a low cost.

- The different sizes of MEMS-based temperature sensors developed in this research can be used either as single sensors or as part of a multifunctional sensor system. The temperature and water content sensor uses a straightforward structure to simplify the fabrication process and retain a good sensor response while lowering the cost.

All sensors were tested in a laboratory environment; the resulting performance, the discovery and development of the sensors, and the sensor testing are described in this report.

This report also describes the demonstration of these sensors in a concrete application. The moisture and water content multifunctional sensor was installed and tested in mortar samples, and the readings of temperature and water content were found to be consistent with the mortar samples' testing environment. The graphene-based strain sensor was installed both inside and outside (at the surface) of a concrete cylinder, and its readings demonstrated the typical deformation behavior of the concrete cylinder under vertical pressure. The conclusive result of the development of the graphene-based sensor was a smart sensing system capable of sending an electrical signal wirelessly from the concrete to a laptop.

INTRODUCTION

Background

Micro-electromechanical sensors and systems (MEMS) are technologies that use microfabrication techniques to produce devices or special structures (MNX 2016). There are three major categories of MEMS devices: sensors, actuators, and passive structures (Maluf 2000). MEMS technology takes advantage of advanced materials characteristics and modifies current existing technology to improve fabrication or sensing. For example, graphene is a highly piezoelectric material, so its electrical resistance changes greatly when under pressure; this change in value is fixed due to the material's properties. MEMS researchers/manufacturers take advantage of graphene's high piezoelectricity to design and fabricate sensors using microfabrication technology; graphene material can in this way be used as a pressure sensor. Design and analysis of the proper shape and thickness of graphene at desired sizes involves MEMS technology, as does the patterning and shaping of graphene on a desired substrate. In general, the MEMS fabrication process applies materials to real applications by using microfabrication technology. Overall, a MEMS-based monitoring system provides an opportunity to make sensing faster and more sensitive and to make fabrication easier and more energy-efficient while lowering the cost.

MEMS sensors can collect environmental information by measuring mechanical, electrical, thermal, biological, chemical, optical, and magnetic signals (Electronics Engineering Herald 2006). These sensors are becoming increasingly important for control and feedback applications. In recent years, MEMS technology has been used to develop sensors in systems ranging from automotive, consumer, industrial, and life sciences applications to defense applications. Current examples of MEMS devices include accelerometers for airbag sensors, pressure sensors, radio frequency (RF) MEMS devices, blood and tire pressure sensors, optical switches, and analytical components (Van Heeren and Salomon 2007). Recent MEMs technology provides many advantages over traditional sensing technologies in applications that require smaller sizes, lower costs, adaptability to large-scale fabrication, and greater complexity.

Research Objectives

Multi-sensor systems are promising in that they have the potential to monitor structural health and to support the efficient operation and maintenance of civil infrastructure through the simultaneous measurement of multiple properties. The primary objectives of this research were twofold:

- Deploy some promising off-the-shelf MEMS sensors developed for monitoring concrete pavements in a live field project (focus of the Volume I final report)

- Develop a wireless MEMS multifunction sensor (WMS) system capable of real-time remote monitoring of strain, moisture content, and temperature in pavement concrete (focus of this Volume II report)

Volume II Report Content

The Volume II final report presents detailed information on the research efforts fulfilling the second objective of this project: Develop a WMS system capable of real-time, remote monitoring of strain, moisture content, and temperature in pavement concrete. This report includes the following chapters:

- **Chapter 1: MEMS-Based Moisture Sensors.** A description of the development and testing of MEMS-based moisture sensors
- **Chapter 2: MEMS-Based Strain Sensors.** A description of the development and testing of MEMS-based strain sensors
- **Chapter 3: MEMS-Based Temperature Sensors.** A description of the development of MEMS-based temperature sensors
- **Chapter 4: Prototypes of MEMS Sensor Systems.** A description of the development and testing of a MEMS multifunctional sensor system for temperature and water content measurement, including a wireless MEMS strain sensor system
- **Chapter 5: Summary and Recommendations.** A summary of the important findings and recommendations from this study

MEMS-BASED MOISTURE SENSORS

Nanofiber-Based Moisture Sensors

Summary of the Work

A moisture capacitive sensor using electrospun poly(methyl methacrylate) (PMMA) nanofibers as a novel moisture-sensitive dielectric material was developed. The sensor is formed by depositing multiple layers of PMMA nanofibers on planar interdigital microelectrodes (IDEs). The porous PMMA nanofibers provide a large surface-area-to-volume ratio to achieve efficient and rapid interactions with the surrounding environment, thus promoting the fibers' dielectric property response to environmental moisture changes. Compared to conventionally cast PMMA film-based moisture sensors, the new sensor has a higher sensitivity and shorter response time. A demonstration was conducted that showed that as the concentration of PMMA in a precursor polymer decreases, the PMMA product of electrospinning experiences a morphological transition from microfibers to microbelts and, ultimately, to nanofibers. The following work was conducted:

- Applied the nanofiber structure to both moisture and temperature multifunction MEMS sensors
- Developed a microfabrication protocol suitable for large-scale manufacturing
- Developed a novel moisture sensing nanomaterial of PMMA nanofibers with improved sensitivity, faster response time, and longer lifetime
- Achieved MEMS moisture sensors having a response two to three times faster than that of commercial moisture sensors, with sensitivity comparable to that of state-of-the-art sensors

Literature Review

High-sensitivity and fast-response moisture sensors are in high demand in environmental monitoring and assessment. Based on transducing principles, moisture sensors are categorized into capacitive, resistive, mechanical, oscillating, and thermo-electrical types (Kim et al. 2009). The capacitive detection method is often used to provide a wide detection range of moisture; it relies on measuring changes in the electrical impedance of a moisture-sensitive dielectric material deposited on the surface of a planar interdigitated capacitor (Kim et al. 2009; Zambrozi and Fruett 2012). A list of common moisture-sensitive dielectric materials includes different ceramic materials (e.g., aluminum [Al] oxide and titanium oxide [Chen and Lu 2005]) and polymers (e.g., PMMA, polyimide [Kim et al. 2009; Chatzandroulis et al. 2002; Starke et al. 2011], polycarbonate, cellulose acetate, and polyester [Shi et al. 2008]). These materials have been widely used in the form of casted films for moisture sensor applications. The recent advances in nanotechnology support the creation of nanostructures such as nano-pores (Shi et al. 2008) and nano-posts inside some of these materials to improve moisture sensor sensitivity (Wu and Brett 2001). For example, PMMA has a high water absorption rate, about 2% water by volume. Its dielectric characteristic is affected by the amount of water absorbed (Malshe et al. 2011). It has been demonstrated that, due to the presence of nano-sized pores, nanoporous

PMMA (Shi et al. 2008) can not only absorb and hold more water content than a casted counterpart, but can also provide an increased interfacial contact area between the material and surrounding air (Wu and Brett 2001), thus improving sensor performance.

Electrospinning is a simple and efficient approach for producing porous polymer nanofibers. This method utilizes a high-strength electric field to draw a charged polymer solution into a liquid jet. As the solvent in the liquid jet evaporates, solid polymer nanofibers are formed and collected on a collector. Electrospun nanofibers feature a large surface-area-to-volume ratio, a nanoporous structure, and high material diversity. These features have been deployed extensively in applications such as gas sensing, water and air filtration, tissue engineering, and energy harvesting. The amount of research in the field of electrospun nanofibers is rapidly growing.

Based on the above literature review, the development of a high-performance moisture sensor exploring the use of electrospun PMMA nanofibers as moisture-sensitive material is described in the following section. The sensor is formed by simply depositing multiple layers of PMMA nanofibers on microfabricated interdigital electrodes. Electrospun PMMA nanofibers provide a porous network of interconnected air pores with a large surface area to promote efficient absorption of water molecules in air. In addition to improved sensitivity, the sensor is also expected to have a short response time because the nano-pores embedded inside the PMMA nanofibers can help water molecules enter the nanofibers and influence the dielectric properties of PMMA. To the best of the researchers' knowledge based on the reported literature, this is the first time a moisture sensor has been constructed using PMMA nanofibers as moisture-sensitive material.

Development of the Moisture Sensor

Stage 1: Using Poly(acrylic acid) (PAA) Cantilever for Moisture Sensing

Four generations of moisture sensor designs were developed. By simplifying the design stage-by-stage without changing the working principle, the dual objectives of cost-effective fabrication and shortening of the fabrication procedure were achieved.

In the first generation of the design, a sandwich capacitor structure was developed, as shown in Figure 1. As the relative humidity (RH) changes in the environment, water-sensitive material changes the shape of the SU-8 cantilever. This change leads to a change in the distance between the two electron pads, so a capacitance change can be detected. A design concept sketch is shown in Figure 1.

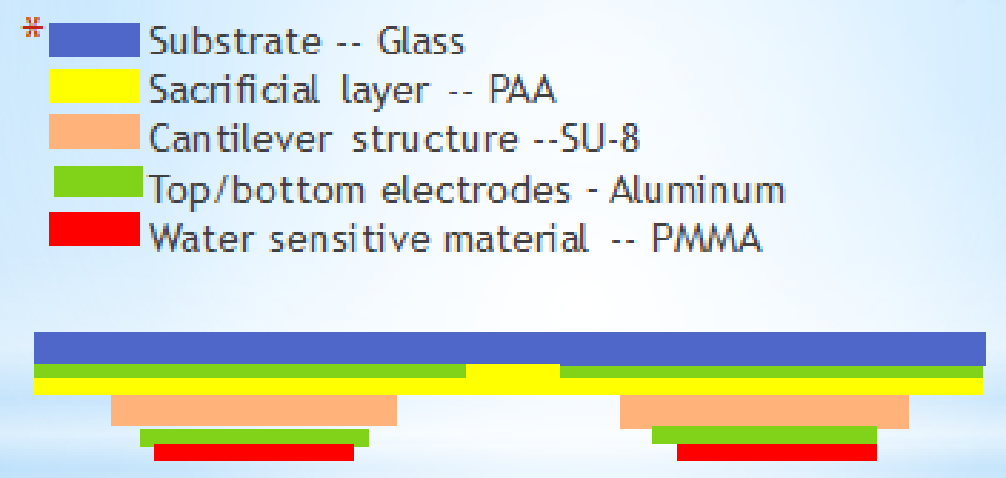

Figure 1. Concept design of Generation 1 MEMS moisture sensor

Each layer of the masks was successfully designed and fabricated using the printed masks.

In the first generation of the design, all layers were grown on one side of a glass slide layer by layer, thus producing a six-layer structure on the glass slide. Fabrication results are shown in Figure 2. The single glass slide can produce 30 functional capacitors, but a long routine is required to implement the entire procedure. Also, the thick layers are easy to etch off during the fabrication process. To produce a better deliverable result and facilitate fabrication, the design plan was moved to the second generation.

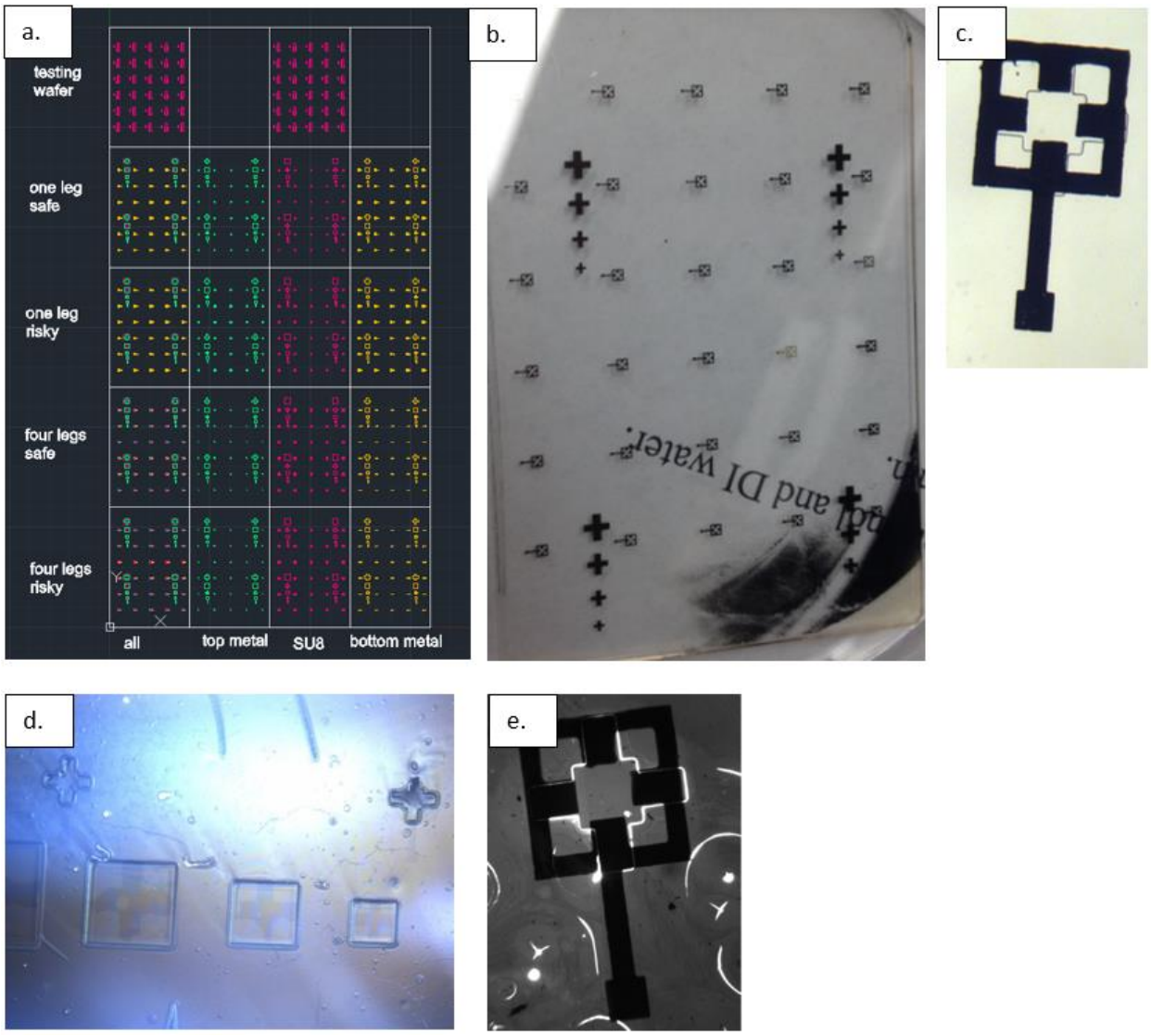

Figure 2. Fabrication results of Generation 1 MEMS moisture sensor: (a) mask design of Generation 1; (b) aluminum (bottom electrons) layer of Generation 1; (c) aluminum layer (bottom electrons) + sacrificial layer (PAA) + SU-8 (cantilever layer) of Generation 1; (d) first aluminum layer (bottom electrons) + sacrificial layer (PAA) + SU-8 (cantilever layer) + second aluminum layer (top electrons) of Generation 1; (e) all layers without etched top aluminum layer for Generation 1

The parameters used for making the device for Generation 1 are as follows:

- Bottom electrodes (Al) thickness:100 nm
- Sacrificial layer (PAA) thickness: 20 µm
- Cantilever layer (SU-8) thickness: 20 µm
- Bottom electrodes (Al) thickness: 100.2 nm
- PMMA layer: 6%, ~2 µm

In Generation 2, fabrication process was changed from growing on only one side of the glass slide to two-sided growing. The principle is that the two pieces of the device are built separately, and conductive SU-8 is then used to stick them together. The conceptual structure is shown in Figure 3.

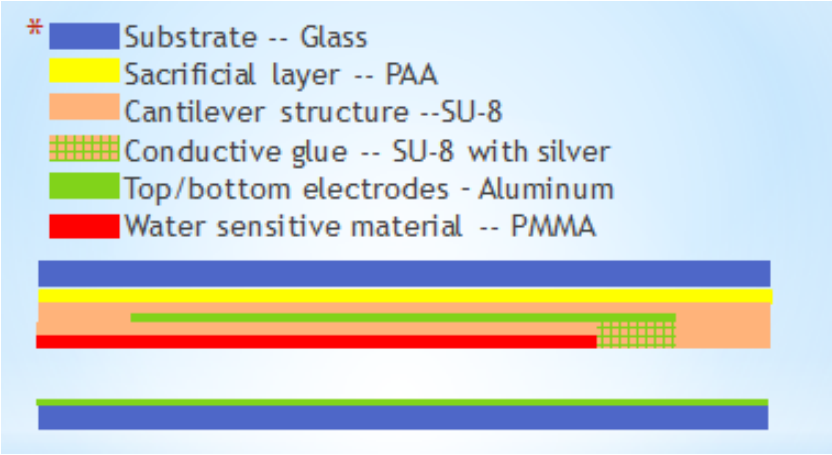

Figure 3. Conceptual design of Generation 2 MEMS moisture sensor

In this design, the PAA sacrificial layer becomes the peeling-off media. With its water soluble property, the top structure can easily be removed from the glass substrate and stuck onto another substrate. This generation of design shares the same mask with the previous generation. Figure 4 shows the peeling-off testing and the stickiness testing of the second design.

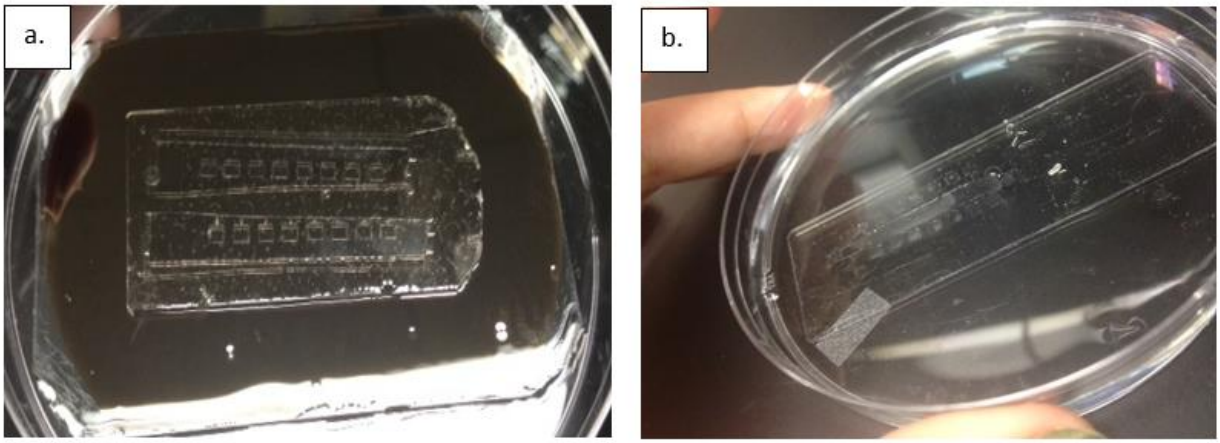

Figure 4. Testing of Generation 2 MEMS moisture sensor: (a) stickiness testing, (b) peeling-off test

From the test results of the second generation MEMS moisture sensor, it was observed that the stickiness of the conductive SU-8 behaved less perfectly than desired, so the third generation of the structure was developed.

The parameters used for making the MEMS moisture sensor device for Generation 2 were as follows:

- Sacrificial layer thickness: 20 μm
- SU-8 layer on PAA thickness: 40 μm
- Structure size: 3 mm × 3 mm square
- Al-coated substrate thickness: 1000 Å
- Sticky SU-8 thickness: 25 μm

To solve the stickiness problem in the top electrode, the plan was revised to use an easier method, referred to as the imprinting technique. The principle is that by fabricating an angled isobornyl acrylate (IBA) mode as the stamp, imprinting the stamp on the liquid state moisture-sensitive layer (PMMA) creates holes that allow the top electrons to come into contact with the substrate pattern. The cross-sectional representation is provided in Figure 5.

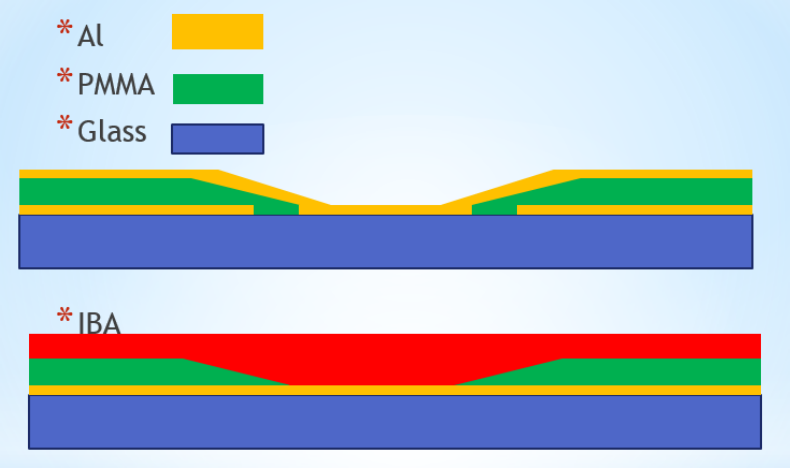

Figure 5. Concept design of Generation 3 MEMS moisture sensor

In this design, one more mask was designed for each layer's pattern, as shown in Figure 6. Each color represents one layer of the device, and there are four designs.

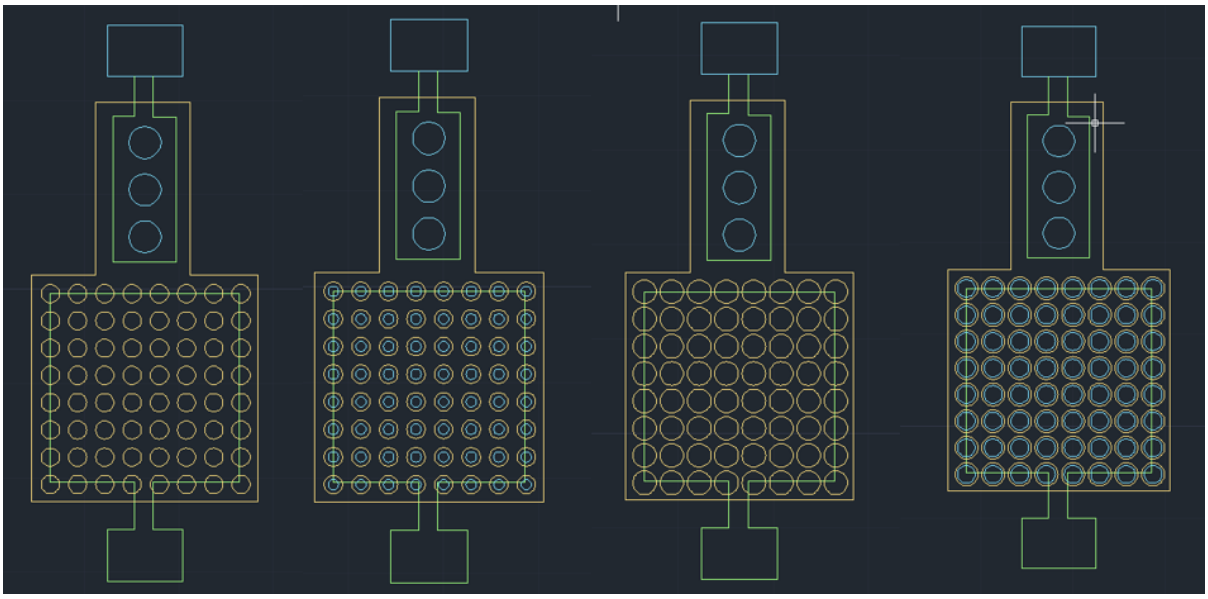

Figure 6. Mask designs of Generation 3 MEMS moisture sensor

The imprinting the two layers was also conceptually tested. By involving an ozone plasma surface treatment and diode testing, PMMA removal from an aluminum-coated glass surface was performed with a high percentage of success. Figure 7 shows the imprinting process.

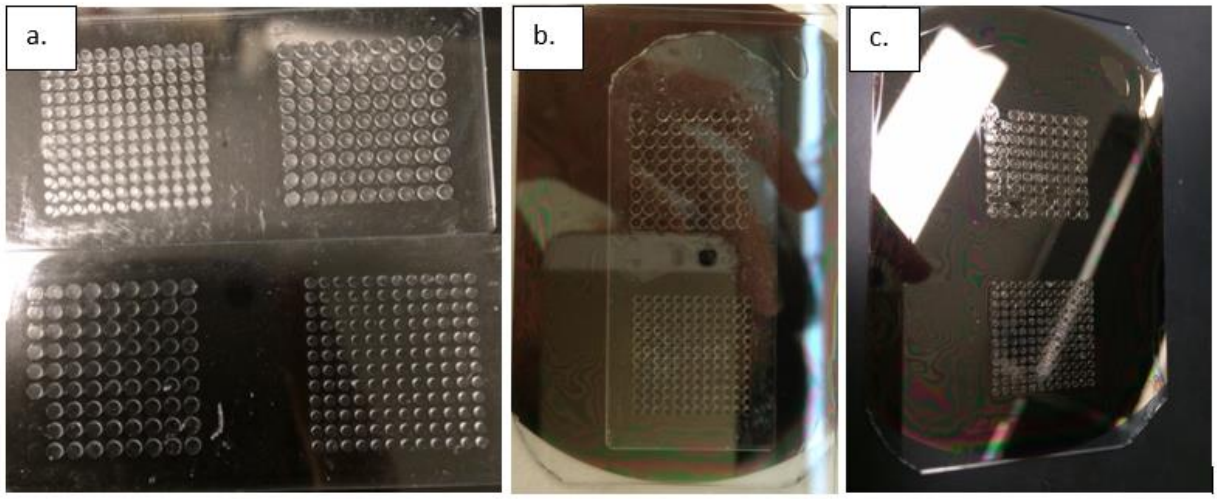

Figure 7. Imprinting process of Generation 3 MEMS moisture sensor: (a) stamp fabrication, (b) imprinting, and (c) plasma burning

Figure 7(a) shows the different sizes of IBA stamps, Figure 7(b) shows the moisture-sensitive material (PMMA) coating the Al under the imprinting process, and Figure 7(c) shows the stamps being removed to leave the remaining patterns. The parameters used for making the Generation 3 MEMS moisture sensor were as follows:

- Al coated substrate: 1000 Å
- Stamp (IBA) structure size: 5 mm radius circle and 3.5 mm radius circle
- Moist sensitive material thickness: 2 μm
- Ozone plasma etching time: 50 minutes

To solve the problem of poor bonding of the top aluminum layer, the sandwich capacitor structure used in the first three generations of design was switched to an interdigital capacitor structure. Using interdigital capacitors, also called planar capacitors, three fabrication steps were combined into one step. By applying this new design, both materials and fabrication time were saved. The concept design of the Generation 4 MEMS moisture sensor is shown in Figure 8.

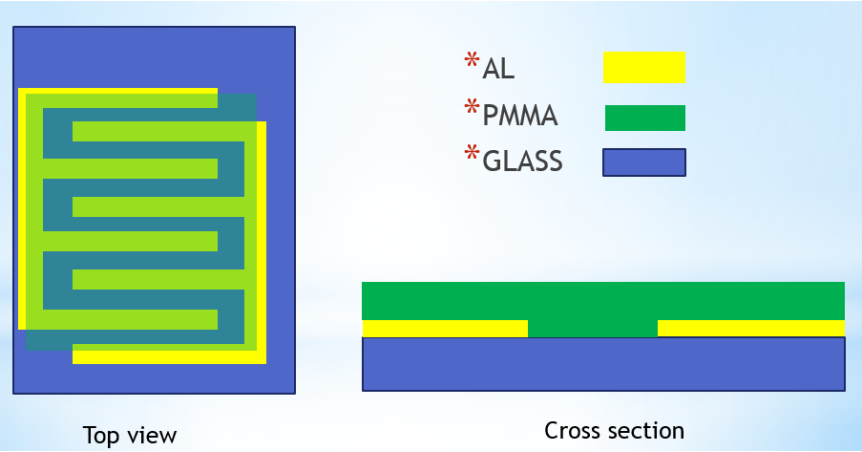

Figure 8. Concept design of Generation 4 MEMS moisture sensor

The mask design for the planar capacitor was also completed, as shown in Figure 9. The green lines outline the shape of the bottom aluminum layer.

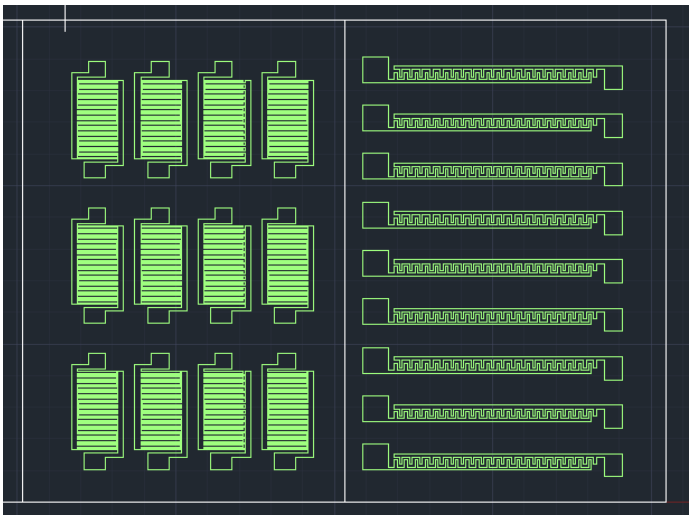

Figure 9. Mask design of Generation 4 MEMS moisture sensor

The proposed device relies on surface micromachining techniques to release the moveable mechanical structures of MEMS sensors. A novel, cost-effective polymer-based surface micromachining technique was developed that has the benefit of completing the whole device fabrication flow at room temperature with low-cost manufacturing equipment and facilities outside of a clean room; more conventional surface micromachining approaches require expensive equipment and facilities inside a clean room and generally require high processing temperatures (e.g., 1000°C during the deposition of oxide as a sacrificial layer).

The proposed device has a flexible membrane that supports both a moisture-sensitive and a temperature-sensitive element. A process was developed that allows the manufacturing of flexible membranes using a negative tone photoresist (SU-8).

By combining the aforementioned polymer-based surface micromachining with flexible SU-8 membrane techniques, a suspended MEMS cantilever structure was achieved as the key to the success of the proposed project. Details of the fabrication process are described below. First, a mixture of PAA (Polysciences, Inc.), dextran (Sigma-Aldrich), and NaOH (Sigma-Aldrich) is formed at a weighing ratio of 19: 5.6: 20. The mixture is then spin-coated on top of the plasma-treated glass slide at a speed of 1000 rpm for 15 seconds, leading to the formation of a 20 µm thick water soluble sacrificial layer. Once the sacrificial layer has been dried out at 120°C on a hotplate, negative photoresist SU-8 (MicroChem Corp.) is spin-coated on top of the sacrificial layer at a speed of 500 rpm for 5 seconds and then 3000 rpm for 30 seconds. This results in the formation of a 15 µm thick SU-8 structural layer. Subsequently, the SU-8 membrane is patterned using ultraviolet (UV) photolithography. Finally, the SU-8 structures are released by removing the PAA using water, forming the flexible membranes (Figure 10 and Figure 11).

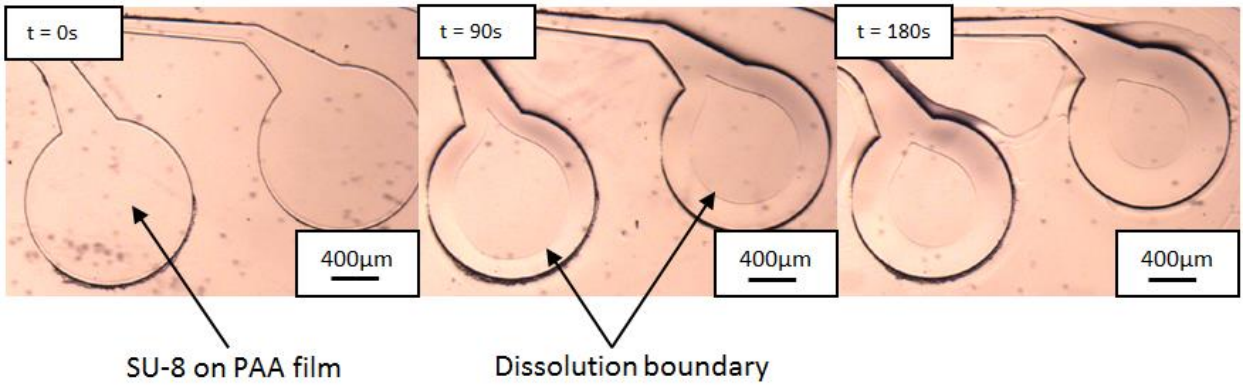

Figure 10. Novel polymer-based surface micromachining process, with MEMS structures formed by gradual removal of a soluble layer beneath the plate

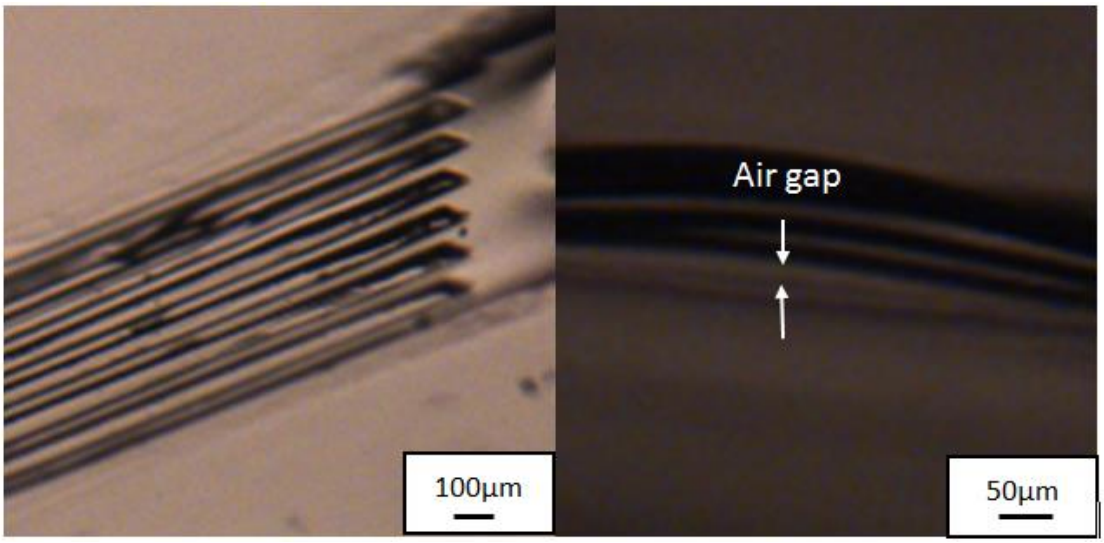

Figure 11. MEMS cantilever

Polymeric and membrane layers were formed using the novel surface machining technique described above; these two structures are the key components of the proposed MEMS sensor. In this stage of the development of the moisture sensor, the geometrical parameters of the device were determined and fabricated (see Figure 12 and Table 1).

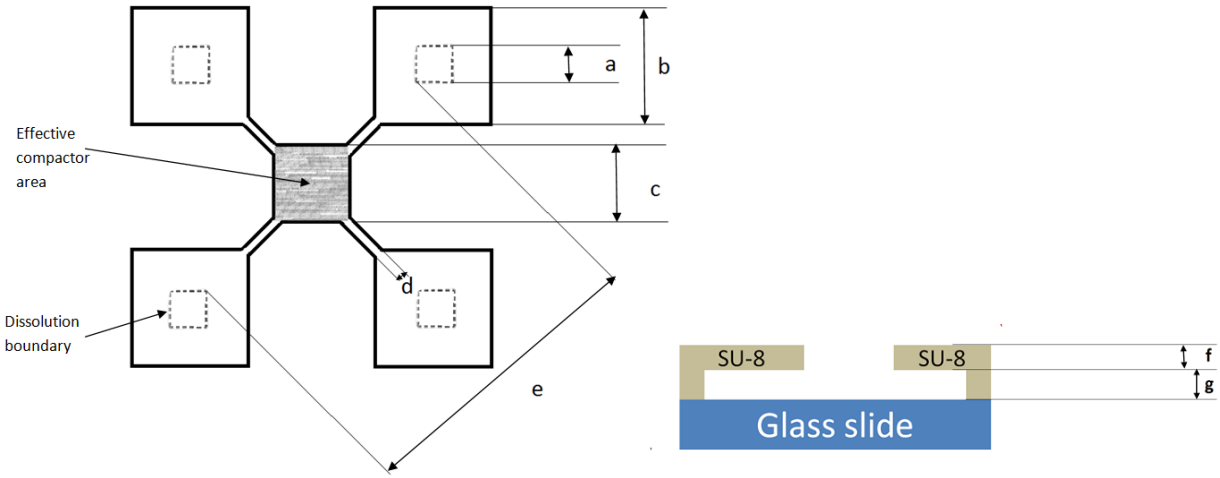

Figure 12. Top view of a typical moisture sensor

Table 1. Geometrical parameters in Figure 12

Part	Description	Length (μm)
a	Sacrificial layer boundary side length	140
b	Point holder side wall length	425
c	Capacitor side length	25
d	Supporting membrane width	40
e	Cantilever holder distance	1000
f	SU-8 cantilever thickness	15
g	Distance of cantilever to substrate	20

Stage 2: Using PMMA Fibers as a Moisture-Sensitive Material

In this stage, a novel relative humidity/moisture sensor using PMMA fibers on interdigital capacitor electrodes was developed and tested. Nanofibers were successfully fabricated with a low concentration of PMMA solution. The diameter and shape of the fibers at different concentrations were studied using scanning electron microscopy (SEM) photographs. The reaction speed of the developed moisture sensor is three seconds, which is quicker than most conventional moisture sensors. The capacitance is linearly proportional to environmental humidity level, and the rate is not affected by temperature.

Figure 13 shows the interdigital planar structure.

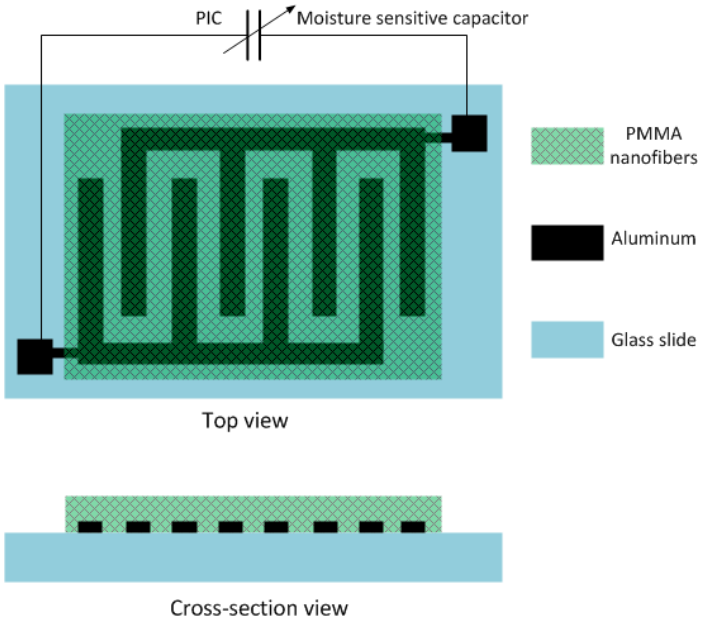

Figure 13. Schematic design of the interdigital planar structure

This structure is easy to fabricate, and a large surface area of interaction with water molecules was achieved using a porous electrospun nanofibrous mat.

The first version of the mask design is shown in Figure 14.

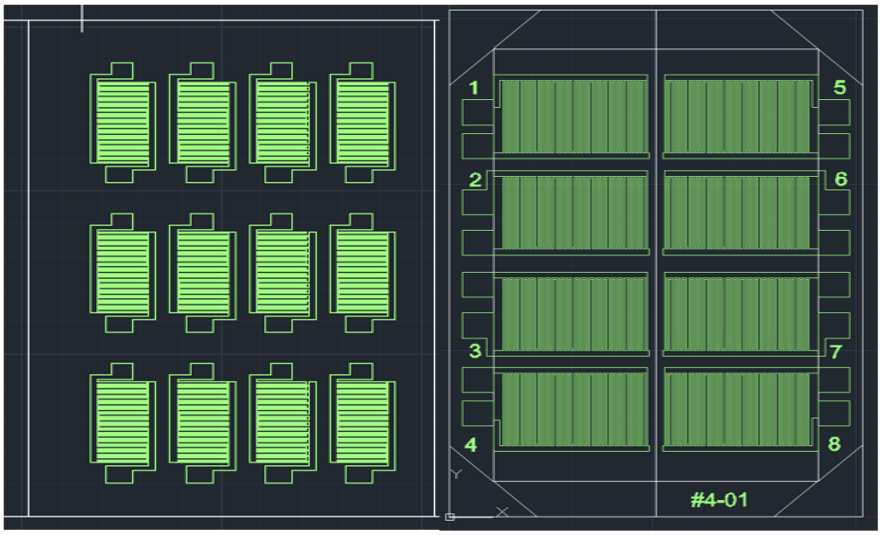

Figure 14. Photomask design of the planar interdigital capacitor moisture sensor

The photomasks for the planar interdigital capacitor (PIC) moisture sensors were designed using AutoCAD software, and the photomasks were manufactured at the University of Minnesota. The number and lengths of the electrode fingers were increased to increase the total capacitance, producing a change in the capacitance of the device to support easy electrical measurement.

For comparison purposes, Figure 15 shows the three masks designed.

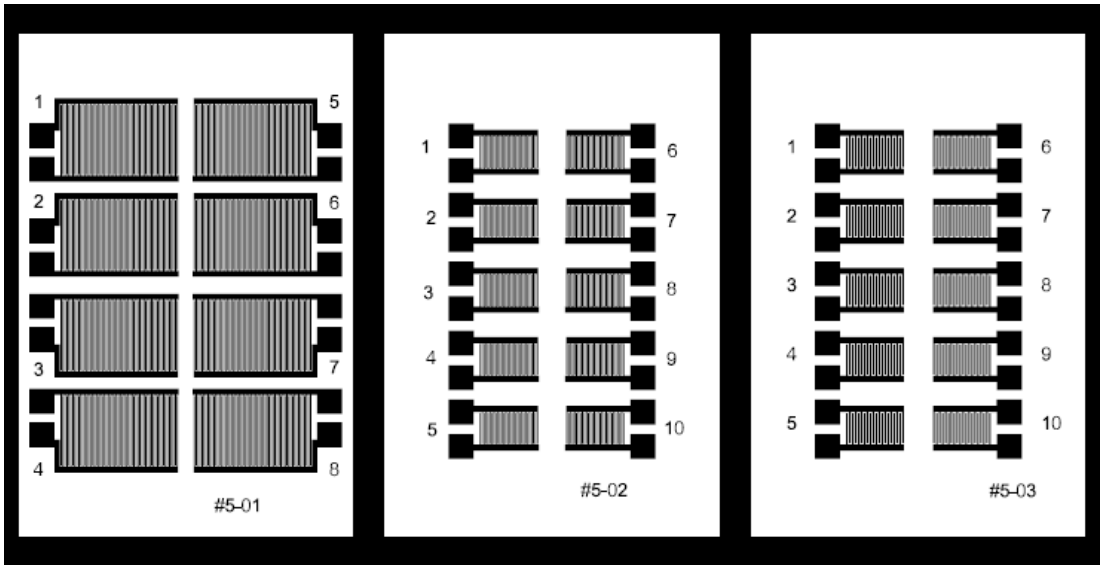

Figure 15. Mask design of the interdigital planar structure

The first mask (#5-01) uses the same single device size as the other masks, but with a higher electrode density. The second mask (#5-02) provides a smaller device size (1/4 of the original size). The third mask (#5-03) provides the same device size as the second mask, but the single finger width feature size is equal to that of the first mask.

A fabrication process for the interdigital electrodes was also developed (Figure 16) that used the following steps:

- Substrates were prepared at Iowa State University's Microelectronics Research Center (MRC). Preparation included the following steps:
    - Standard cleaning (2% HCl and deionized [DI] water)
    - Use of evaporation to coat 100 nm thick Al film on the surface of glass slides
- Al electrodes were patterned in the laboratory using the following procedure:
    - Bake before spin coating for 5 minutes at 95°C.
    - Spin coat hexamethyldisilazane (HDMS) for 5 seconds at 500 rpm and then for 45 seconds at 4000 rpm.
    - Spin coat AZ 5214 photoresist (EMD Performance Materials) for 5 seconds at 500 rpm and then for 45 seconds at 4000 rpm.
    - Pre-bake at 95°C for 45 seconds.
    - Expose to UV light at an intensity of 8 mW/cm^2.
    - Post-bake for 3 minutes at 90ºC.
    - Immerse the slides into developer for 3 minutes.
    - Immerse the slides into aluminum etchant for 4 minutes.
    - Rinse with DI water.
    - Remove any remaining photoresist using ethanol.

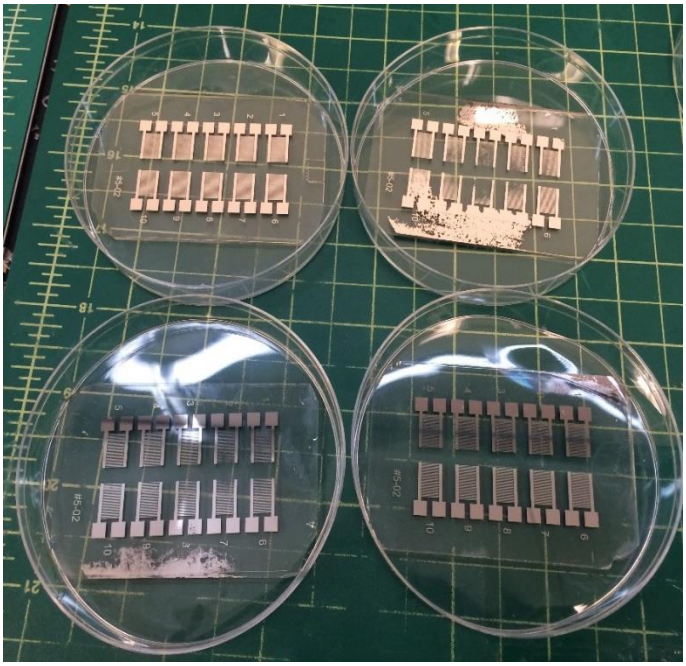

Figure 16. Fabrication of interdigital planar electrodes

An electrospinning fabrication process for the nanofibers was also developed in this stage (Figure 17 and Figure 18).

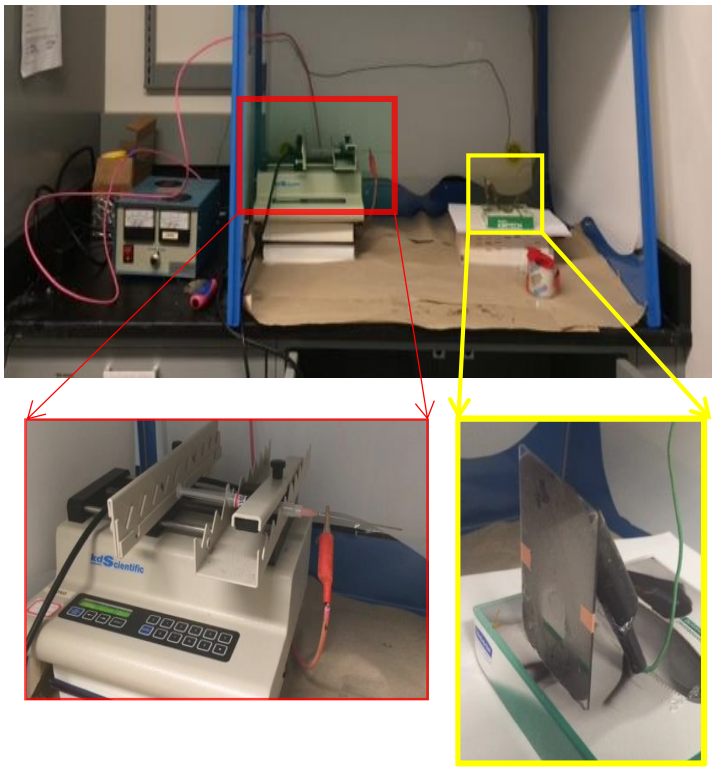

Figure 17. Setup of the electrospinning process for nanofiber fabrication

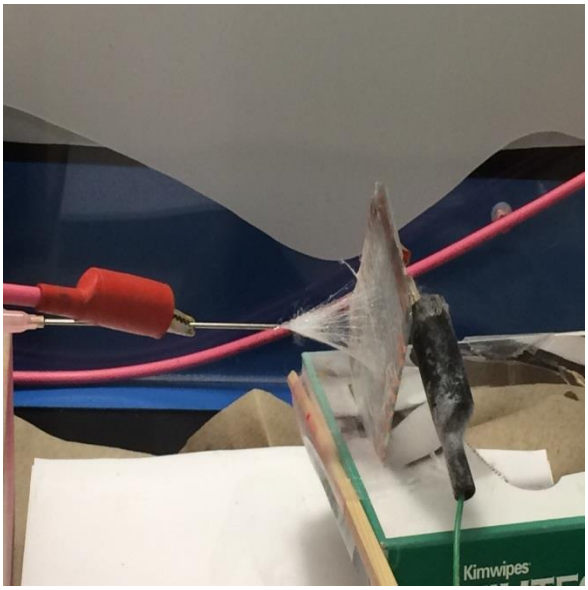

Figure 18. Electrospinning process for nanofiber fabrication

The materials and characteristics of the electrospinning fabrication process were as follows:

- Speed: Pumping rate of 800 µm/hour
- Voltage: 18 kV
- Syringe: 0.7 mm × 25 mm Luer-Lok PrecisionGlide needle (Fisher Scientific)
- Material: 11% 950 PMMA in acetone
- Deposition distance: 6 cm
- Fiber collector: Al-coated glass

After all of the fiber was collected, the transient response was measured to test the sensor's response to humidity. Transient testing was conducted using an oscilloscope and LabVIEW signal processing software.

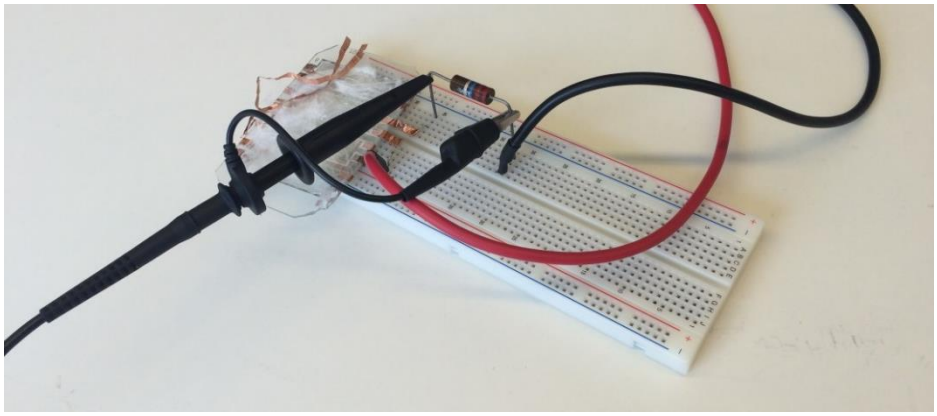

Figure 19. Testing of the moisture sensor

A square-wave signal was generated using a function generator and displayed on an oscilloscope (Figure 20).

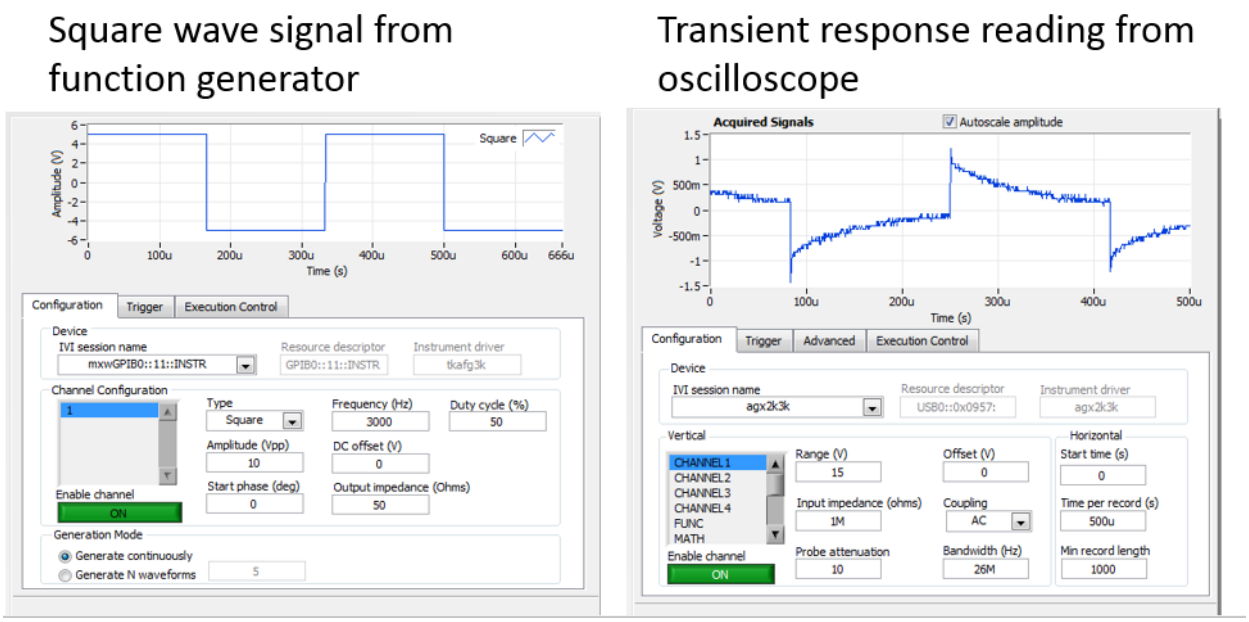

Figure 20. Parameters of function generator and oscilloscope for transient response testing

Using $q = Q_0 e^{-\frac{t}{RC}}$ to describe the charging process of the developed capacitive moisture sensor, a time constant $\tau = RC$ was read from the square-wave signal voltage response (Figure 21).

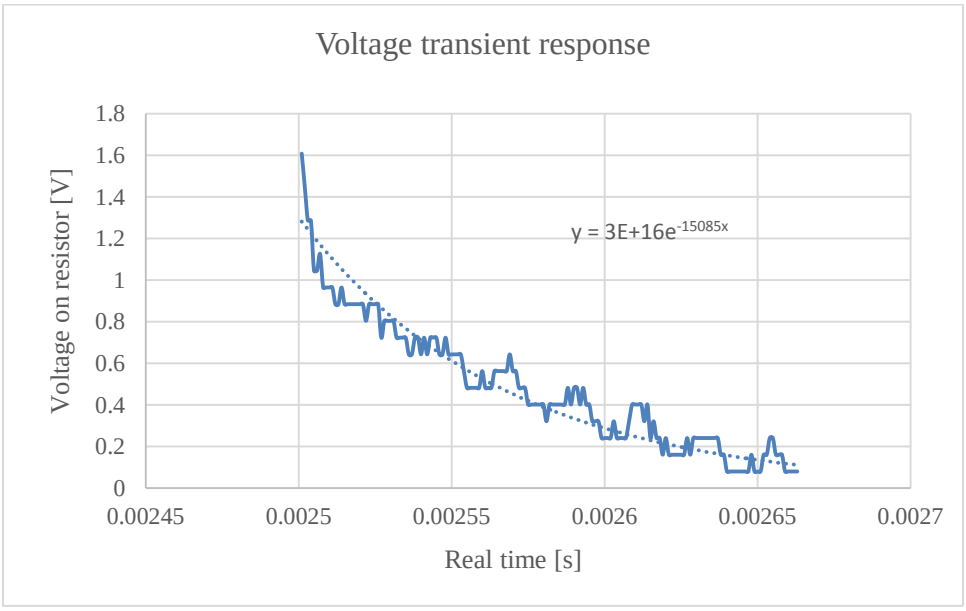

Figure 21. Voltage transient signal received from breadboard testing setup for the capacitive relative humidity sensor

The transient response time reflects the reaction time of a device when it transitions to a new environment with a different moisture level. The average transient response time of the device tested was about 3.5 seconds (Figure 22).

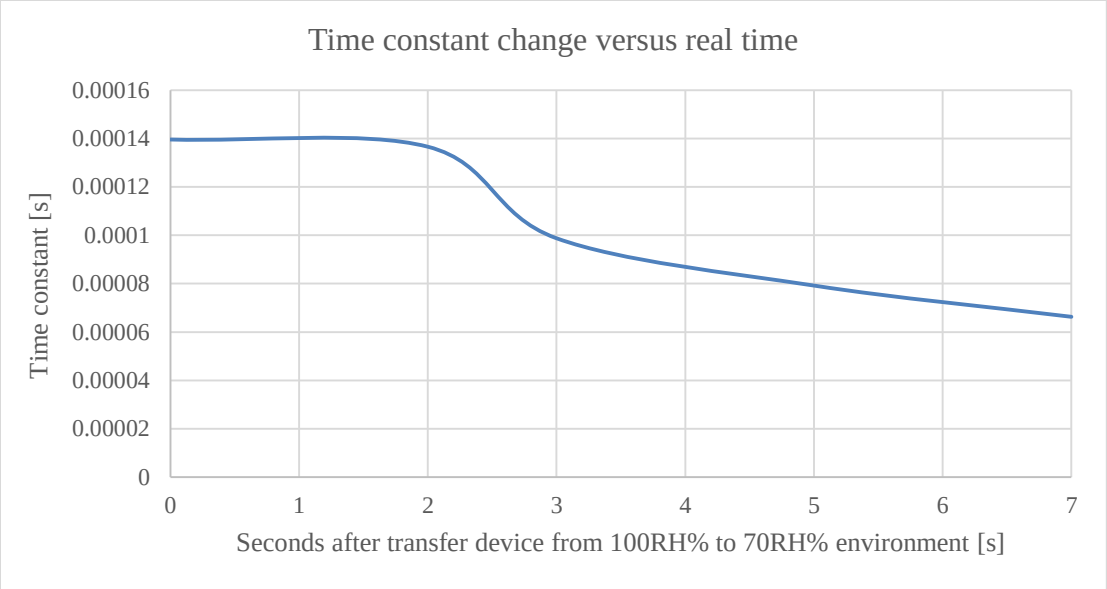

Figure 22. Real-time response of the capacitive sensor

Capacitance versus humidity was also tested at different temperatures. It was found that the capacitance linearly increased with the environmental relative humidity and that the ratio of capacitance change to relative humidity was constant at all working temperatures.

Moisture sensors with a PMMA nanofibrous mat and cast film, respectively, were developed to demonstrate the effectiveness of the nanofibers as a sensing material. In the results shown in Figure 23, it can be seen that the use of PMMA nanofibers leads to a higher capacitance change than the use of conventional cast film.

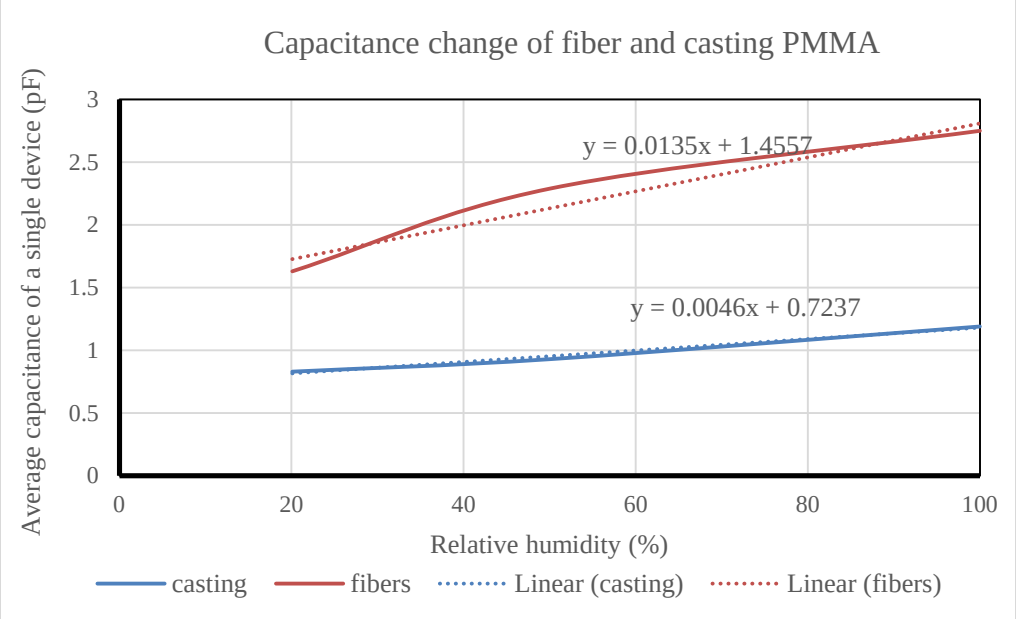

Figure 23. Comparison of capacitance versus relative humidity for the film casting and nanofiber coating methods

Capacitance changed 13.5 pF in response to a change of 1% in relative humidity.

Key Findings and Results

Small-diameter PMMA nanofibers are required to obtain a high surface-area-to-volume ratio for maximal interfacial contact with air. PMMA has high mechanical strength and a Young's modulus that makes it difficult to form nanofibers using electrospinning. The formation of nanofibers using electrospinning is sensitive to many factors, including solvent type, the concentration and molecular weight of the polymer, the viscosity and feeding rate of the polymer solution, electric field strength, environmental temperature, and humidity. Given a polymer and solvent system, the concentration of the polymer in the precursor solution and the electric field strength are often more critical than other parameters in determining the morphologies of electrospun products. For example, when the deposition voltage is fixed at 18 kV, no obvious difference in fibers is observed when the deposition distance decreases from 6 cm to 4 cm.

PMMA precursor solutions with various concentrations were prepared by dissolving different amounts of PMMA powder (molecular weight 350000, Sigma-Aldrich) in pure acetone (Sigma-Aldrich) at room temperature for 12 hours. All air bubbles were removed from the mixed solution prior to loading it into a 3 mL syringe (BD Biosciences). The collector was an Al-coated glass slide (50 mm × 75 mm, Corning) serving as an electrical ground. The syringe was attached to a syringe pump (KDS210, Kd Scientific, Inc.). A stainless steel flat-tip needle (18 gauge, Howard Electronic Instruments, Inc.) was screwed onto the syringe and connected to a high-voltage power supply (Gamma High Voltage Research, Inc.). A direct current (DC) voltage of 18 kV was applied between the collector and the needle spaced at a distance of 6 cm. The feeding rate of the polymer precursor solution was set to 800 µL/hour.

Figure 24 shows different fiber morphologies resulting from varying the concentration of the precursor PMMA solution (CPMMA).

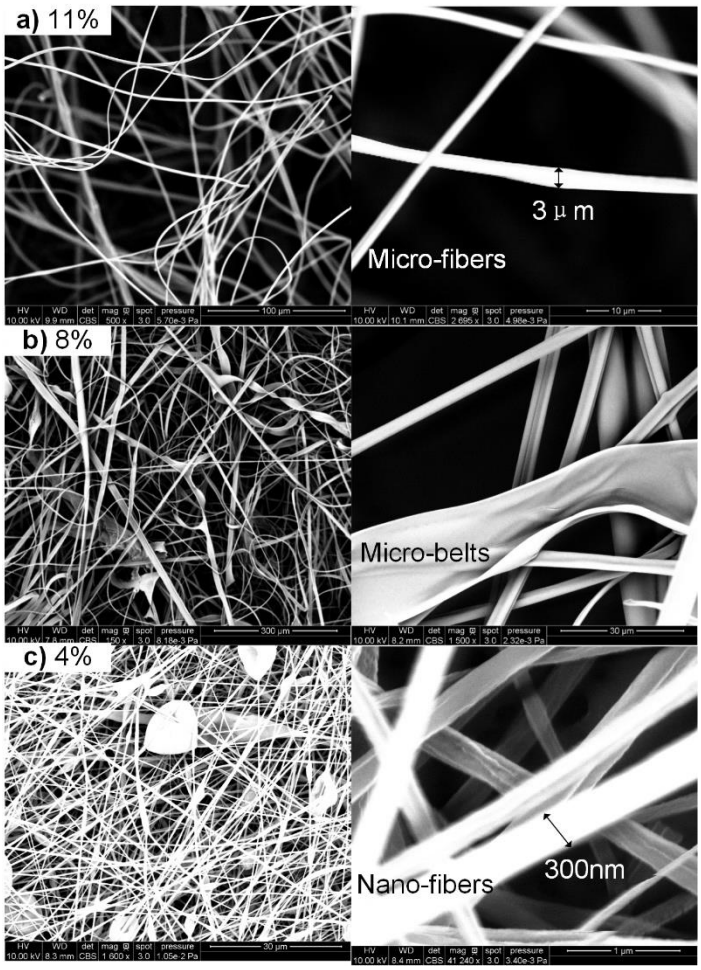

Figure 24. (a) Microfibers with a diameter of 3 μm produced by 11% PMMA; (b) microbelts with a belt width of 30 μm and a belt thickness of 1 μm produced by 8% PMMA; (c) nanofibers with a diameter of 300 nm produced by 4% PMMA

The shapes of the electrospun products were expressed as microfibers, microbelts, and nanofibers. Varying the concentration of the precursor PMMA had the following results:

- When CPMMA > 20%, the solution was too viscous to flow from the needle, and the needle became clogged.
- When 8% < CPMMA < 20%, mixed microfibers were formed.
- When 4% < CPMMA < 8%, microbelts were formed.
- When the concentration was reduced to 4%, nanofibers were formed.
- When CPMMA < 4%, the precursor solution was not viscous enough to form a Taylor cone, and the solution dropped directly onto the collector.

The capacitive moisture sensor was formed using two interdigitated electrodes covered with PMMA nanofibers. Capacitance between the two electrodes was measured, with the overall capacitance of the sensor influenced by the permittivity change in the nanofibers due to changes in air moisture (Rahman et al. 2014). The capacitance C can be calculated as the capacitance between two parallel aluminum lines related to the electrical field lines passing though the polymide layer (Laconte et al. 2003):

$$C_{PMMA} = \frac{n\,\varepsilon_{PI}\,l\,h_{fingers}}{W_{gap}} + \frac{nl\varepsilon_{PMMA}}{2} \quad (1)$$

The sensor capacitance is determined by the sensor dimensions, the permittivity of the dielectric material, and other parameters used in fabrication. In this design, the gap W_{gap} between two electrode fingers was 150 μm, the overlapping length of the electrode pair l was 6 mm, the aluminum layer thickness $h_{fingers}$ was 100 nm, and there were 60 electrodes. If the fact that the surface is covered by PMMA is taken into consideration and the relative permittivity of PMMA $\varepsilon_{PMMA} = 4.9$ (Thomas et al. 2012) is included in equation (1), C_{PMMA} = 0.782 pF is obtained. Due to the electrical field lines passing through the insulator layer, this design also had a significant parasitic capacitance, which can be obtained as follows (Laconte et al. 2003):

$$C_{parasitic} = \frac{nl\varepsilon_{glass}}{2}\alpha\left(L, t_{glass}\right) \quad (2)$$

where α is a proportionality factor expressing the repartition of electrical field lines between the layers and the thickness of the insulator layer. In a theoretical calculation of parasitic capacitance, $C_{parasitic}$ was measured as 1.2 pF. Because C_{PMMA} is parallel to $C_{parasitic}$, in theory if all of the surface layers are covered by PMMA, the total capacitance of the sensor should be $C_{total,\ \text{theory}} = C_{parasitic} + C_{PMMA,\ theory} = 1.982$ pF. In reality, the measured $C_{total,\ \text{real}}$ was 1.5 pF at room temperature. This capacitance differed from the previously calculated value because of the nature of the constructed three-dimensional (3D) mats of PMMA on the surface; to be exact, about $1 - \frac{C_{total,\ \text{theory}} - C_{total,\ \text{real}}}{C_{PMMA}} = 39\%$ of the volume was filled by air.

A fiber collector was fabricated by following a standard device fabrication process. First, a 100 nm thick aluminum layer was deposited onto a glass substrate. Spin-coated layers of adhesion (HDMS) and photoresist (AZ) were then formed at a speed of 500 rpm for 5 seconds and 4,500 rpm for 45 seconds, respectively. The electrodes were then subjected to UV exposure with an intensity of 8 for 24 seconds, and the exposed area of photoresist was developed in AZ developer solution for 90 seconds. The last step was to etch out the unprotected aluminum layer using aluminum etching solution for 60 seconds. Once the aluminum electrodes were fabricated and cleaned, the sensor substrate was prepared for the fiber fabrication step (Figure 25).

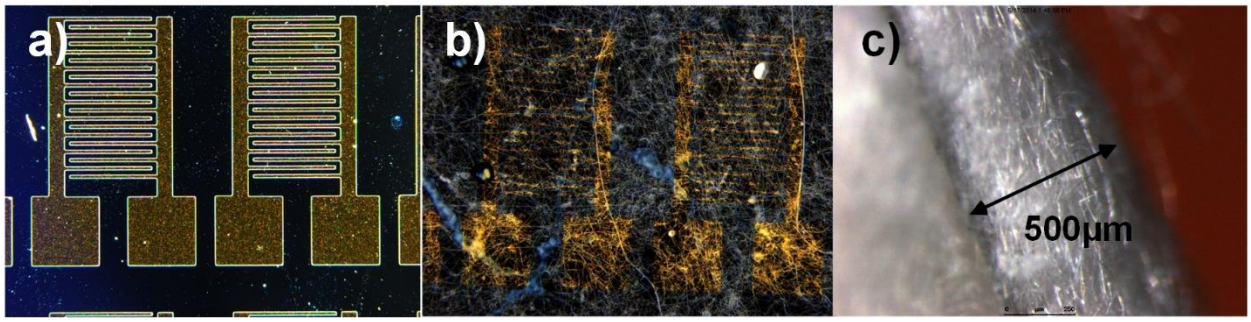

Figure 25. Fabrication of relative humidity sensors: (a) Interdigitated electrodes with a feature size of 150 µm (without fibers covered on), (b) interdigitated electrodes covered with fibers, (c) cross-section of the 3D PMMA fiber mat constructed on electrodes with a thickness of 500 µm

An inductance, capacitance, and resistance (LCR) meter was used to measure capacitance at different RH values. To create a dry environment as the base RH, drying particles were placed in the chamber, and real-time RH information was read from a commercial RH sensor (Extech RH101: Hygro-Thermometer + InfraRed Thermometer, Extech Instruments). To study the sensitivity of the sensor to RH, a graded moisture level environment was created by blowing different amounts of wet air (100% RH) into the closed dry base environment.

Figure 26 shows that the sensor's capacitance has a linear relationship to the RH of the air.

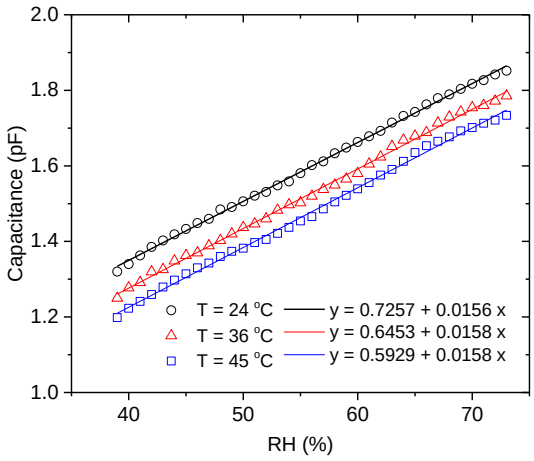

Figure 26. Capacitance of sensor with respect to relative humidity at 24, 36, and 45°C

The relative humidity level was controlled in the range of 35% to 75%. The slope of its linear fitting indicates an approximately 0.157 pF (0.156 pF at 24°C, 0.158 pF at 36°C, and 0.158 pF at 45°C) rise in capacitance for every 1% RH change. Because the linear fits at three temperatures (at 24, 36 and 45 ºC) are all parallel, it can be concluded that the sensitivity of this sensor is independent of temperature. The intersection of the fitting lines and the y-axis sets the capacitance base value at each temperature: the higher the temperature, the smaller the capacitance.

To understand the influence of temperature on the sensor response, the capacitance of the sensor was recorded at different temperatures. To explain the results, the concepts of the moisture content of air and the relative humidity of air should be distinguished. At a constant environmental pressure, RH can be calculated by dividing the maximum amount of potential moisture that can be contained in the air by the amount of moisture in the air. Warm air has a greater potential to hold water vapor than air at room temperature. Relative humidity is the ratio of two pressures, as follows: RH = 100% $\times p/p_s$, where p is the actual pressure of the ambient water vapor present and p_s is the saturation pressure of water at the ambient temperature (Rotronic Instrument Corp. 2005; Lawrence 2005). The relative humidity sensor was exposed to air during laboratory testing, so the detected air pressure (p) due to moisture can be treated as a constant. As shown in Figure 27, the sensor's capacitance is linearly proportional to RH and has a negative slope, meaning that, with moisture being constant, an increase in heat leads to a decrease in RH. In the equation RH = p/p_s, the saturation pressure ($p_{s)}$ depends on temperature, such that a warmer environment experiences a greater saturation of air pressure. Therefore, an increase in heat decreases RH and capacitance in an open space (Rotronic Instrument Corp. 2005).

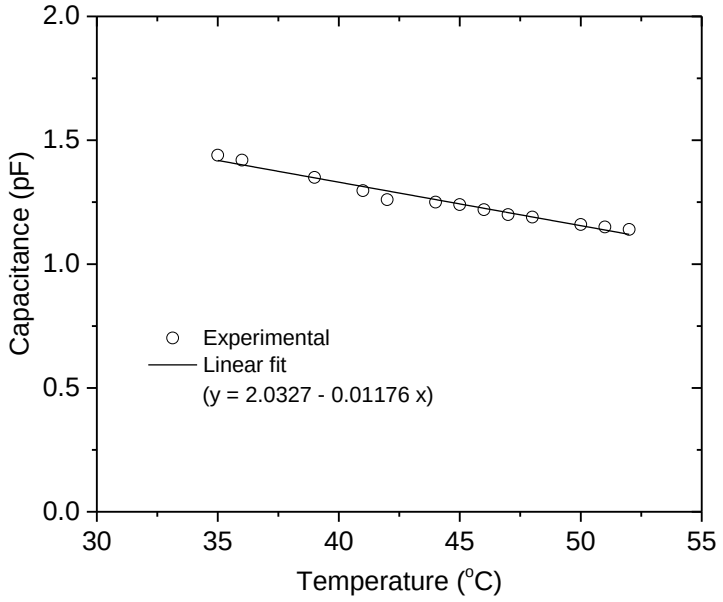

Figure 27. Dependence of sensor capacitance on temperature in an environment with constant moisture

The transient response of the sensor was also determined. The sensor's transient response time corresponds to the reaction speed of the sensor. To determine transient response time, the sensor was transferred from a testing chamber with an RH of 38% to a chamber with an RH of 43%. As shown in Figure 28 , the sensor took about 10 seconds to register the change and stabilize.

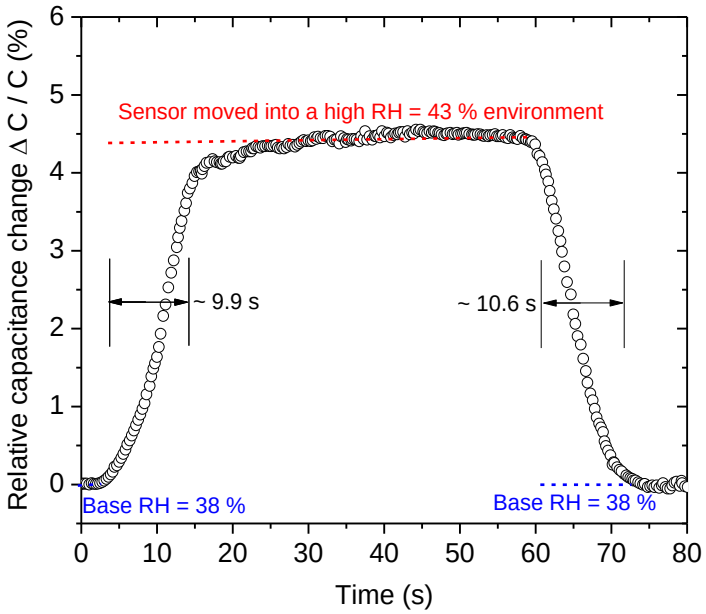

Figure 28. Transient response of sensor capacitance at 26°C

For comparison, a traditional casted polymer film sensor was also fabricated and tested. The test showed that the casted film sensor consumed three times more dielectric material than the electrospinning-fabricated fiber sensor to achieve the same reaction speed and sensitivity. In summary, the electrospinning-fabricated PMMA sensor uses less material without sacrificing high sensitivity and fast reaction speed. These benefits are due to the porous structure of the polymer fibers. Nanofibers are used to construct a 3D mat, and this mat increases the chances of PMMA interacting with moisture in air. Due to the larger area of contact with moist air, the reaction speed of the sensor is also improved over more traditional sensors.

Despite the sensor's fast response and high sensitivity, there is room for further improvement. A further sensitivity improvement is expected by electrospinning a thicker layer of PMMA nanofibers and increasing the size of the capacitor, but the uniformity of the electric field that is created during the electrospinning process becomes troublesome when the fiber collector is a large wafer. If only a single spinneret (positive electrode) is applied at the top of the collector, the center of the fiber collector (ground pole) experiences a stronger electric field than its surroundings. This difference occurs because the edges of the wafer have longer distances to the spinneret than the center of the wafer. The larger the wafer, the bigger the electric field difference us. This problem can be solved using multi-jet electrospinning (Lin 2011) or a drum rotatory fiber collector technique (Kumar 2012).

The morphology of the fiber also affects the stability of the sensor. During RH measurement, the capacitance change (ΔC) is detected by an electric field (generated between the electrode fingers) passing through the dielectric material (PMMA fibers), and any morphology change in the top layer of the fibers is detected by the capacitance signal. To minimize the influence described

above, a sensor with very thick layers of PMMA fibers can be fabricated. The farther the fibers are from the electrodes, the smaller the influence is. Table 2 compares the newly developed moisture sensor with other sensors in terms of sensitivity, response time, materials, and technology.

Table 2. Comparison of the developed sensor and other existing moisture sensors

No.	Sensitivity @ 65% RH (percentage/RH%)	Response time (seconds)	Material	Technology	Reference
Developed sensor	1.3%	10	PMMA nanofibers	Electrospinning	
1	2.05%	40	Etched polyimide	Spin coating	Kim et al. 2009
2	0.153%	N/A	Polymide layer	Spin coating	Laconte et al. 2003
3	2.6%	110	Six layers of polymide	Printing	Starke et al. 2011
4	0.128%	N/A	Capillary wicking polyimide	Spin coating	Lazarus et al. 2010
5	0.011%	20	Micro-air-bridge	Micromachining	Fang et al. 2004
6	4.58%	120	Nanoporous polycarbonate	N/A	Shi et al. 2008
7	3.75%	300	Nanoporous cellulose acetate membrane	Casting ultrasonicated solution	Shi et al. 2008, Kim et al. 2013
8	4.16%	180	Nanoporous nylon	Electrospinning	Shi et al. 2008, Shi et al. 2011
9	0.17%	N/A	Polymide on silicon (Si) cantilever	Semiconductor thin film deposition	Chatzandroulis et al. 2002
10	3.42%	7	Porous alumina/ aluminum oxide (Al_2O_3) film	Anodic Spark Deposition	Kovac et al. 1977

Overall, polymer materials dominate the core materials for the moisture sensors, because their sensitivity is comparably higher than air-based sensors. Spin coating and deposition of film are the most used fabrication techniques for producing moisture sensors, but nano-structured sensors have better sensitivity than traditional film-based sensors. Nanoporous membrane–structured sensors have high sensitivity but require minutes of transient time for signal stabilization. Sensors based on aluminum oxide porous film have high sensitivity and fast response, but they require a high temperature created by a large instantaneous current density ($10^4 A/cm^2$) during fabrication (Kovac et al. 1977). The sensor developed in this study exhibits a quick response, relatively high sensitivity, and a cost-effective fabrication process.

Graphene Oxide–Based Moisture Sensor

Summary of Work

A simple fabrication method for forming large-area graphene oxide (GO) thin films was developed that used spinning-assisted spray coating (SSC) to apply a GO dispersion onto wafer surfaces and thus produce GO-based moisture sensors. By combining spray coating with a spinning process, this method overcomes the limitation of existing spray coating methods, which only support small-area fabrication. The importance of spinning a substrate during spraying is that it suffuses the coating material uniformly over the whole surface of the substrate. The key processing parameters of the method were investigated, including the vertical distance between the airbrush and the substrate, the pressure of the air source, and the spinning speed of the substrate. The optimization of these parameters allowed the spraying of a GO dispersion onto the wafer's center while spreading it towards the wafer's edges without any spillover. To demonstrate the application of moisture sensor based on large-area GO films, a GO-based humidity sensor on an 8 in. silicon wafer was developed. Impedance analysis showed that the sensor exhibited a high sensitivity to humidity with a short transient response time and good repeatability.

Literature Review

Graphene and its related materials (e.g., GO) have attracted increasing interest for use in many sensor applications due to the materials' exceptional optical, electrical, mechanical, and chemical properties and their high surface-area-to-volume ratio (Yao et al. 2012a). GO has oxygen-containing functional groups such as epoxy, hydroxyl, and carboxyl groups, providing tunability of the material's electronic and mechanical properties (Mkhoyan et al. 2009). This allows GO to be used in forming different sensors for the detection of humidity, gas, strain, stress, and biochemical species (Bi et al. 2013, Yao et al. 2012b). For example, Zhao et al. (2011) developed an interdigital capacitive humidity sensor using graphene oxide as a sensing material, and that sensor displayed higher sensitivity and a faster response than a sensor based on polyimide (Zhao et al. 2011). Dua et al. (2010) used inkjet-printed reduced graphene oxide to detect Cl_2 and NO_2 (Dua et al. 2010). Shan et al. (2010) reported the first graphene-based glucose biosensor to exhibit wide linear glucose response, good reproducibility, and high stability (Shan et al. 2010). Wang et al. (2009) fabricated a graphene-based electrode for the selective determination of dopamine (Wang et al. 2009). In addition, Mei and Zhang (2012) used GO as the energy donor in

a fluorescence resonance energy transfer (FRET) sensor for the visual detection of a variety of biomolecules (Mei and Zhang 2012).

The dispersion behavior of GO in water and many other solvents allows it to be deposited onto a wide range of substrates in the form of thin films (Eda et al. 2008). Spin coating, drop-casting, spray coating, and chemical vapor deposition methods to create continuous GO films on different substrates have been studied. Chang et al. (2010) demonstrated the development of continuous few-layer GO films deposited by spin coating GO onto substrates, including quartz, glass, and a silicon wafer (Chang et al. 2010). Zhao et al. (2014) studied the formation of continuous reduced graphene oxide (rGO) film on modified polyethylene terephthalate (PET) substrates and found that polydopamine-modified PET substrates exhibited the most favorable interaction with rGO sheets (Zhao et al. 2014). Chemical vapor deposition has emerged as an important method for the preparation and production of graphene films for various applications, such as flexible transparent conductors and field-effect transistors (Zhang et al. 2013a). Recently, Pham et al. (2010) used a spray coating method to form GO films on a small-area (2×2 cm^2) preheated quartz substrate (Pham et al. 2010). By coupling electrochemical methods with a spray coating technique, controllable synthesis of GO films on substrates up to 5×4 cm^2 has been realized (Zhou et al. 2009). In contrast to these efforts, the existing solution-based deposition methods allow coating only over small areas; this limits the usefulness of these methods for large-scale, low-cost manufacturing of GO films.

Measurement and control of moisture is a critical issue in some industrial and agriculture applications (Li et al. 2008), so the moisture level in such applications must be accurately monitored and controlled to maintain a constant level of moisture. Existing moisture sensors present issues such as slow response, slow recovery time, and low sensitivity (Bi et al. 2013). Graphene oxide is more than 10 times as sensitive as conventional capacitive moisture sensors in the range of 15% to 95% relative humidity (Bi et al. 2013). The richer oxygen groups make GO hydrophilic, enhancing the GO-based sensors' sensitivity to water (Stankovich et al. 2006). Yao et al. (2011) reported that a thin GO film coating on quartz crystal microbalance (QCM) showed excellent humidity sensing and linear frequency response versus RH in the range of 6.4% to 93.5% RH (Yao et al. 2011). Yao et al. (2012a) presented a stress-type humidity sensor based on a graphene oxide–silicon bi-layer flexible structure, with graphene oxide thin films spin-coated onto a silicon micro bridge as a humidity-sensing layer (Yao et al. 2012b). Yao and Ma (2014) reported that a Poly(dimethyldiallyammonium chloride) (PDDA)/GO composite thin film–coated QCM humidity sensor exhibited a large humidity sensing response, fast response and recovery times, and excellent repeatability (Yao and Ma 2014).

Development of Moisture Sensor

Development of SSC Method

The GO dispersion was prepared by mixing 0.5 mg GO sheets in 1 ml distilled water. The GO dispersion was sonicated for 2 hours to exfoliate GO flakes for a coating material (Yao et al. 2012a). An 8 in. silicon wafer with 50 nm thick thermal oxide was used as a substrate. The setup for the proposed SSC method is shown in Figure 29.

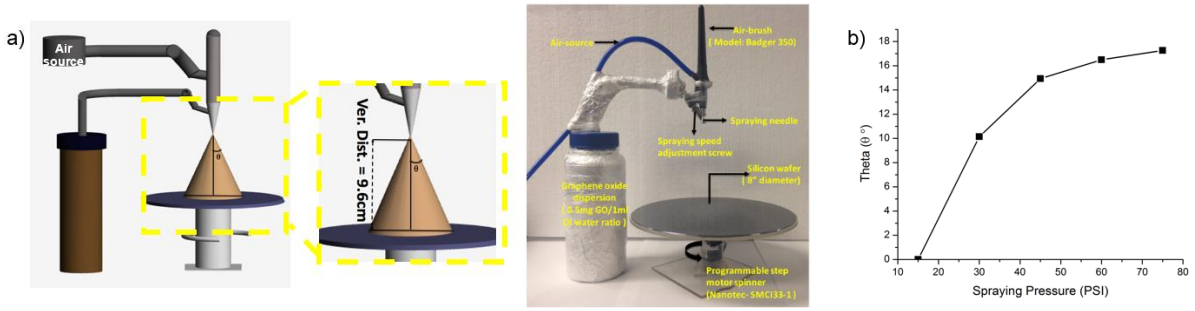

Figure 29. Proposed SSC method setup: (a) illustration and photograph showing the vertical distance between the airbrush and the substrate and θ (the half-angle of the cone-shaped stream of GO sprayed from the airbrush); (b) the effect of airbrush spraying pressure on angle θ

To set up the SSC method, a substrate is placed on top of a programmable step motor spinner (Nanotec SMCI33-1) using double-sided adhesive tape. A Badger 350 airbrush is vertically placed some distance above the center of the substrate, as shown in Figure 29 (a). Generally, the airbrush works by passing a stream of fast moving (compressed) air through a Venturi nozzle to create a local reduction in air pressure (suction) and draw a suspension from a connected reservoir at a normal atmospheric pressure. Compared to any tilted-angle positions of the airbrush, the vertical position provides a better focus of pressure on the center of the silicon wafer for the spraying process, allowing the sprayed dispersion to be suffused in all directions over the whole surface of the substrate. The key processing parameters of this process include the vertical distance between the airbrush and the substrate, the air source pressure, the substrate spinning speed, and the evaporation temperature.

The air source pressure was varied between 15 and 75 pounds per square inch (psi) to determine its effect on the spread angle θ (the half-angle of the cone-shaped GO dispersion sprayed from the nozzle), as shown in Figure 29(a). The result shows that increasing the spraying pressure up to 45 psi increases θ, as shown in Figure 29(b). Higher pressures don't change θ by much but can cause the GO dispersion to spill over from the substrate. Therefore, a 45 psi spraying pressure was selected. The spraying speed can be adjusted by turning a screw on the airbrush, as shown in Figure 29(a). When the screw is turned counterclockwise, the spraying speed increases. In the tests described below, the spraying rate was set to 9 ml/minute.

The influence of the rotational speed of the substrate on the uniformity of the GO films produced was studied. GO films obtained at different spinning speeds are shown in Figure 30 and demonstrate that the rotational speed has a significant impact on the formation of large-area GO thin films on substrates.

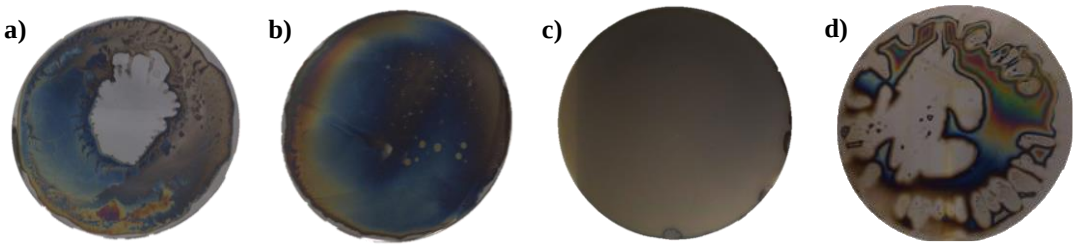

Figure 30. SSC formation of GO film on an 8 in. wafer at different spinning speeds: (a) 0 rpm, (b) 5 rpm, (c) 10 rpm, (d) 80 rpm

The optimum speed for uniform and thin GO film on large-scale substrate was found to be 10 rpm. At spinning speeds lower than 5 rpm, the spinning provides insufficient outward force to push GO dispersion over the entire surface. Conversely, higher spinning speeds cause GO dispersion to spill over, forming discontinuous GO films.

After the GO suspension was coated on the substrate using the SSC method, the coated substrate was dried, and the drying temperature's effect on the final formation of the GO film was studied. Figure 31 shows the GO films formed at different hotplate temperatures.

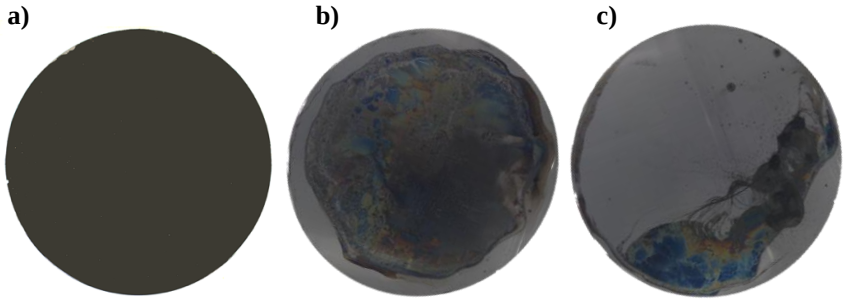

Figure 31. GO film formation at different temperatures for different evaporation temperatures: (a) 25°C, (b) 90°C, (c) 180°C

The results show that fast evaporation at high temperatures does not support the formation of continuous films.

The thickness distribution of the GO films was analyzed using a film thickness measurement system (Model F20, Filmetrics). Figure 32(a) shows the thickness measurement results for the GO films created using the SSC method on SiO_2 substrate.

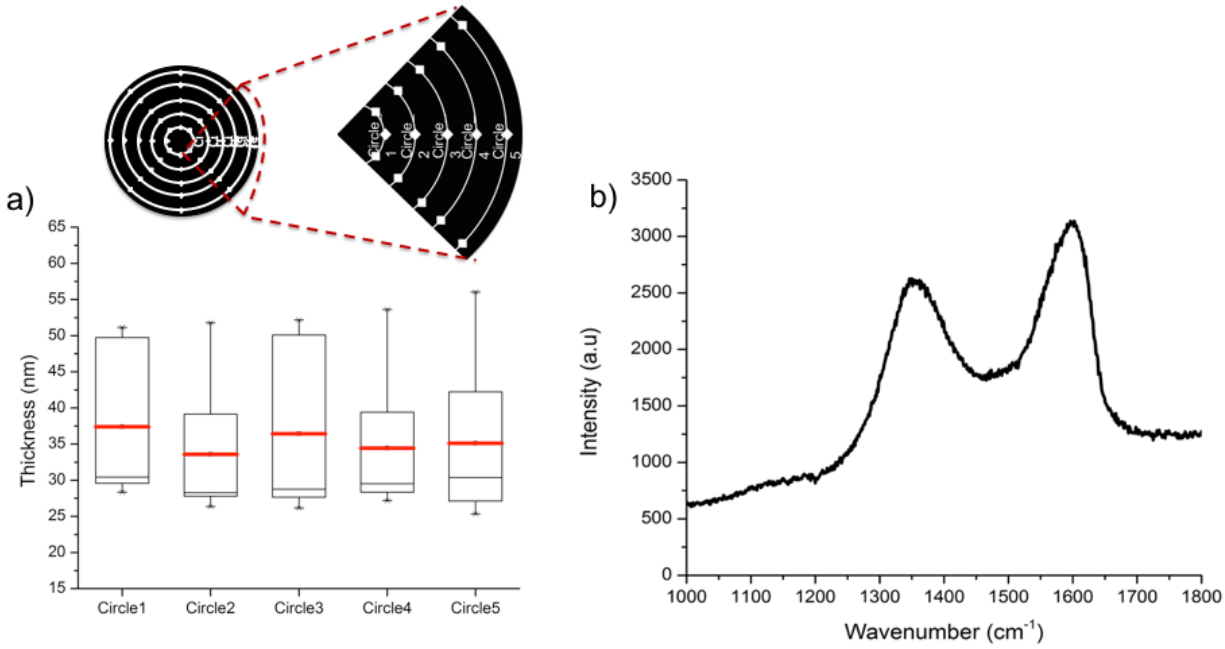

The spraying speed was at 9 ml/min (0.5 mg to 1 ml distilled water ratio dispersion).

Figure 32. Results of GO film thickness tests: (a) thickness of a GO film formed on an 8 in. silicon wafer, (b) Raman spectrum analysis of GO film produced by the SSC method

The numbered rings in Figure 32(a) represent the circular positions on the substrate from the innermost to the outermost. The thickness measurement results show that GO film was formed uniformly and continuously by the SSC method. Figure 32(b) shows the Raman spectrum of the GO film formed by the SSC method.

Figure 33 shows the scanning electron microscopic (SEM) images of the different coated films.

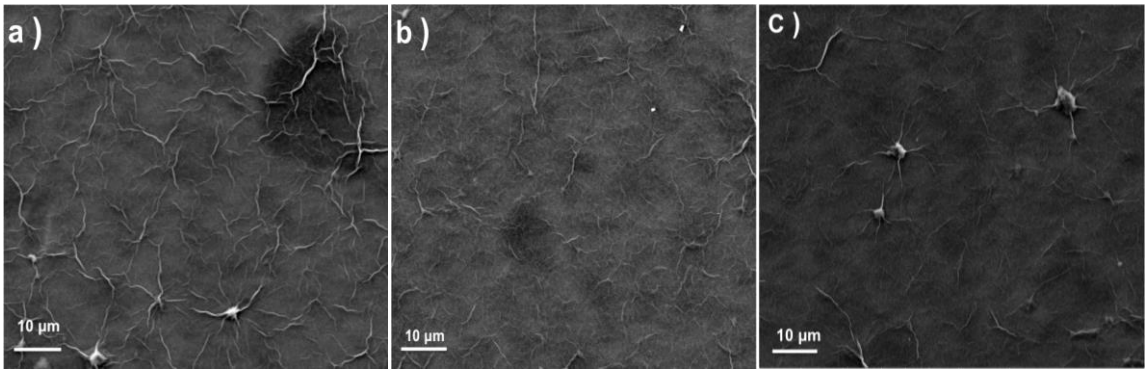

Figure 33. Scanning electron microscopy images of GO film at different regions of the coated substrate: (a) edge region of the Si wafer, (b) medium region of the Si wafer, (c) center region of the Si wafer

These continuous GO films have similar surface morphologies at different locations on the substrates. The SSC method makes the spraying method effective in obtaining uniform GO films on large-scale substrates.

Application of Spinning-Assisted Spray-Coated GO Film for Moisture Sensing

To demonstrate the application of GO films created using the SSC method and to verify how film uniformity influences the performance uniformity of GO-based devices, GO-based relative humidity sensors were developed by coating the surface of interdigital microelectrodes with GO film.

To demonstrate the application of sensors developed using patterned GO film on IDEs, dielectric humidity sensors were developed on an 8 in. wafer using the SSC method to form GO film into humidity-sensitive material. Humidity sensing was performed based on impedance analysis between 50 Hz and 100 kHz. Gold (Au) IDEs were patterned on an 8 in. Si substrate using photolithography and metal deposition techniques. First, an SiO_2 wafer was coated with Au using an Au evaporation technique at a thickness of 75 nm. At the beginning of the microfabrication of the interdigitated electrodes, an Au-coated SiO_2 wafer was cleaned using acetone, ethanol, and distilled water, respectively, and baked for 30 minutes at 90°C to remove unwanted moisture and improve the adhesive force between the gold and the Si substrate. The surface was treated with HDMS to achieve strong adhesion between the gold and the AZ photoresist (AZ 5214E); the surface was then coated with AZ photoresist by spin coating. After soft-baking the AZ photoresist–coated SiO_2 wafer for 3 minutes at 90°C, the wafer was exposed to UV light for 15 seconds at an intensity value of 8 mW/cm^2 to transfer the IDE mask pattern onto the surface of the SiO_2 wafer. Finally, unexposed areas were etched using gold etchant and rinsed with DI water to fabricate the IDEs.

To obtain patterned GO film on the IDEs, a lift-off process was performed after fabrication of the electrodes. An SiO_2 wafer patterned with Au IDEs was coated with AZ photoresist using the same process. The wafer was then exposed to UV light for 5 seconds at an intensity of 4 mW/cm^2 to transfer the pattern onto the SiO_2 wafer. To make the exposed areas insoluble in the developer, the UV-exposed substrate was post-baked for 60 seconds at 110°C**.** Then, to make the unexposed areas developable, a floodlight exposure was applied for 114 seconds at an intensity of 10mW/cm^2. The unit was finally developed with AZ 726 metal-ion-free (MIF) developer until the pattern could be clearly seen. After this step, the SiO_2 substrate was treated with O_2 plasma to make the surface hydrophilic, and GO coating was applied by the SSC method. Finally, after the GO film was formed the photoresist was removed with acetone, producing GO-coated IDEs, as shown in Figure 34(b). The whole process flow of forming patterned GO film on IDEs can be seen in Figure 34(a).

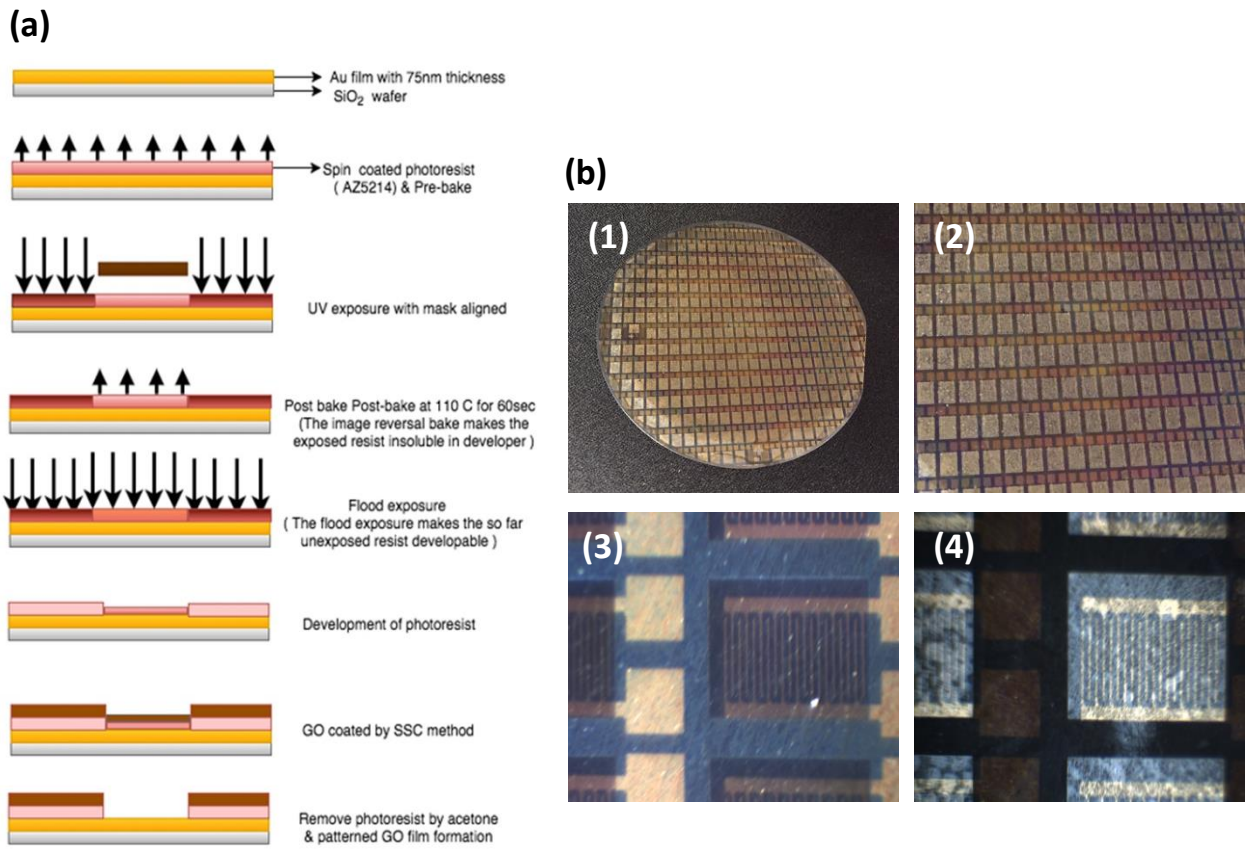

Figure 34. Fabrication steps and optical images of sensors: (a) process flow of patterned GO film fabrication on Au interdigitated electrodes; (b) GO film–patterned Au interdigitated electrodes on Si wafer, (1) fabricated device with the process defined in (a), (2) GO film–patterned IDEs on SiO_2 wafer, (3) microscope image of IDEs developed with negative photoresist, (4) microscope image of IDEs coated with GO film

To demonstrate the application of sensors developed using patterned GO film on IDEs, humidity sensors were developed on an 8 in. wafer using the SSC method to form GO film as a humidity-sensitive material. Humidity sensing was performed between 50 Hz and 100 kHz based on impedance analysis.

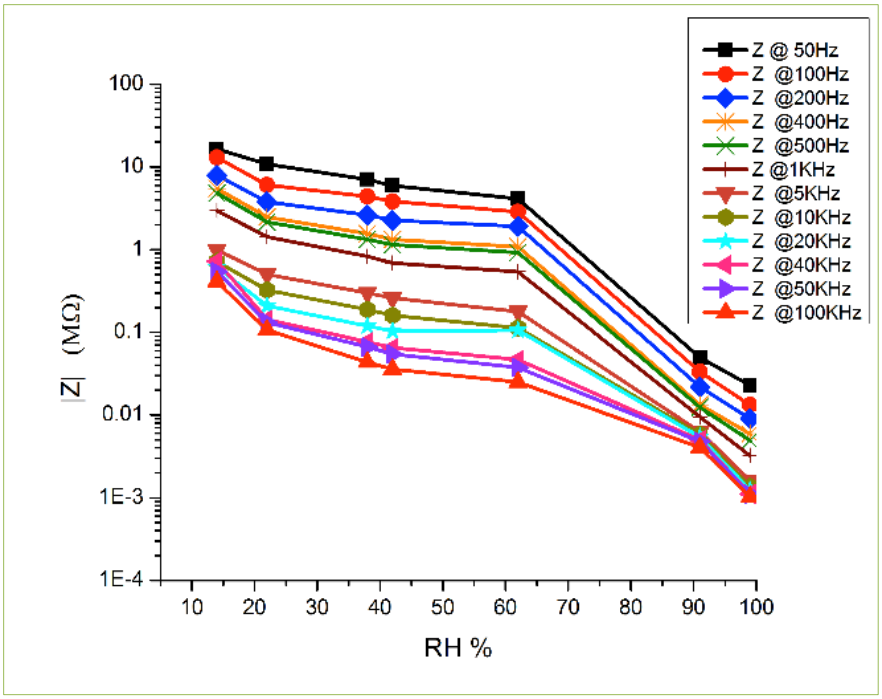

Figure 35. Impedance analysis of GO-based humidity sensors at different RH values for a frequency range of 50 Hz to 100 kHz

Essentially, the resistivity of GO is related to physisorption (physical adsorption) of water molecules on GO because different sorption processes yield different resistivity values inversely proportional to humidity. At lower humidity levels, GO has very strong double hydrogen bonding, so water molecules cannot penetrate into the GO. GO is a hydrophilic material so it tries to adsorb the water, but because of the double hydrogen bonding it exhibits a strong electrical resistivity. When the humidity increases, the penetration and adsorption of water molecules becomes easier, so resistivity decreases. As shown in Figure 36, the impedance of GO films decreases as humidity increases.

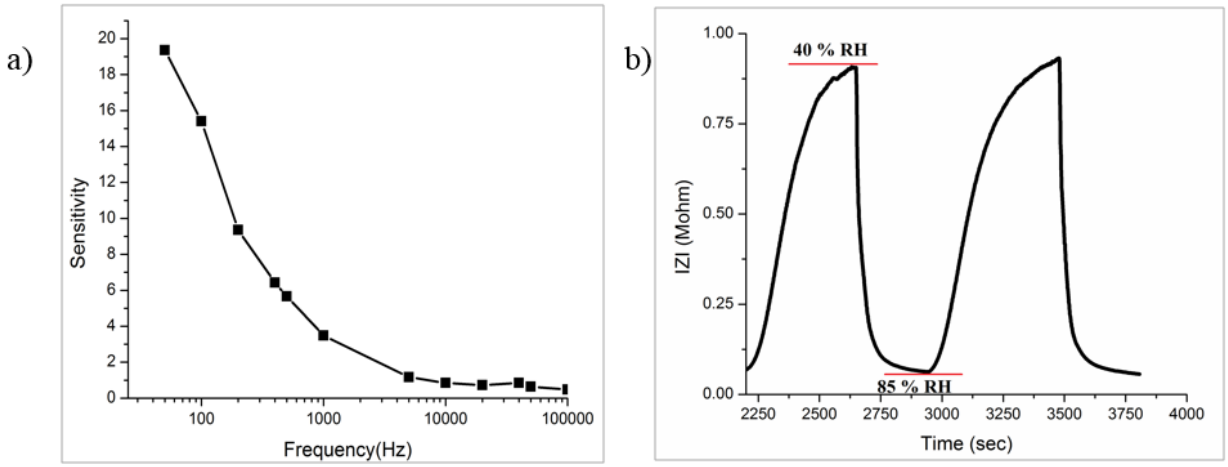

Figure 36. Impedance of GO film: (a) sensitivity analysis based on the impedance change in GO film between 14% RH and 99% RH with frequency range from 50Hz to 100 kHz, with sensitivity defined as the change in impedance for a 1% change in RH; (b) transient response of the sensor between 40% RH and 85% RH at 50 Hz

Sensitivity is defined as the impedance change for a 1% RH change in a frequency range of 50 Hz to 100 KHz. As seen in Figure 36(a), sensitivity is inversely proportional to frequency.

As frequency increases, the direction of the electric field changes so fast that the adsorbed water molecules on a GO film cannot catch up, causing the sensor to be less sensitive. As with all sensors, exhibiting a fast response is a critical issue for humidity sensors because the sensor should provide output in a very short time after an instantaneous change in humidity. A transient response measurement (as relative humidity was increased from 40% to 85%) indicated that the response time of the sensor is about 40 seconds, as shown in Figure 36(b), and the GO layer thickness has a significant effect on this response time. In principle, the oxygen groups make GO hydrophilic, so water molecules can easily intercalate into the inner side of the GO when the film is relatively thin (Stankovich et al. 2007).

Key Findings and Results

The fabrication of thin and uniform GO film on a large-scale substrate using the SSC method to apply GO film as a sensing material was demonstrated. The key parameters of the process were considered, including the vertical distance between the airbrush and the substrate, the pressure of the air source, the spraying speed, and the substrate spinning speed. The optimization of these parameters supports spraying a GO dispersion onto the wafer's center while spreading it towards the wafer's edges without any spilling over. To demonstrate sensor applications for large-area GO films, GO-based humidity sensors were developed on an 8 in. SiO_2 wafer. Impedance-based analysis showed that the GO-based sensor exhibited high sensitivity to humidity with a fast transient response time and good repeatability. These results demonstrate a cost-effective method for forming large-area GO film for sensing applications.

MEMS-BASED STRAIN SENSORS

Flexible Graphene Strain Sensor with Liquid Metal

Summary of the Work

A graphene-based strain sensor was developed using an all-flexible material, thin graphene film as a sensing element, liquid metal for signal conducting, and polydimethylsiloxane (PDMS) for packaging. In this design, the liquid metal interconnections improved the flexibility near the sensing area to retain the sensor's maximum sensitivity; the all-flexible structure also combines good repeatability with long survival life.

First, the liquid metal interconnections maximize the sensitivity of the sensor. Even though multiple graphene strain sensors made of flexible materials exist, their electrical interconnections generally use hard metal/alloy materials. Such solid material near a sensing area introduces an influence during specimen deformation that affects the strain measurement. In the proposed design, the liquid metal interconnections between the sensing element and the solid wires, which retain a high flexibility around the detecting area, allows the sensor itself to achieve the maximum sensitivity. Measurement of the resistance response showed that the liquid metal used for the interconnections does not affect the overall resistance signal resulting from the strain placed on the graphene while still achieving full sensor flexibility.

Second, this graphene-based strain sensor, with its fully flexible structure, yields a trustworthy strain measurement device that exhibits good repeatability and a long life. The sensor was stretched and released under different levels of strain over a long time period, and the sensor's resistance reaction continued to produce the expected values. In a demonstration of multidirectional strain measurement using stacked sensors in a rosette structure, the sensor system successfully provided both direction and magnitude information for the incoming force. In a structural health monitoring application, the sensor was glued onto a curved concrete surface, and the sensor signal responses exhibited the same pattern as the applied load on the concrete.

The development of the flexible graphene strain sensor involved the following steps:

- Develop wireless small-strain MEMS sensors capable of continuously detecting strain changes inside concrete
- Develop a packaging method for small-strain MEMS sensors embedded inside concrete
- Test the long-term stability of the packaging method
- Successfully demonstrate the capability of small-strain MEMS sensors in the laboratory to monitor time-varying strain information inside and on the surface of concrete structures

Literature Review

Strain sensors have been widely used to monitor mechanical and structural damage, evaluate material fatigue properties, and track human body movement. Recently, graphene has been investigated as an important pressure and strain sensing material because of its high piezoresistivity, fast electron mobility, and high Young's modulus (Jing et al. 2013, Lee et al. 2008, Hempel et al. 2012). Significant efforts have been made to fabricate various graphene-based strain and pressure sensors by suspending a graphene membrane over a shallow well on a silicon substrate, transferring a graphene membrane onto a micromachined silicon nitride membrane, and using graphene flakes to cover an array of wells engraved into a silicon substrate (Bae et al. 2013, Fu et al. 2011, Wang et al. 2011, Frank et al. 2011, Hempel et al. 2012).

These MEMS-based pressure sensors have a compact footprint but limited structural flexibility. In a different category, graphene-based strain and pressure sensors have been developed with large-area graphene-polymer composite, laser-scribed graphene foam, and patterned graphene on elastomer (Jing et al. 2013). These sensors often have a large size, on the order of square centimeters or even larger, but are made with structurally flexible materials that have great potential for many wearable sensor applications (Yamada et al. 2011). It is worth pointing out that in existing graphene-based sensors, the electrical interconnections are generally achieved using hard metal/alloy materials (Engel et al. 2006). This can not only compromise the overall structural flexibility of the devices, but may also cause a long-term reliability issue due to possible local strains introduced into the interconnecting areas during sensing and actuation.

In contrast, many liquid metals have been found to be non-toxic and non-evaporative and can melt at room temperature. They have comparable electrical conductivities and better wetting properties than mercury (Morley et al. 2008). Due to the fluid nature of liquid metals, they can flow and reshape without cracking or fatigue when responding to mechanical deformation. Recently, the inclusion of liquid metal into a flexible elastomer has led to several tunable and wearable electronic devices, including electrical probes (Chiechi et al. 2008), microfluidic electrodes (So and Dickey 2011), electrical interconnectors (Kim et al. 2008), antennas (Jobs et al. 2013), and metamaterials (Yang et al. 2016). Among existing liquid metals, gallium-indium eutectic (EGaIn) is considered to be one of the most promising metallization candidates for flexible electronics because of its liquid state at room temperature and its low toxicity (Morley et al. 2008). It has been reported that such liquid metal can be introduced via the openings of a silicon interposer to better accommodate thermal stresses and provide re-workability in the case of chip failures or upgrades (Hu et al. 2007). In addition, this liquid metal has enabled the flexible packaging of solid-state integrated circuits into a flexible substrate (Hernandez et al. 2013, Zhang et al. 2013a).

Based on this literature review, fully flexible graphene strain sensors using liquid metal as interconnectors for enhanced structural flexibility and reliability were proposed. Such sensors can be formed by encasing graphene sensing elements in an elastomer containing built-in microfluidic channels filled with liquid metal. Such flexible technology allows for the hybrid integration of graphene-based sensing material with liquid metal–based microfluidics to achieve full structural flexibility of the strain sensor. To explore potential applications for such sensors,

multiple flexible strain sensors were bonded together layer by layer in a rosette structure to form a flexible rosette strain sensor with the capability to measure strains coming from multiple directions. The feasibility of monitoring strain in concrete was also demonstrated.

Strain Sensor Development

Development of the Stamping Technique

A technique was developed to pattern graphene on a PDMS layer, as shown in Figure 37.

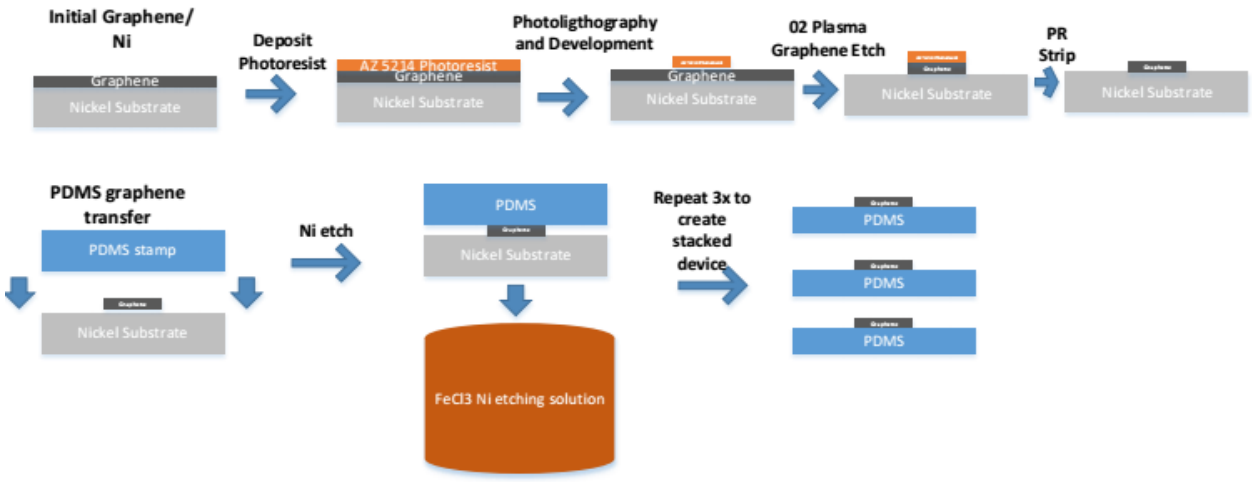

Figure 37. Process flow of PDMS stamping

This technique lays the foundation for developing various high-performance strain sensors for structural health monitoring. Figure 38 shows the sensor before transfer.

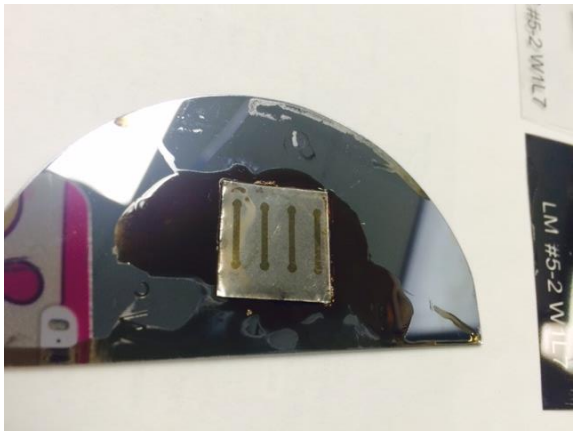

Figure 38. Graphene sensor fabrication: patterning photoresist to create a protection layer for etching

The major steps in the fabrication technique are as follows:

- Prepare the graphene on a nickel (Ni) sample (Graphene Supermarket, chemical vapor deposition [CVD] multilayer graphene film on Ni foil, 2 in. by 2 in.). Ensure that the photomask can fit onto the sample.
- Use AZ photoresist to glue the graphene film onto the surface of a silicon half-wafer, and flatten the sample by hand.
- Bake to dry the glue at 90°C (at least 70°C) for 5 to 10 minutes (depending on the size of the sample).
- Spin-coat the AZ photoresist for 25 seconds at a speed of 500 rpm.
- Pre-bake the sample for 5 minutes at 90°C and allow it to cool for 5 minutes.
- Spray acetone on the photomask for cleaning, then heat the mask for drying at 70°C.
- Expose the mask to UV light at an intensity of 2 mW/cm^2 for 90 seconds, and use a glass slide to flatten the mask.
- Prepare ferric chloride hexahydrate ($FeCl_3$) with a weight of 27 grams dissolved in 300 ml water (in a plastic silver bottle with a blue lid) to etch the nickel.
- Use aluminum foil to cover the etching solution, and use a slow shake for quicker dissolving.
- Immerse the sample for 90 seconds in AZ photoresist developer (about 120 mL). Wash the sample with regular water; for more complete washing, the sample can be immersed into water.
- Blow dry the sample, and post-bake for 10 minutes at 120°C.

After the process described above, follow with nickel etching, IBA patterning, PDMS bonding with alignment, liquid metal injection, and sealing with PDMS. The detailed fabrication process is described in the following steps:

- Use oxygen plasma for graphene etching.
- Prepare a PDMS stamp.
- Remove the photoresist, soak the sample in acetone, remove the graphene from the Si wafer, wipe the Si wafer for reuse, wipe the photoresist from the sample, and wipe away any graphene residue.
- Rinse the sample in water for a couple of minutes, then blow dry and bake for further drying.
- Remove the PDMS stamp and cut it into a shape equivalent to that of the sample; the side touching the glass will be the side that touches the graphene.
- Place the PDMS layer with the graphene sample facing upward.
- Remove the PDMS, making sure that the sample stays on the PDMS.
- Place the sample in a $FeCl_3$ solution, with the graphene facing downward and the PDMS floating on the solution.
- Wait 24 to 36 hours, then etch out the nickel.
- Rinse with water.

To elucidate the graphene sheet transfer process, a Raman shift provides information about the graphene film during the PDMS stamping process to confirm that the strain-sensitive graphene

thin film has been successfully transferred from a hard to a flexible substrate. A comparison of the peaks of the Raman shift in Figure 39 provides evidence of successful graphene transfer.

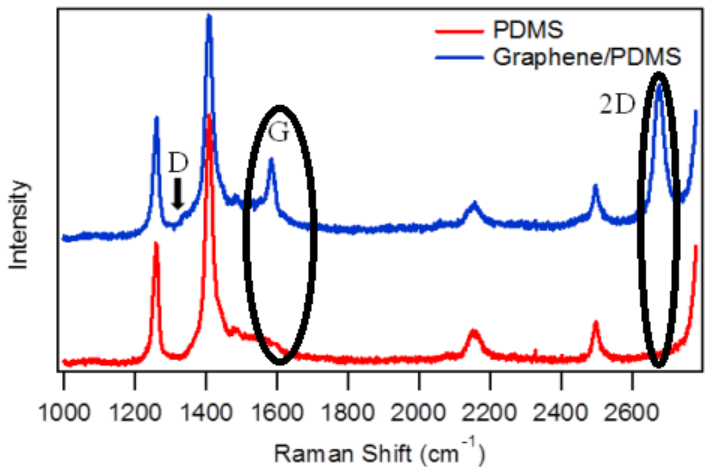

Figure 39. Raman shift of graphene before and after transferring

Development of the Multiple Layer Alignment Technique

To develop a strain sensor that can detect strain in multiple directions, a design for a multidirectional small strain sensor was proposed, as shown in Figure 40.

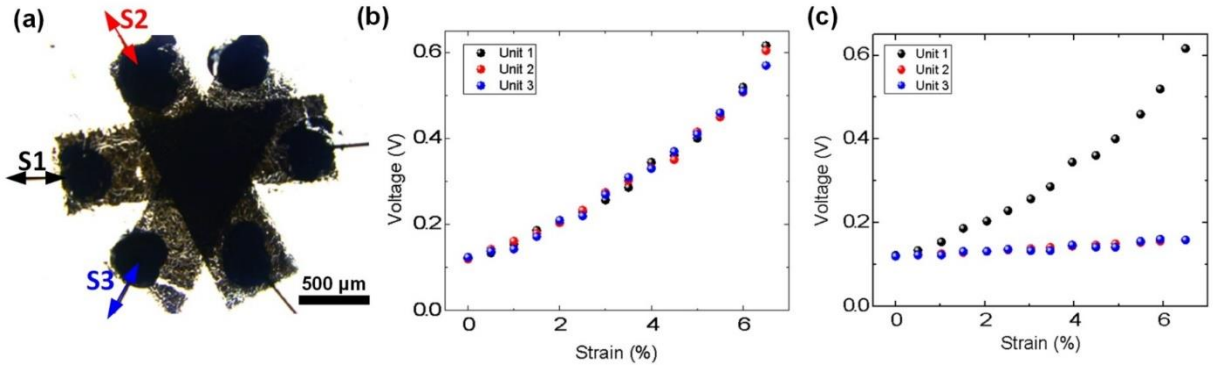

Figure 40. First generation of rosette graphene strain sensor

Micromachining technology was developed to chemically bond and align multiple layers of single-directional strain sensors. This design enabled accurate multi-directional strain detection in small areas.

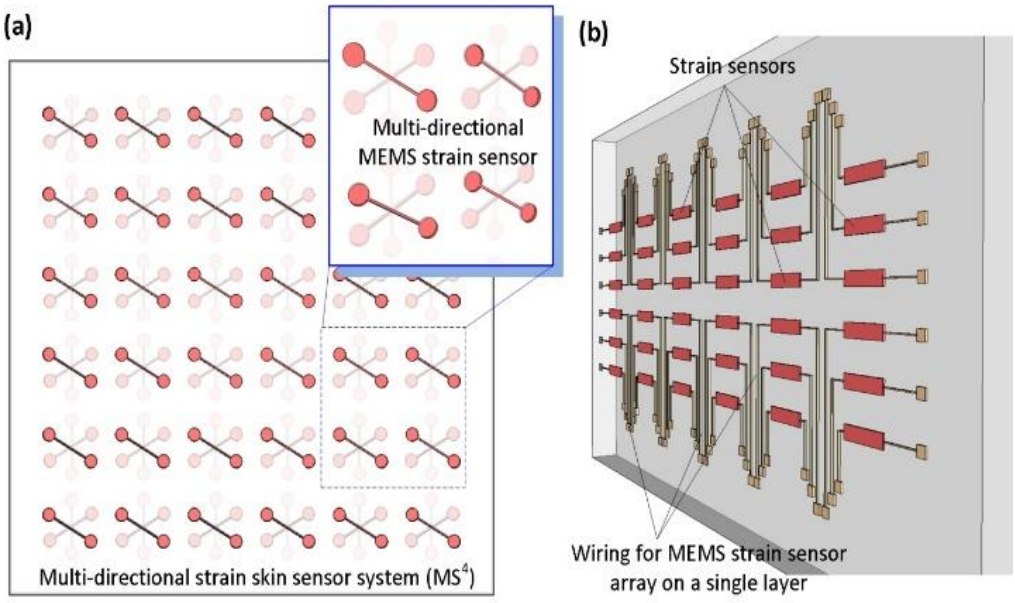

Figure 41. Multi-directional strain sensor system

For larger scale applications, embedding a MEMS strain sensor array on a single-layer device would create the capability for strain distribution to be determined and analyzed over a large area.

Development of the Signal Conduction Technique

To study conduction from the graphene to the exterior circuitry, patterned graphene sensors were packaged in PDMS protection layers with both contact and contactless interfaces. Different patterns were fabricated and tested using either gold or liquid metal as conductors to achieve fully bendable structures, as shown in Figure 42 through Figure 44.

Figure 42. Gold used as conduction wire

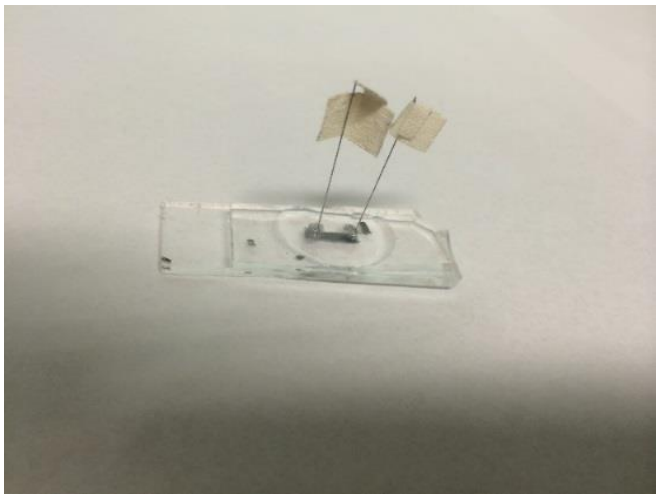

Figure 43. Direct contact with conductor wire

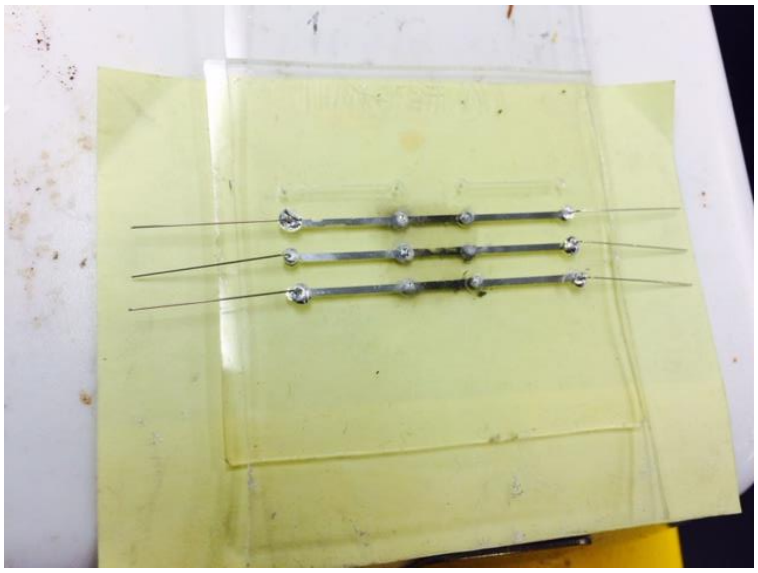

Figure 44. Liquid metal used as a conductor

Development of the Sensor Fabrication Technique

Before the major layer of the sensor was fabricated, an IBA model for PDMS channel fabrication was created, as shown in Figure 45.

Figure 45. IBA for PDMS channel fabrication

This design contains a 150-micron-thick liquid metal channel with a 1 mm wide graphene strip array and was fabricated using 24 seconds of UV exposure at an intensity of 8 mW/cm^2.

The strain sensors were fabricated based on an "all-flexible" concept, which combines the benefits of using graphene as the core detecting component and liquid metal as the contact material. The concept of the sensor and the design for the photomask are shown in Figure 46.

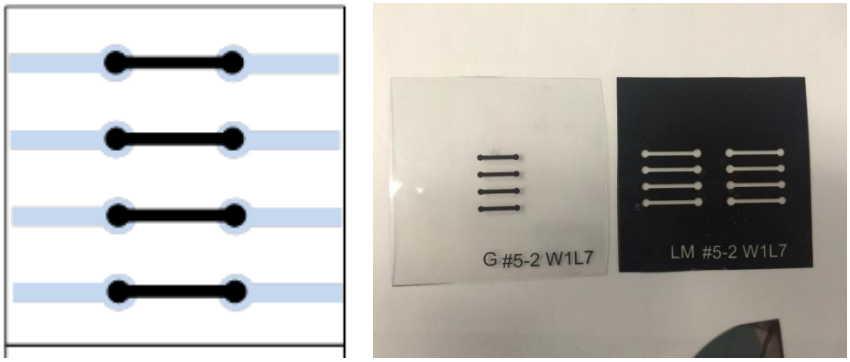

Figure 46. Concept sketch of all-flexible strain sensor (left) and photomask design of sensor array (right)

The following fabrication steps were used to produce sensors with a four-pair array design, which was intended to improve yield and calibration:

1. The steps in the sensor fabrication process were as follows:
    - Prepare the graphene on a nickel sample (Graphene Supermarket, CVD multilayer graphene film on Ni foil, 2 in. by 2 in.). Ensure that the photomask can fit onto the sample.

- Use AZ photoresist to glue the graphene film onto the surface of a silicon half-wafer, and flatten the sample by hand.
- Bake to dry the glue at 90°C (at least 70ºC) for 5 to 10 minutes (depending on the size of the sample).
- Spin-coat the AZ photoresist for 25 seconds at a speed of 500 rpm.
- Pre-baking the sample for 5 minutes at 90ºC and let it cool for 5 minutes.
- Spray acetone on the photomask for cleaning, then heat the mask to dry at 70ºC.
- Expose the mask to UV light at an intensity of 2 mW/cm^2 for 90 seconds, and use a glass slide to flatten the mask.
- Prepare 27 grams of ferric chloride hexahydrate ($FeCl_3$) dissolved in 300ml water to etch out the nickel.
- Use aluminum foil to cover the etching solution, then slowly shake for quicker dissolving.
- Immerse the sample for 90 seconds in about 120 mL of AZ photoresist developer. Wash with regular water; for more complete washing, the sample can be immersed into water.
- Blow dry the sample, and post-bake for 10 minutes in 120ºC.
- Use oxygen plasma for graphene etching for at least 30 minutes.
- Remove the photoresist, soak the sample in acetone, remove the graphene from the Si wafer, wipe the Si wafer for reuse, wipe the photoresist from the sample side, and wipe away any graphene residue.
- Rinse in water for a couple of minutes, then blow dry and bake for further drying.
- Remove the PDMS stamp and cut it into a shape equivalent to that of the sample; the side touching the glass will be the side that touches the graphene.
- Place the PDMS layer with the graphene sample facing upward.
- Remove the PDMS, making sure that the sample stays on the PDMS.
- Place the sample in a $FeCl_3$ solution, with graphene facing downward and the PDMS floating on the solution.
- Wait 24 hours for the nickel to etch out.
- Rinse with water.

2. The steps in the sensor packaging process were as follows:
    - Prepare 1:15 PDMS, fully mixed; degas the solution for 20 minutes; pour the solution into a patterned IBA channel; and bake the sample for 60 minutes at 85°C.
    - Cut out the PDMS and drill holes into the connection for liquid metal injection.
    - Treat the graphene in the PDMS sample with oxygen for 10 minutes; cut the PDMS cap, bond the components together, and bake the sample at 85°C for 10 minutes.
    - Inject the liquid metal using a needle slightly smaller in diameter than the drilled hole.
    - Put wires into the drilled holes to make contact with the liquid metal, then seal the package with another layer of 1:15 PDMS.

Figure 47 shows the sensor at each of the major fabrication steps.

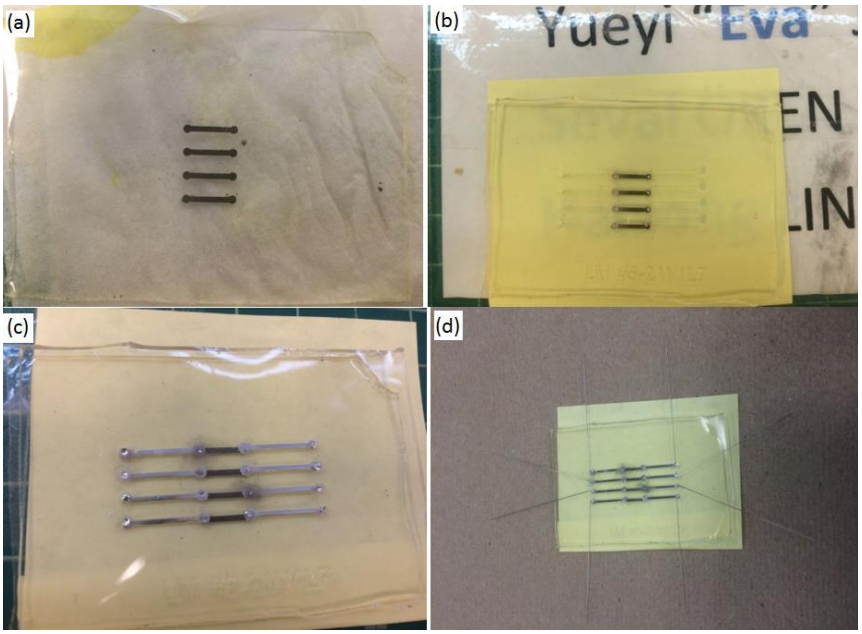

Figure 47. Sensor fabrication process: (a) patterning graphene film, (b) forming microchannels, (c) loading liquid metal, (d) sealing channels

Development of the Sensor Testing Technique

To test the behavior of the sensor in the laboratory, a manually controlled linear stage was first used to obtain a rough measurement, as shown in Figure 48.

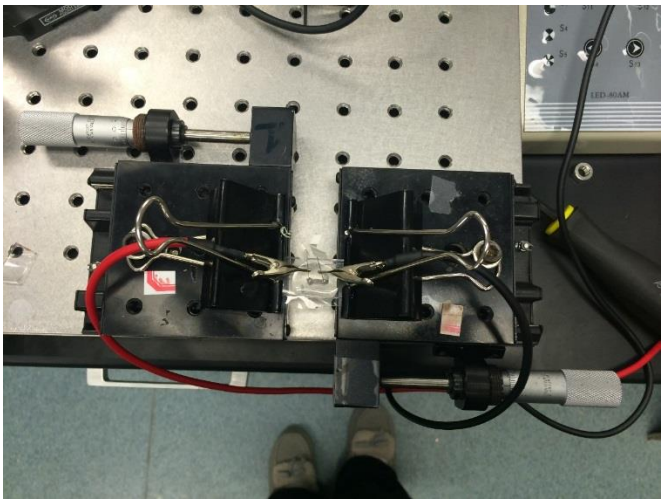

Figure 48. Manually controlled linear stage

During this step, the laboratory sensor strain testing method was improved by replacing the manual rotary length controller with a computer-controlled programmable motor linear stage, as shown in Figure 49.

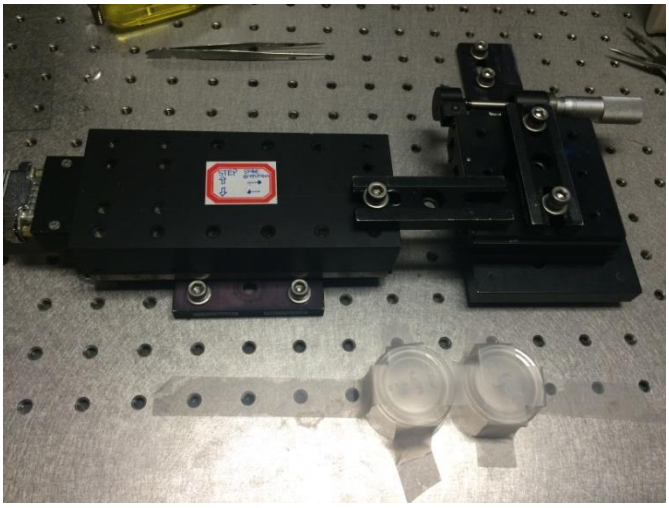

Figure 49. Motor-controlled linear stage setup for strain resistance testing in the laboratory

Using this new device for testing provided the capability to control the length change to a resolution of 1 micrometer with a constant speed, which greatly improved the data accuracy and reliability and decreased the error during testing. To convert the linear length change to the strain felt by the sensor, one edge of the sensor was fixed with screws, and another edge was stretched to a designed length using the linear stage. This new setup also provided load/unload cyclic measurement.

To offset the resistance resulting from installation, the sensor was first pre-stretched and fixed to the linear stage. When the length is changed by a certain amount, the sensor responds to the strain produced by changing the resistance that is detected and recorded by an LCR meter. Repeating this procedure produced the averaged result shown in Figure 50.

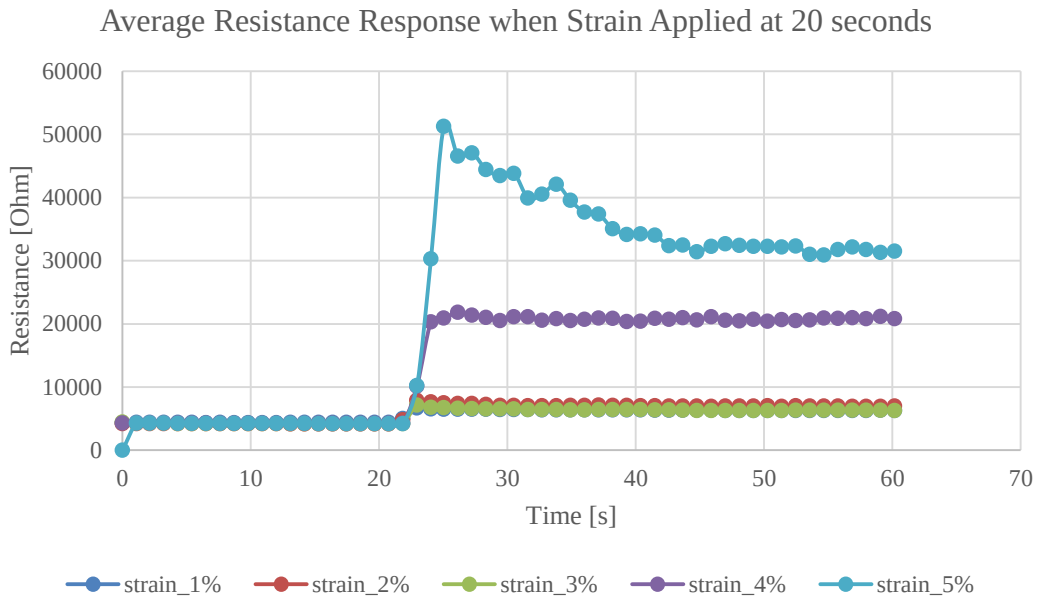

Figure 50. Averaged resistance response when strain applied at 20 seconds

Figure 50 shows an increase in resistance (y-axis) at 20 seconds (x-axis) due to the additional applied force. The resistance becomes stable at about 30 seconds, indicating that the sensor quickly responds to the strain. The magnitude of change depends on the strain applied, with a higher stain producing a higher resistance change.

The resistance of the liquid metal at different strain levels was also tested. The results of this testing led to the conclusion that graphene is effective as the core of the strain sensor because it responds to small strains very sensitively. At the same time, the liquid metal improves the sensor's signal out connection without affecting total sensor sensitivity.

To study sensor stability during the load and unload processes, cyclic measurement for the strain sensor was performed in the laboratory. Strain was applied and released, and sensor resistance was recorded with an LCR meter. When the sensor was stretched due to strain, the resistance response was at a different level than when no extra force was applied. After the additional strain was released and the sensor returned to its pre-stretched status, the resistance decreased to its original value as well. The test was done under different loading strains with the same result.

Key Findings and Results

Three major steps were involved in fabricating the graphene sensors: patterning and transferring of the graphene, formation of the microfluidic channels, and formation of the liquid metal wires. Photoresist was first spin-coated and photo-patterned on the surface of a nickel foil substrate, on which was grown a 105-nm-thick graphene layer. Subsequently, oxygen plasma was used to etch away the graphene from the unwanted area on the foil. After the photoresist was removed using acetone, the graphene patterns were formed. To transfer the patterned graphene onto the surface

of an elastomeric substrate, PDMS precursor solution (Dow Corning, Sylgard 184 Silicone Elastomer Kit, weight ratio of parts A:B = 15:1) was mixed and degassed in vacuum, poured into a petri dish, and then partially cured for 40 minutes at 85°C on a hotplate. The resulting PDMS had a thickness of 1 mm after cutting; the fresh PDMS was immediately stamped onto the surface of the patterned graphene.

The PDMS−nickel foil stack was then immersed into a 5% by weight $FeCl_3$ solution for 24 hours or until the nickel foil was fully etched, which transferred the graphene patterns to the surface of the PDMS elastomer. Next, to form liquid metal wires for making electrical contacts with the patterned graphene, microfluidic channels were formed on another thin PDMS elastomer using a master mold with microchannel patterns created by patterning 200-µm-thick photoresist (SU-8-2075, Microchem Corp.) onto a glass slide using photolithography. The same PDMS precursor solution was poured over the mold, which was then baked at 70°C for 40 minutes. After the patterned PDMS layer was peeled away from the mold, the holes necessary for loading the liquid metal were manually punched through the PDMS layer. Subsequently, this PDMS channel layer and the other PDMS layer with the graphene patterns were bonded using an oxygen plasma treatment. Then, EGaIn liquid metal was injected into these channels through a syringe with a stainless steel needle, thereby reaching and making contact with the graphene patterns. Finally, to achieve electrical connections to the external circuits, thin metal wires were inserted into the channels through the punched holes. These holes were later sealed by a drop of thermally cured PDMS precursor solution, resulting in the realization of a graphene strain sensor with full flexibility. The process for developing these sensors is shown in Figure 51.

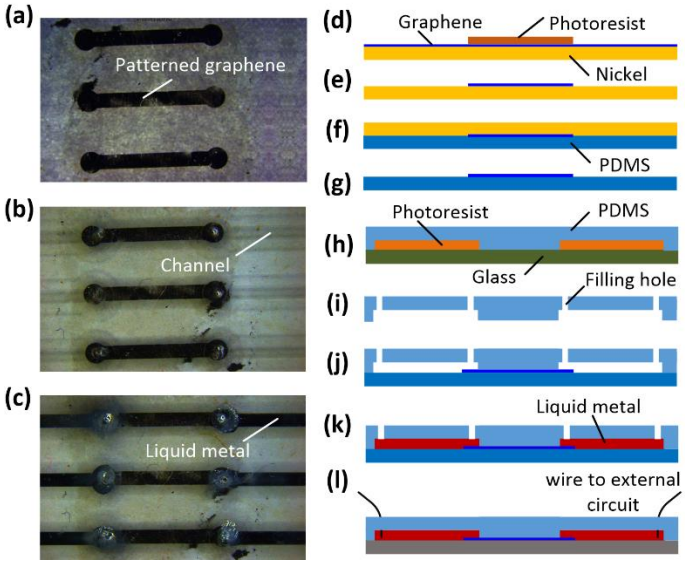

Figure 51. Process flow for making fully flexible graphene strain sensors

A multidirectional rosette-type strain sensor (Figure 52) was also developed. It was composed of three individual graphene sensing elements arranged at 60° angles from one another and embedded into four PDMS layers.

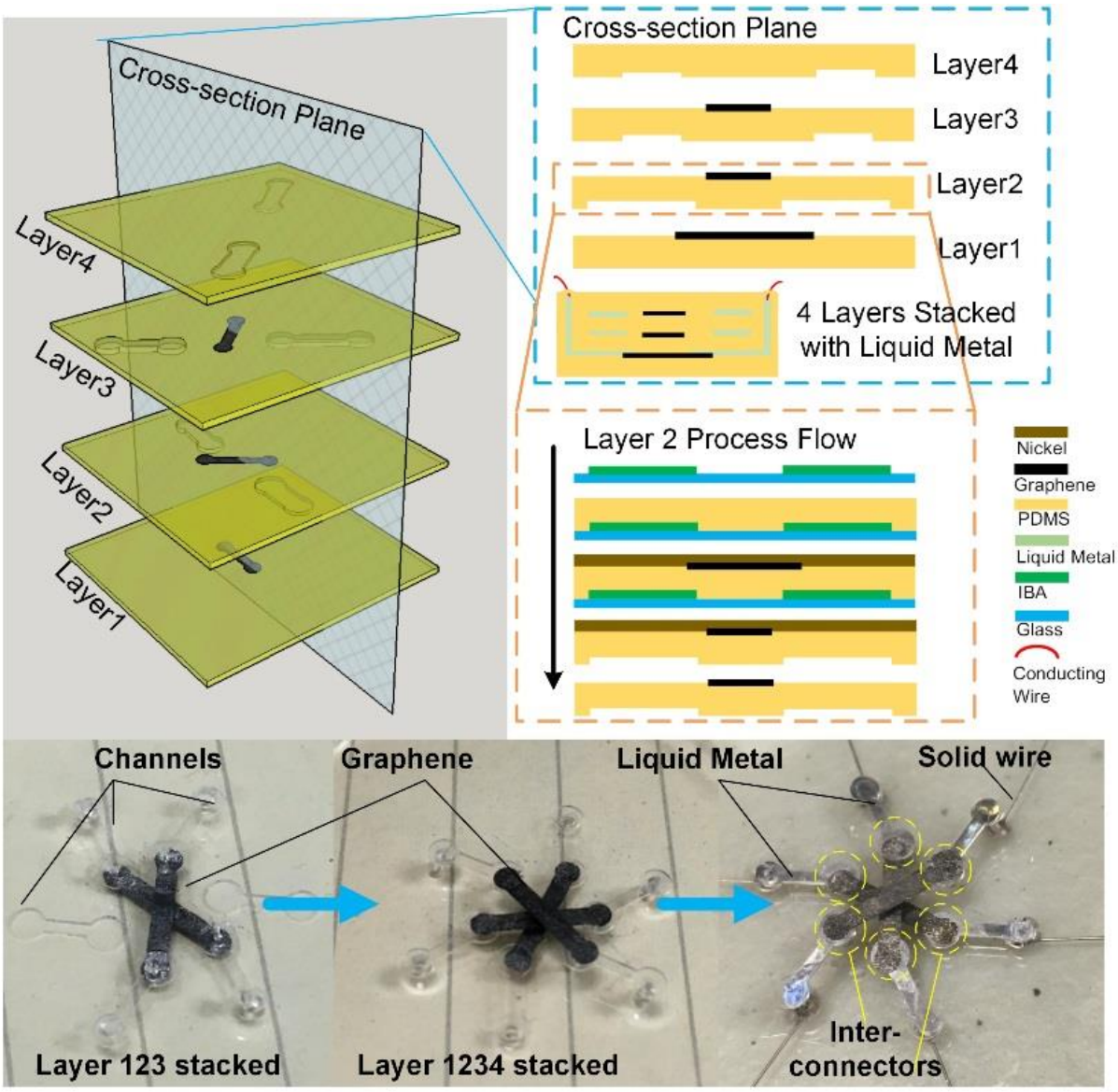

Figure 52. Process flow for making a stacked rosette strain sensor

For the multidirectional strain sensor, graphene elements S1, S2, and S3 were formed on the top surfaces of three PDMS layers L1, L2, and L3, respectively. PDMS layer L4 resided on the very top of the device but contained no sensing elements. Liquid metal channels M1, M2, and M3 for making electrical contacts with S1, S2, and S3 were formed on the backside of L2, L3, and L4, respectively. Each PDMS was 1 mm thick, and each liquid metal channel was 250 µm deep. The process for making S1 on the top surface of L1 was the same as that used to create the individual graphene sensor, as described above. To form L2 and L3 with microchannel patterns on the back and graphene patterns on the top, master molds for the microchannel patterns were first created by patterning 200-µm-thick photoresist (SU-8-2075, Microchem Corp.) on glass slides. The aforementioned PDMS precursor solution was then spin-coated on the formed molds at 500 rpm for 40 seconds and then baked at 70°C for 40 minutes. The patterned graphene structures were subsequently transferred to the top surfaces of L2 and L3 using the processes described above.

After the filling holes were formed, the four PDMS layers were bonded using an oxygen plasma treatment. Finally, liquid metal was filled into the channels, and the filling holes were sealed using the same process described above.

Figure 53(a) shows that when the fabricated graphene sensor was twisted and bent, the liquid metal at the end of the channel remained in good contact with the graphene patterns. To test the resistance changes of the sensor in response to such stretching, the sensor was fixed on a computer-controlled motor-driven linear stage, with the direction of stretching along the long dimension of the graphene strip. Figure 53(b) shows that the resistance of the sensor (3 mm wide and 10 mm long) varied between 245 and 295 ohms as the applied strain increased to 9%. When the stretch was relaxed, the sensor reset to its initial state, reflecting reversible cycling behavior. Figure 53(c) shows that the liquid metal wires of the sensor have little influence on the total resistance response of the sensor to applied strains. Here, two electric wires were fed out from the two contacts between the liquid metal and the graphene sensing element, with two other wires fed from the other ends of the liquid metal wires.

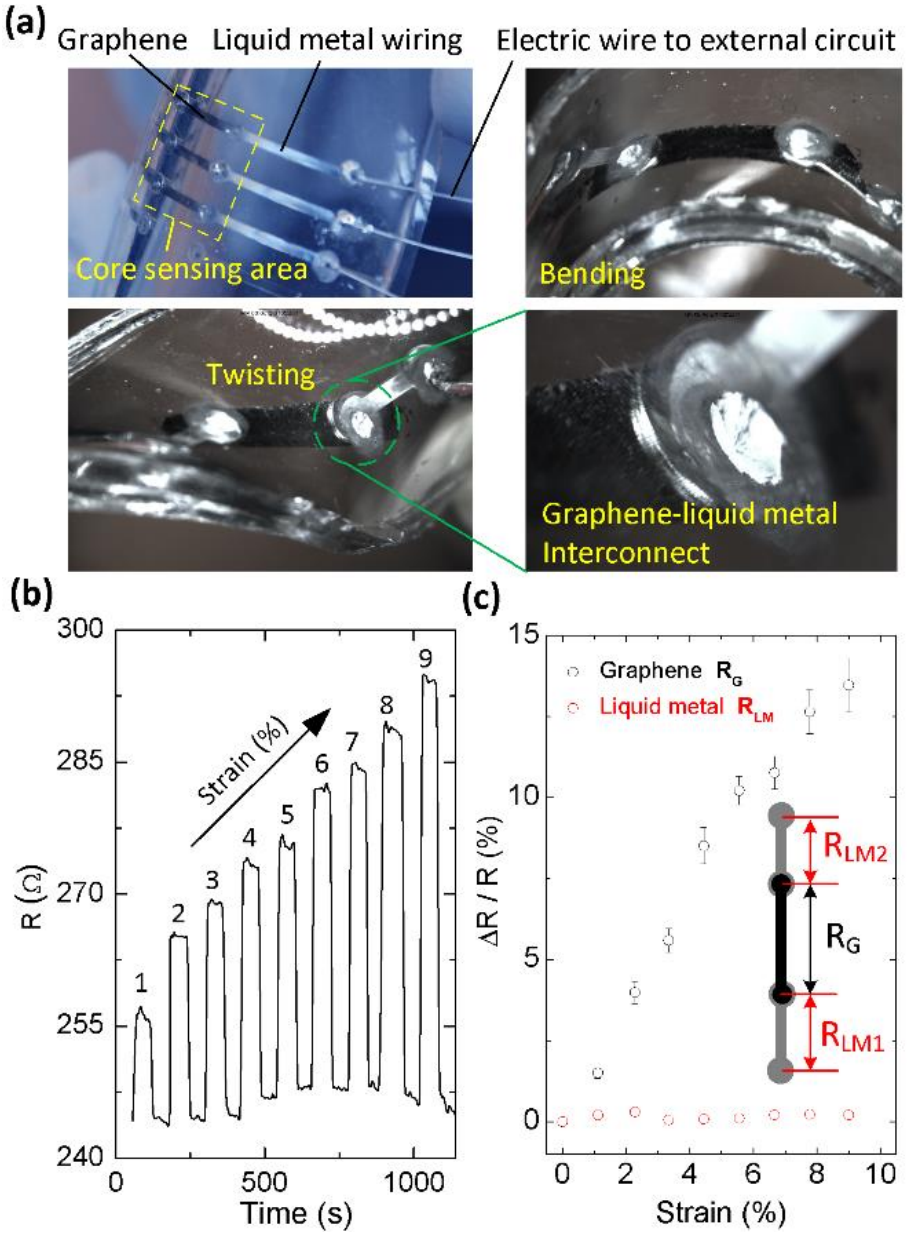

Figure 53. Completed fabricated unidirectional graphene strain sensors: (a) Photographs showing structural flexibility of the fabricated unidirectional graphene strain sensors using liquid metal for wiring inside the encasing elastomer, (b) resistance changes of the strain sensor in response to applied time-varying strains during cyclic stretch and release measurements, (c) relative resistance changes of the graphene strip alone and the liquid metal wire alone as a function of applied strain, with the inset showing the wiring schematic for this measurement

Strains were then applied along the long dimension of the sensor. This setup allowed separate measurement of the strain-induced resistance changes in the liquid metal wires and the entire sensor. The results show that the graphene's resistance changed more significantly than that of the liquid metal. A gauge factor F_G was used to evaluate the sensitivity of the liquid metal and

graphene to the applied strains, as follows: $F_G = (\Delta R / R) / (\Delta L / L) = \Delta R / (R \times \varepsilon)$, where R, ΔR, L, ΔL, and ε represent the resistance, the change in resistance, the length, the change in length and the applied strain of the tested material, respectively. The value of F_G for the graphene sensing element itself was 1.51, while the liquid metal wire had an F_G value close to zero, indicating that the liquid metal wires inside the device made little contribution to the total response of the sensor.

Another feature of the graphene strain sensor was demonstrated by applying the fabricated rosette sensor to detect strains in a multidirectional strain field. When a normal strain was applied to the rosette sensor, strains denoted as ε_{s1}, ε_{s2}, and ε_{s3} were developed in the three sensor sensing elements S1, S2, and S3, respectively. Figure 54(a) shows that the three sensing elements provided almost the same responses to strains applied along their own length directions, indicating good reproducibility of the fabrication processes for each element.

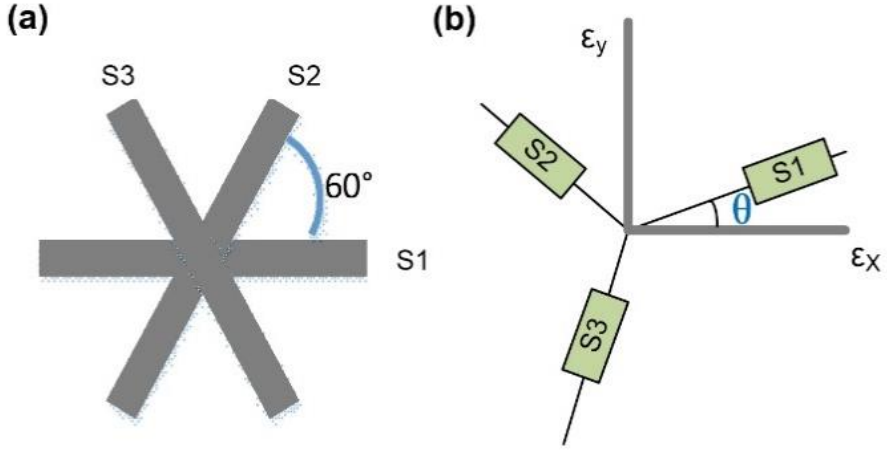

Figure 54. Rosette sensor: (a) S1, S2, and S3 graphene sensors stacked as a rosette gauge system, (b) schematic representation of graphene strain sensors arranged in rosette configuration indicating the direction of the principal axes

Figure 54(b) shows that when a 2.1% strain was applied to the sensor along a direction 5° clockwise from S1, the resistances of S1, S2, and S3 were increased by 2.18%, 0.77%, and 0.44%, respectively. In the coordinate system shown in Figure 54(b), εx and εy represent the strain components along x and y directions, respectively, of an applied strain. According to rosette gauge theory, when a primary strain is applied at an angle θ with respect to S1, as shown in Figure 54(b), the strains εs1, εs2, and εs3 experienced by S1, S2, and S3 can be represented by εx and εy as a function of θ, θ + 60°, and θ + 120°, respectively, based on equation (3):

$$\varepsilon_{si} = \frac{\varepsilon_x + \varepsilon_y}{2} + \frac{\varepsilon_x - \varepsilon_y}{2} cos2[\theta + (i-1)60^o] \qquad i = 1, 2, \text{and } 3 \tag{3}$$

Therefore, by measuring strain values ε_{s1}, ε_{s2}, and ε_{s3}, the orientation θ and the strains ε_x and ε_y can be found using equations (4) and (5), respectively (Starke et al. 2011):

$$\theta = \left(\frac{1}{2}\right) tan^{-1}\left((\sqrt{3}(\varepsilon_{s2} - \varepsilon_{s3}))/(2\varepsilon_{s1} - \varepsilon_{s2} - \varepsilon_{s3}) \right) \quad (4)$$

$$\varepsilon_{x,y} = \frac{\varepsilon_{s1}+\varepsilon_{s2}+\varepsilon_{s3}}{3} \pm \frac{\sqrt{2}}{3}\sqrt{(\varepsilon_{s1} - \varepsilon_{s2})^2 + (\varepsilon_{s2} - \varepsilon_{s3})^2 + (\varepsilon_{s3} - \varepsilon_{s2})^2} \quad (5)$$

where + and - indicate algebraically maximum ε_x and minimum ε_y strains, respectively. By mapping the resistance change of each sensing element onto strain values, the strains along the length directions of S_1, S_2, and S_3 were found to be ε_{S1} = 2.475%, ε_{S2} = 0.875%, and ε_{S3} = 0.5%, respectively. Furthermore, using equation (4), the angle θ was calculated to be 0.0897 (rad) or 5.14°, a deviation of only 2.8% from the real angle 5° of the applied strain. Similarly, using equation (5), the strain components ε_x and ε_y of the applied primary strain were found to be ε_x = 2.078% and ε_y = 0.488%. Based on the obtained ε_x and ε_y values, the calculated magnitude of the applied strain was 2.134%, a deviation of only 1.6% from that of the applied strain. This result indicates that the fabricated rosette graphene sensor could not only detect the strains applied in the directions along the sensing elements, but could also provide the magnitude and direction of the primary strain.

Graphene Strain and Pressure Sensors

Summary of the Work

A simple, reliable, and cost-effective method of fabricating wearable graphene-based physical sensors on adhesive tape was developed for detecting mechanical signals such as pressure, force, and strain. The device fabrication mainly involved two steps: (1) patterning the graphene by a repeated "sticking and peeling off" process using Scotch tape and (2) transferring the patterned graphene to another adhesive tape. Once a reusable mold has been formed by soft lithography, no further film deposition, lithography, or etching processes are required to obtain graphene-based wearable sensors. The strain and pressure sensors made on polyimide tapes can be used to track body motion and monitor pressure applied to a flexible object.

Literature Review

Wearable sensors have been widely used in real-time motion tracking and structural health monitoring, smart prosthetics, and humanized robotic systems. In particular, flexible mechanical sensors with high sensitivity and low cost, such as pressure and strain sensors, have attracted considerable attention. Mechanical flexibility is crucial in developing wearable sensors that must permit direct contact between the sensors and the sensed surfaces of objects with irregular shapes. Strain and pressure sensors based on conventional technology are generally fabricated on etched wafers of SiO_2 or glass that cannot provide adequate flexibility, reversibility, and a useful lifetime. To overcome these limitations, the use of a flexible substrate is attractive for providing a combination of appropriate mechanical structure and electrical performance for the sensing material. Many elastomer-based conductive composites have recently become popular materials for wearable mechanical sensors and are formed by introducing various conductive nanomaterials (e.g., carbon nanotubes or graphite) into flexible and stretchable elastomers (e.g.,

silicone, polyimide, or polyethylene); these materials exhibit good flexibility and electrical conductivity.

Additionally, due to its high piezoresistivity and stretchability, a two-dimensional material, graphene, has become a promising candidate for use in pressure and strain sensors formed on various flexible and stretchable substrates (Yao et al. 2012b, Lee et al. 2008).

The transduction mechanisms of pressure sensors are variously based on piezoresistivity, capacitance piezoelectricity, optics, etc. Currently, most commercial pressure sensors are made of membrane-based mechanical structures with high thickness, perhaps hundreds of nanometers. Piezoresistive sensors convert mechanical strain into resistance change. Unfortunately, their performance is limited by the bulk mechanical features of their materials, leading to low sensitivity, large Young's modulus, and long response times. To overcome such drawbacks, the sensing mechanism can be modified by adding contact resistance between the sensing film and the electrodes, but sensors using this approach are not capable of sensing high or low pressure extremes due to the lack of an elastic structure (Pan et al. 2013).

Another piezoresistive sensing mechanism is based on detecting the difference between the pressure within a reference cavity and the ambient pressure by measuring piezoresistance. The main drawback of such pressure difference sensing is the requirement of a stable reference cavity pressure during the entire lifetime of the sensor (Dolleman et al. 2016). Capacitive sensing is another transduction method used in pressure sensors in which an applied pressure causes parallel plates to deflect and change their capacitance. Because such capacitance changes resulting from the application of pressure tend to be very small, this kind of sensor provides only low sensitivity. Piezoelectricity is based on the occurrence of electric dipoles in solid materials (such as ceramics) that relate to the generation of an electrical charge generation in the material due to the applied pressure. In addition to the abovementioned transduction mechanisms, light intensity and wavelength are used as input signals for optical pressure sensors like those used in touchscreen-based devices such as smart phones or tablets. Frequency shift is a signal detected in resonant pressure sensors; when pressure is applied, the resonant element frequency changes due to a change in density distribution (Zang et al. 2015). Jiang et al. (2014) demonstrated a pressure sensor that includes graphene as a nanomechanical resonator and Si/ SiO_2 as a pressure membrane (Jiang et al. 2014).

Development of Strain and Pressure Sensor

To develop a graphene-based physical sensor, first an SU-8 mold was created using conventional soft photolithography. The desired channels (with 0.21 mm depths) were then created in PDMS by pouring the PDMS into an SU-8 mold, thermally curing, and peeling the PDMS from the mold. Then a graphene dispersion in a mixture of ethanol and distilled water (volume ratio of 70:30) was sonicated for 400 minutes and drop-cast into a PDMS mold pretreated with oxygen plasma (Liu et al. 2012). After drying for 5 minutes on a hotplate at 90°C, a graphene film covering the whole surface of the mold was formed, as shown in Figure 55(a).

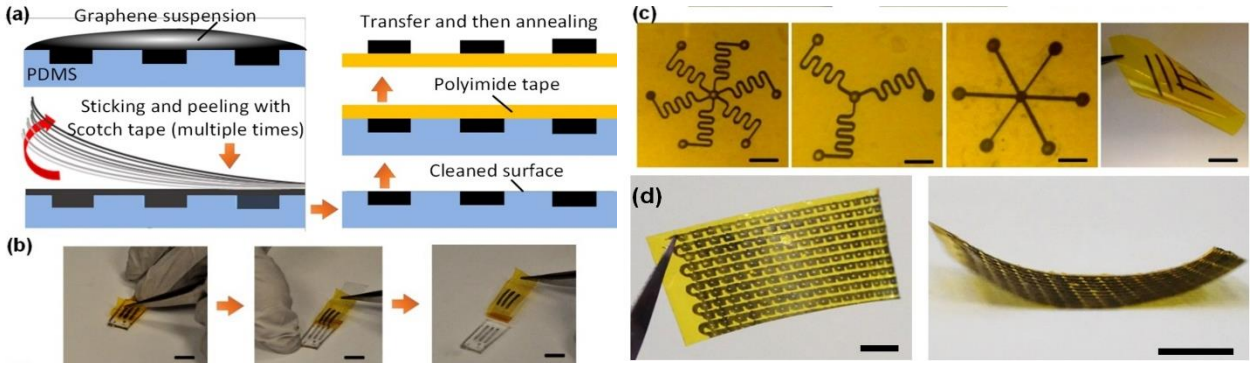

Figure 55. Development of strain and pressure sensor: (a) schematic of fabrication processes to make graphene sensors on adhesive tape; (b) photos showing how to transfer a graphene pattern onto a polyimide tape, with 4 mm scale bars, (c) fabricated graphene structures as an element, with 1 mm scale bars, (d) fabricated graphene structures as an array, with 3 mm scale bars

Subsequently, Scotch tape was used to stick and peel multiple times until all excess graphene was removed from the top surface of the PDMS mold, leaving the desired graphene to fill in the channels of the mold. Then another adhesive tape (in this case 25-µm-thick polyimide film with adhesive on one side) was laid flat and adhered to the PDMS mold, after which the whole structure was annealed for two hours in an oven at 200°C. The annealing treatment increased the electrical conductivity of the graphene patterns by about two orders of magnitude and strengthened the adhesion between the polyimide and the graphene. Finally, the thin polyimide tape was peeled from the mold and the conductive graphene patterns were transferred to the polyimide tape, as shown in Figure 55(b).

Figure 55(c) and Figure 55(d) show different array patterns and an element, respectively, formed on the tape. Figure 56 shows SEM images for the multilayer graphene patterns created on the polyimide tape. The images were captured to determine whether the adhesion between the graphene and the polyimide tape is sufficiently strong and the graphene film is continuous.

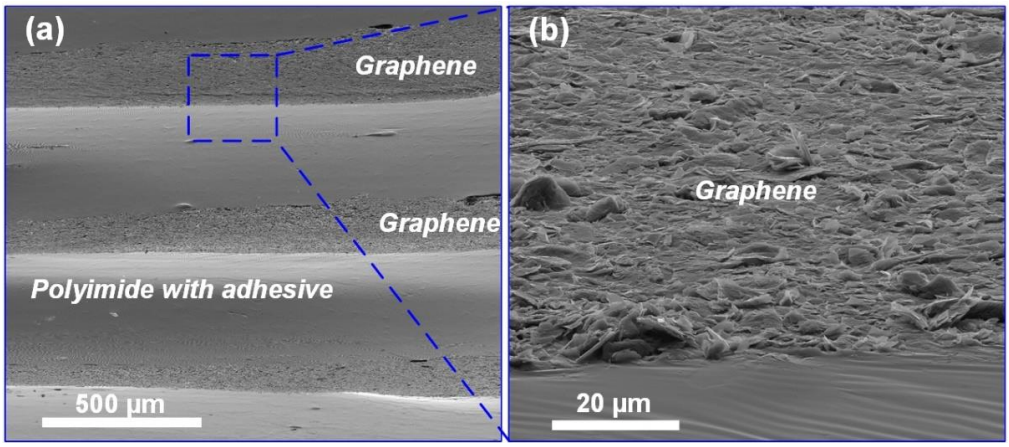

Figure 56. Scanning electron microscopy of the graphene patterns transferred onto a polyimide substrate

According to this analysis, continuous graphene film was formed on the polyimide tape with strong adhesion between them.

Key Findings and Results

This section presents test results demonstrating applications of graphene patterns as force, pressure, and strain sensors for body motion, finger force detection, and balloon pressure tracking. Figure 57(a) shows the relative resistance changes of the graphene sensor on the polyimide tape as a function of applied tensile strain along the length of the graphene pattern.

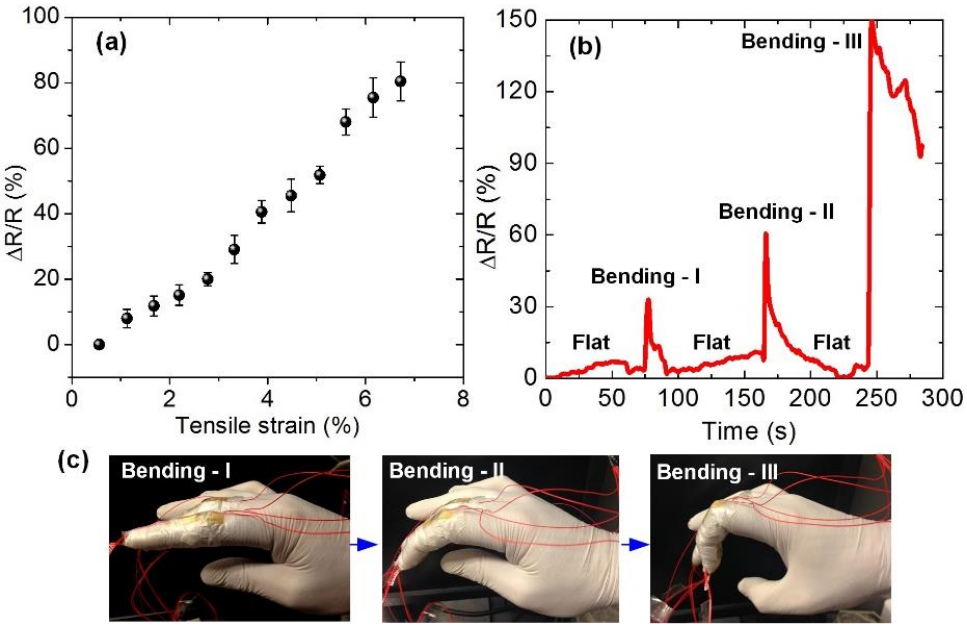

Figure 57. Graphene sensor test results: (a) relative resistance change as a function of tensile strain applied along the surface of polyimide tape, (b, c) demonstration of tracking motion of the index finger

The response of the sensor to tensile strain is almost linear. An index finger motion test was run by continuously bending the sensor at different angles.

The strain sensor was adhered to the middle joint of index finger, as shown in Figure 57(c), to track different bending positions of the finger. As the finger bent, the resistance of the sensor increased. Once the finger returned to a flat position from a bending position, the resistance correspondingly returned to its initial value, indicating that the sensor has good reversibility.

As another application of a graphene pattern sensor, the sensor was attached to the surface of a balloon to track dynamic changes in tension in the balloon during inflation (Figure 58). The air pressure was kept at 3 psi during the measurement while the duration of air flow to the balloon changed. Figure 58 shows that as the balloon was inflated, the resistance of the sensor increased. When the balloon remained at a given inflated state, the resistance became stable.

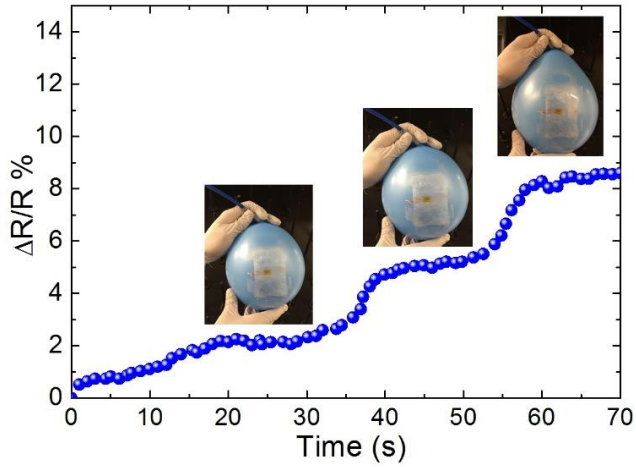

Figure 58. Demonstration of tracking changes in tension on a balloon during inflation

The graphene pattern formed on the tape can detect the pressure applied to the surface of the pattern. Figure 59(a) shows the relative resistance changes of the graphene sensor as a function of external pressure applied normally to the surface of the graphene pattern.

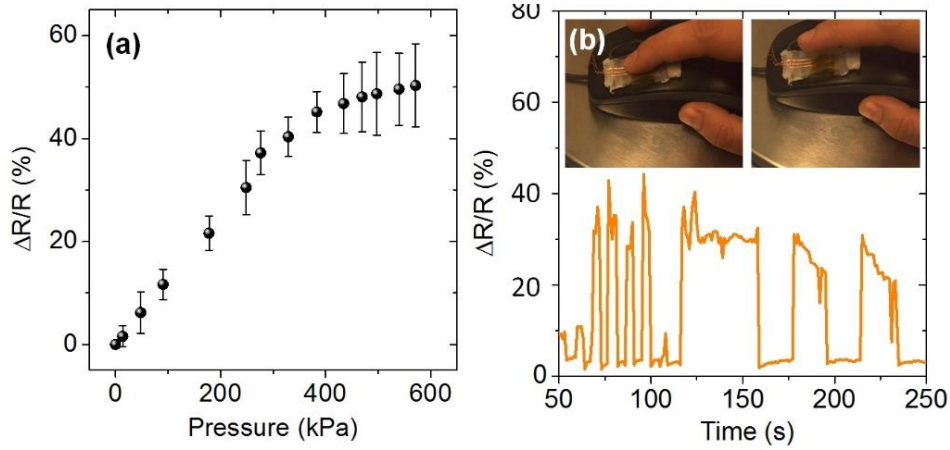

Figure 59. Detection of applied pressure to the surface of the graphene patterm: (a) relative resistance change as a function of pressure applied normally to the surface of the tape, (b) demonstration of tracking mouse click pressure and frequency

The mouse click pressure was monitored using a sensor attached to the left side of the mouse. When the mouse was clicked, the resistance of the sensor decreased, and when the clicking pressure increased, the relative resistance change increased. Figure 59(b) tracks how the sensor responded to different click pressures and frequencies.

Figure 60 demonstrates an approach that uses two sets of sensors (a total of 10 sensors) to track the bending and pressure levels involved in the action of catching a tennis ball bounced up from a hard floor.

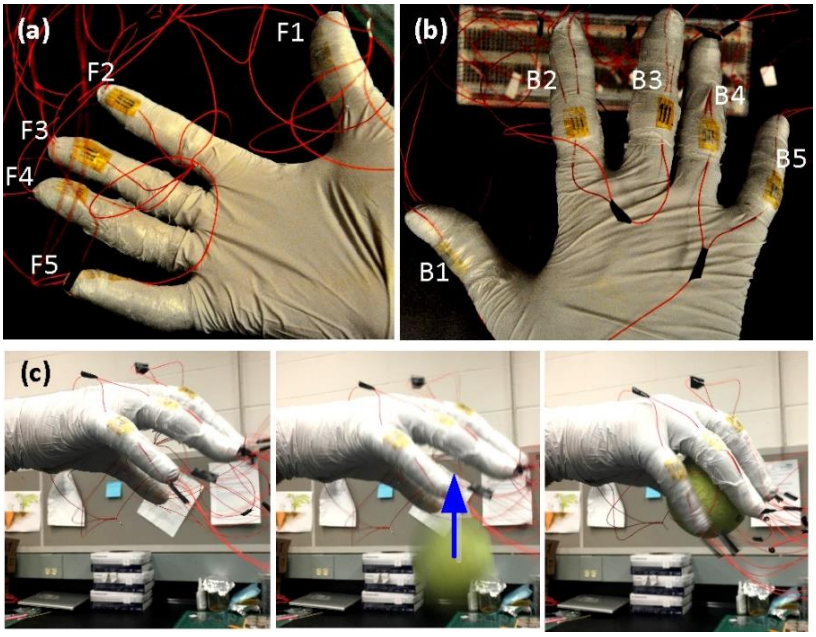

Figure 60. Using sensors to detect bending and pressure levels: (a, b) positions of five strain sensors (F1–F5) and five pressure sensors (B1–B5); (c) demonstration of tracking pressures and strains during the action of catching a tennis ball, with the pressure and strain signals read at three states: preparation (left), adjustment (middle), and catching (right)

Each finger was equipped with a strain sensor at the top of each finger joint and a pressure sensor at the fingertip. Table 3 shows the obtained pressure and strain values for the three states: preparation, adjustment, and catching.

Table 3. Relative resistance changes of five pressure sensors (F1–F5) and five strain sensors (B1–B5) attached to fingers during the action of catching a tennis ball

	Pressure (kPa)					**ΔR/R (%)**				
	F1	**F2**	**F3**	**F4**	**F5**	**B1**	**B2**	**B3**	**B4**	**B5**
Preparation	0	0	0	0	0	1.7	1.5	1.2	1.3	1.4
Adjustment	4.4	5	6.5	5.3	2.5	3.5	3.4	3.2	3.1	3.5
Catching	420	456	547	467	469	4.9	4.6	4.7	4.3	4.2

3D Graphene Sensors

Summary of the Work

A novel, simple, reliable, and low-cost method to form 3D graphene sensors using a microfluidic patterning fabrication method was developed. This method overcomes the limitations related to the complexity of fabricating patterned graphene film to provide a straightforward method that reduces the cost and time of fabrication. This section describes two different microfluidic

formations of 3D channel-structured graphene sensors: planar shaped (Figure 61) and helical shaped (Figure 62).

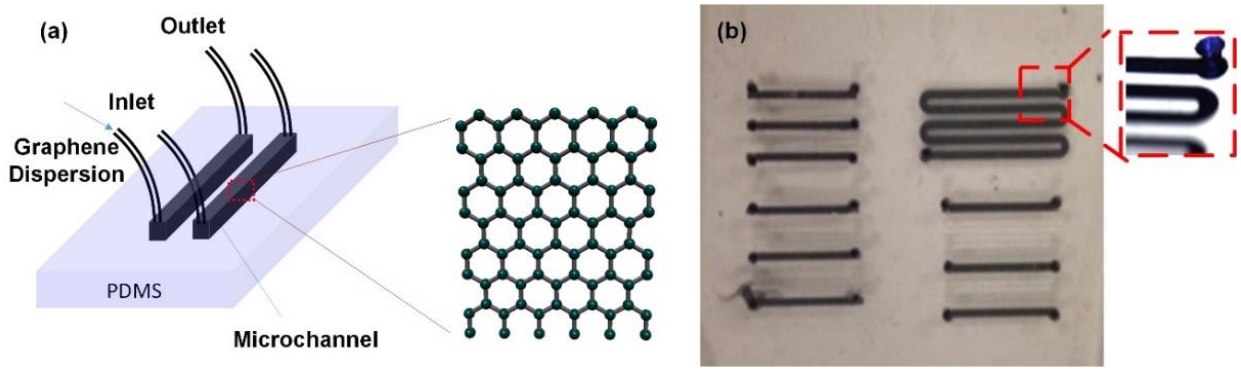

Figure 61. Planar structured graphene based strain sensor: (a) schematic of the planar structured graphene based strain sensor fabrication, (b) optical image of graphene based microfluidic sensor

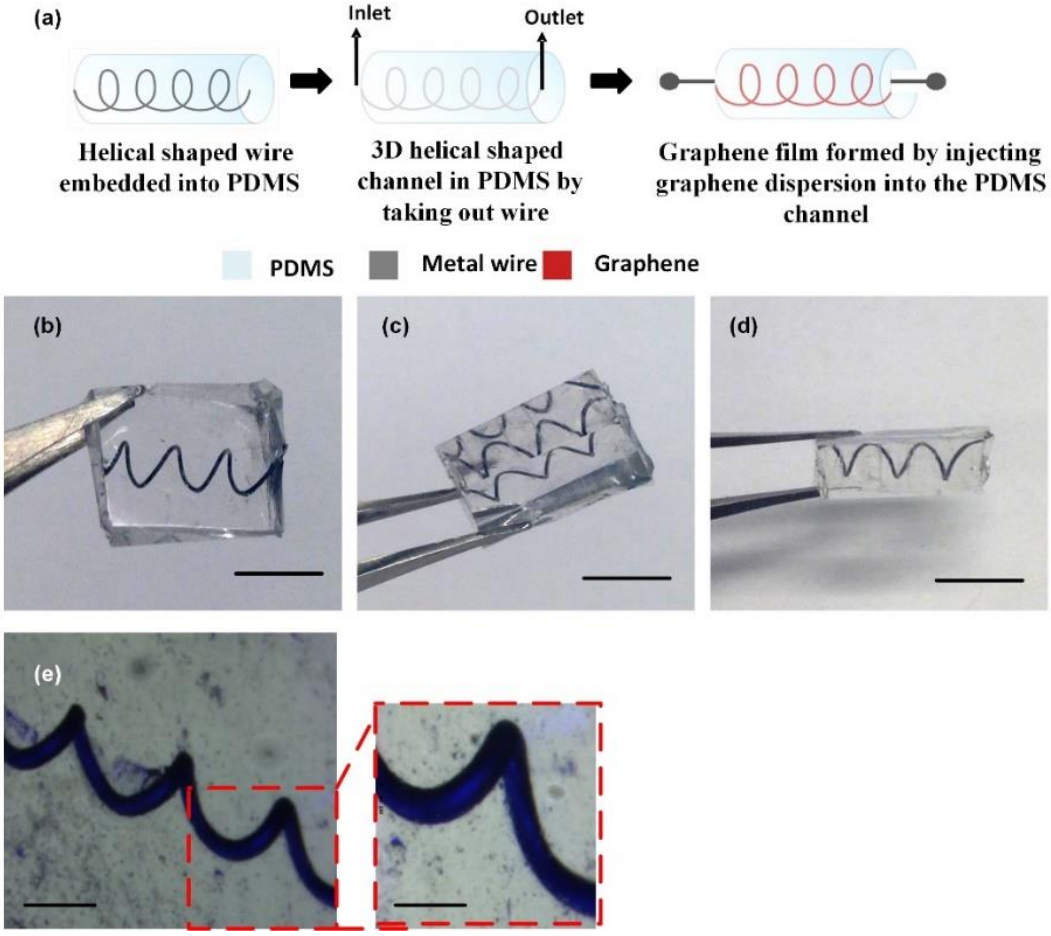

Figure 62. Helical-shaped graphene based strain sensor: (a) schematic of the 3D helical-shaped graphene based strain sensor fabrication, (b) top view, (c) 45° rotated, (d) 90° rotated, (e) microscope image of 3D helical-shaped sensor

In addition to the advantages mentioned above, this proposed novel fabrication method promises to provide a low-cost, reliable, genuine microfluidic fabrication and microchannel coating process. With the striking simplicity of the fabrication method as well as low cost and reliable fabrication, this method provides two more crucial improvements for strain sensing. First, 3D helical-shaped microchannels are fabricated using a simple and time-saving method that eliminates the most challenging step of microfluidic channel fabrication, i.e., photolithography. These improvements cannot be achieved with other recent microfluidic device fabrication methods. Second, the 3D helical structure is similar to a spring, with compressible and stretchable features that provide the proposed microfluidic formatted 3D graphene sensor with a large working range.

Literature Review

Graphene and its related materials (e.g., GO) have attracted increasing interest for use in many sensor applications due to their exceptional optical, electrical, mechanical, and chemical properties (Yao et al. 2012b). Graphene has been used for strain, pressure, and stress sensing because of its good mechanical properties (Mkhoyan et al. 2009). Its piezoresistance response, excellent stretchability, and high conductivity make graphene the best candidate for strain sensor use. Also, the dispersion behavior of graphene in many solvents allows it to be deposited onto wide ranging substrates in the form of thin films (Eda et al. 2008). Spin coating, drop-casting, spray coating, and chemical vapor deposition methods have been studied and found to create continuous graphene films on different substrates. Chemical vapor deposition has also emerged as an important method for the preparation and production of graphene films for various applications. In contrast, existing solution-based film formation methods allow the formation of films or basic patterns over only a small area, with small numbers of patterns able to be created simultaneously. These limitations keep these methods from being favored for sensor fabrication. These methods can also require highly expensive equipment because of complex fabrication processes that include a sequence of steps in which one small mistake may require fabrication to be restarted, leading to wasted time and additional cost.

Development of 3D Strain Sensor

Graphene was dispersed by exfoliating graphene powder using sonication for 400 minutes in ethanol and DI water at a ratio of 20 mg graphene/1 ml solution (0.7 ml ethanol and 0.3 ml DI water). For planar and helical-shaped channel formation, the desired wire shape was embedded into liquid phase PDMS and cured until the PDMS became solid. The wire was then removed gently from the PDMS to form a channel in the solid PDMS, following the same process as that used in convenient microfluidic fabrication methods that cannot provide 3D channel formation. The prepared graphene dispersion was then injected into the microchannels, forming a uniform and conductive internal film. Figure 61 and Figure 62 show planar and helical-shaped channels, respectively.

For graphene film characterization, the main parameters affecting the formation of conductive and uniform graphene film in microchannels are the concentration of the graphene dispersion, the time it takes to inject the graphene dispersion into a channel, and the temperature and

duration of the annealing treatment to improve graphene film conductivity. The experimental studies conducted for this project show that a single flow of dispersion with a ratio of 20 mg graphene/1 ml solution (0.7 ml ethanol and 0.3 ml DI water) into the channel gives the best results in terms of yielding films with high conductivity and uniformity, using an annealing treatment at 200°C for 3 hours. Along with film conductivity and uniformity, the adhesion between the PDMS and the graphene was also considered. SEM images taken from both the top and the cross-section of the graphene-coated microchannels show that the injected graphene dispersion forms a continuous film on the inside wall and inlet/outlet of the microchannels; this is crucial for the sensor to sustain different levels of compression and tensile strain (Figure 63).

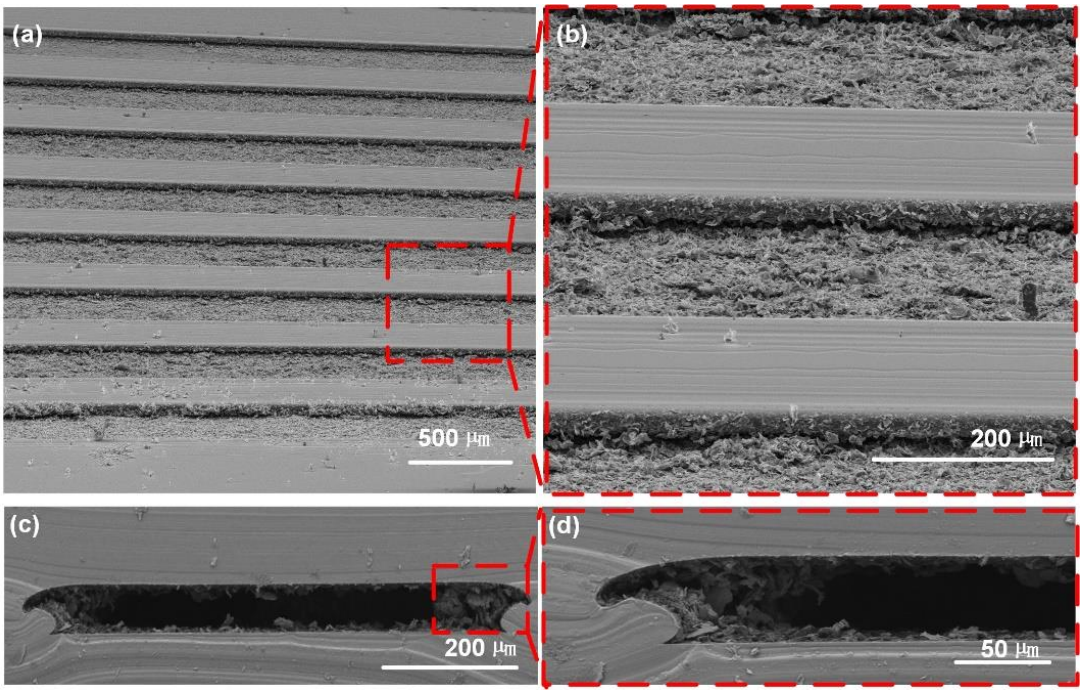

Figure 63. SEM analysis of graphene film in channels: top view with a 75º tilted angle at (a) 500 µm and (b) 200 µm, cross-section of a microfluidic coated channel with graphene at (c) 200 µm and (d) 50 µm

Key Findings and Results

The test results for the proposed 3D planar and helical strain sensors are shown in Figure 64 and Figure 65, respectively. Both were subjected to different levels of tensile and compression strains at different time intervals to determine their responses in terms of resistance change and the speed at which they respond to applied strain. The planar sensor was tested first. The applied tensile strain was increased to 8% by stepwise increments of 0.6%, with 20-second intervals between each strain level. Resistance increased by 106% due to the applied 8% tensile strain, as shown in Figure 64(a).

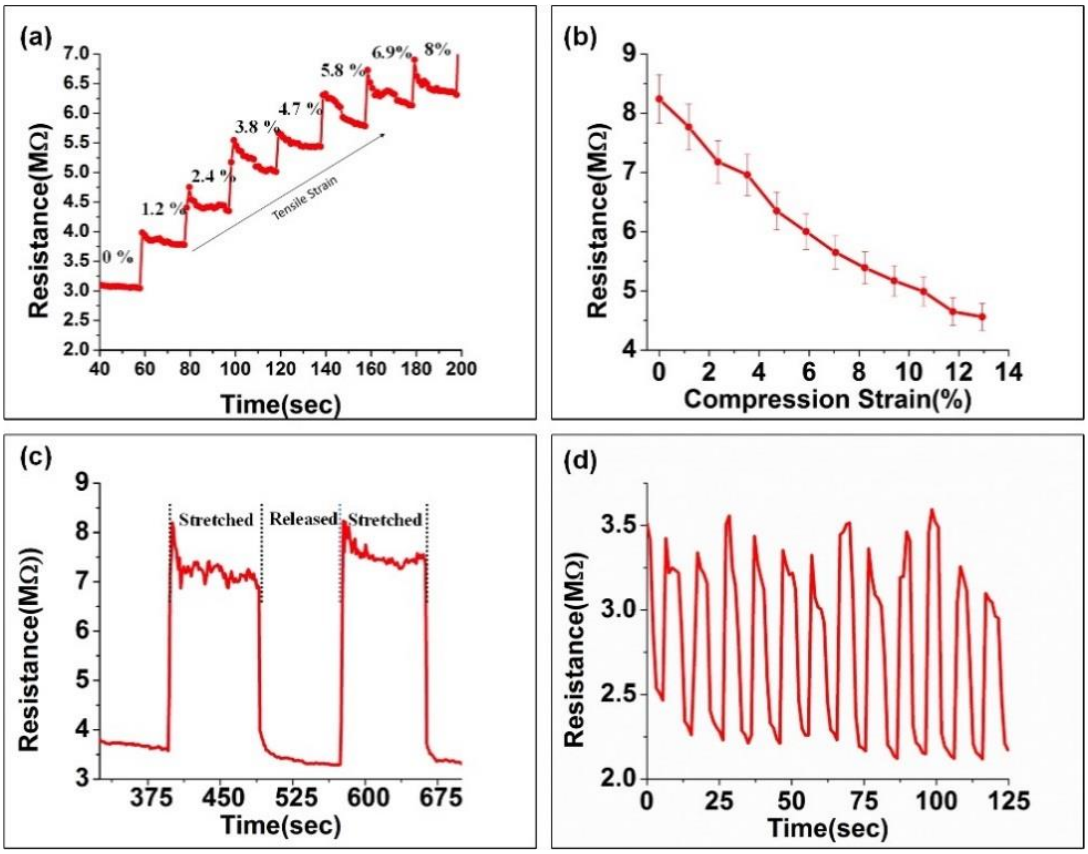

Figure 64. Resistance change response of planar-shaped sensor to (a) tensile strain (%), (b) applied compression strain (%), (c) stretching and releasing, (d) repeatability analysis involving stretching and releasing 25 times

Figure 64(b) presents the response of the sensor to compression, which decreases the resistance value. Resistance changed by 102% due to an applied 13% compression strain. For strain and pressure sensors, reversibility is an important parameter for producing accurate results, so the resistance change of the proposed planar sensor in response to stretching and releasing was tested, with a 100-second interval between each stretch and release cycle, as shown in Figure 64(c). The results show that the sensor returns to its initial state when it is released after being stretched. Repeatability and sustainability is still another critical parameter for sensors, and Figure 64(d) shows the sensor's response to stretching and releasing multiple times. The results illustrate that the sensor's response is still stable after 25 stretch and release cycles. Figure 64(d) also depicts the sensor's response time. As the figure shows, the sensor exhibits a very fast response of 4 seconds to changes in strain percentage level.

Similarly, the responses of the 3D helical-shaped sensors were measured, as shown in Figure 65.

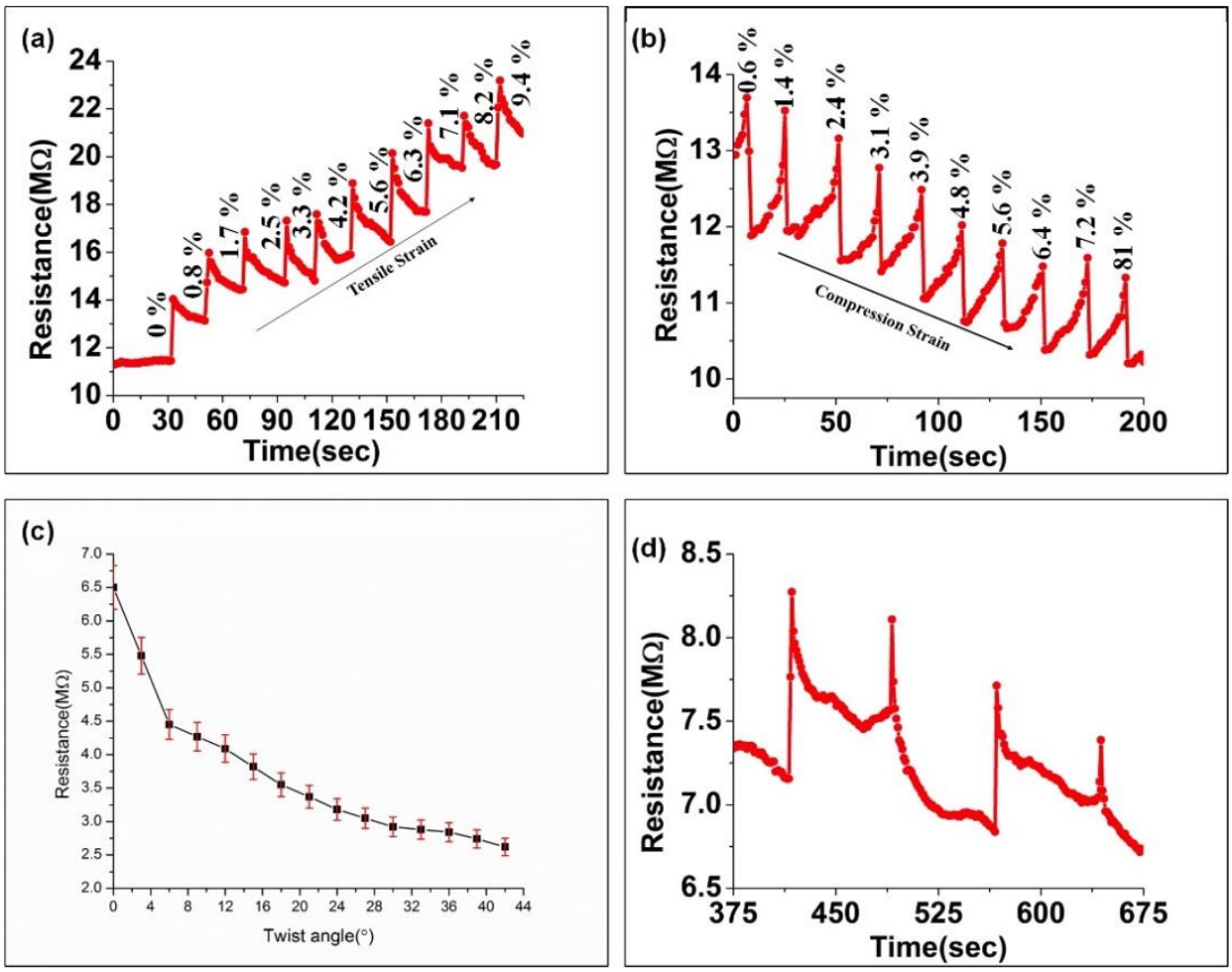

Figure 65. Resistance change response of 3D helical-shaped sensor to (a) tensile strain (%), (b) compression strain (%), (c) twisting effects, (d) stretching and releasing

Compared to the planar-shaped sensor, the 3D helical-shaped structure requires the sensor to sustain more strain and compression; while planar-shaped sensors can measure strains up to 8%, the helical-shaped unit can measure strains up to 9.4% with greater sensitivity. In addition to this advantage, the 3D helical-shaped sensor is also much more sensitive to twisting effects than the planar-structured sensor, which is not capable of sensing the tensile and compression strain from all directions.

MEMS-BASED TEMPERATURE SENSORS

Figure 66 is a schematic drawing of both a temperature sensor and a moisture sensor fabricated on a single substrate. Similar to the process used to create the moisture sensor substrate, the microfabrication protocol used to create this sensor is adaptable to large-scale manufacturing.

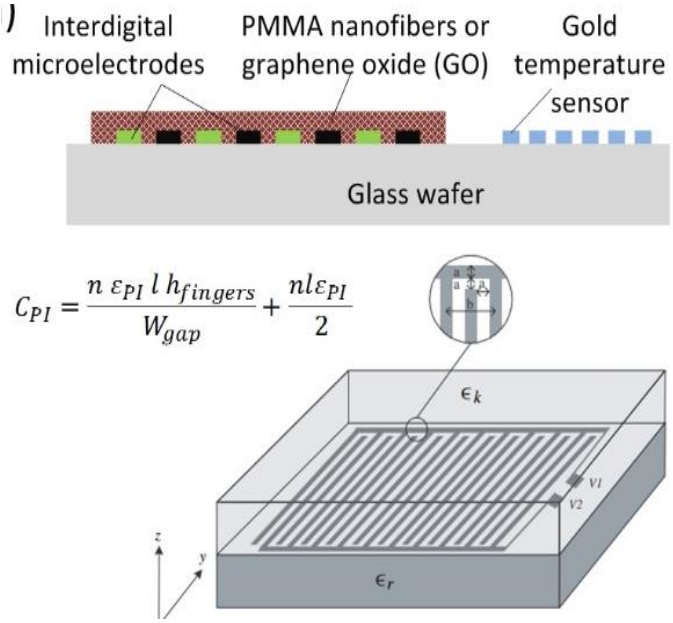

Figure 66. Structure of a multifunction MEMS sensor for measuring both moisture and temperature

The fabrication process for the temperature sensor is as follows:

- Substrates were prepared at Iowa State University's MRC. Preparation included the following steps:
  - Standard cleaning (2% HCl and DI water)
  - Use of evaporation to coat 100-nm-thick Al film onto the surface of glass slides
- Al electrodes were patterned in a MEMS laboratory administered by Associate Professor of Electrical and Computer Engineering Liang Dong using the following procedure:
  - Bake before spin coating for 5 minutes at 95°C.
  - Spin coat HDMS for 5 seconds at 500 rpm and then for 45 seconds at 4000 rpm.
  - Spin coat AZ photoresist for 5 seconds at 500 rpm and then for 45 seconds at 4000 rpm.
  - Pre-bake at 95°C for 45 seconds.
  - Expose to UV light at an intensity of 8 mW/cm^2.
  - Post-bake for 3 minutes at 90°C.
  - Immerse the slides into developer for 3 minutes.
  - Immerse the slides into aluminum etchant for 4 minutes.
  - Rinse with DI water.
  - Remove any remaining photoresist using ethanol.

To support fabrication on a silicon water, a photomask for the temperature sensor was designed and fabricated using AutoCAD. The photomask is shown in Figure 67.

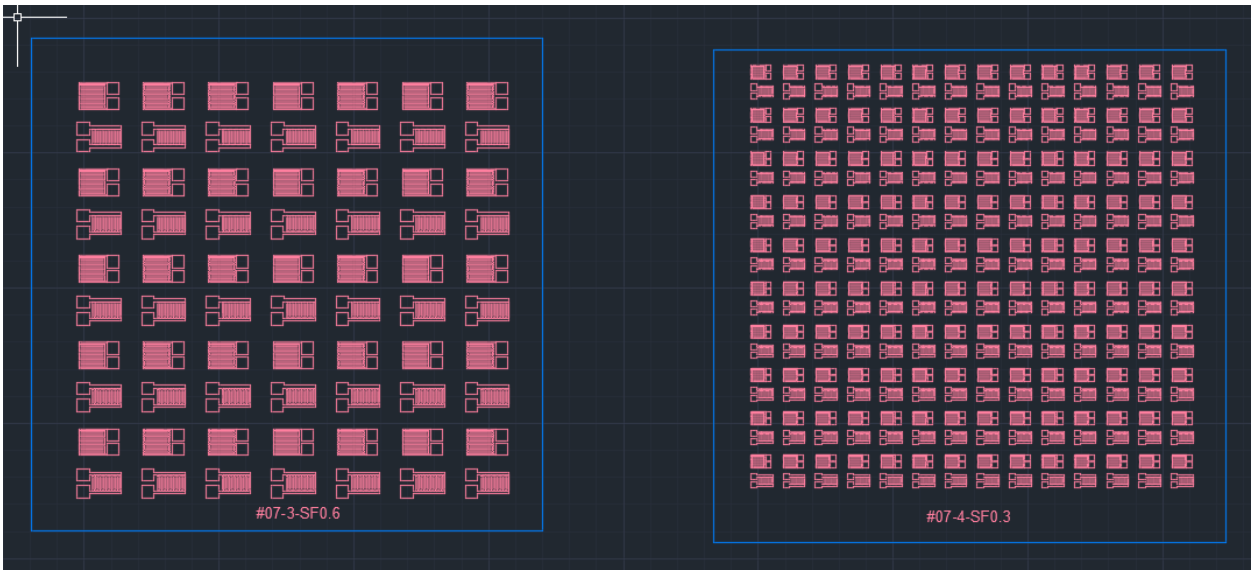

Figure 67. Photomask of temperature sensor

Temperature sensors of different sizes were designed for comparison; the design with a feature size of 1.8 mm produced the best results. Figure 68 shows the fabricated gold electrodes on a silicon wafer.

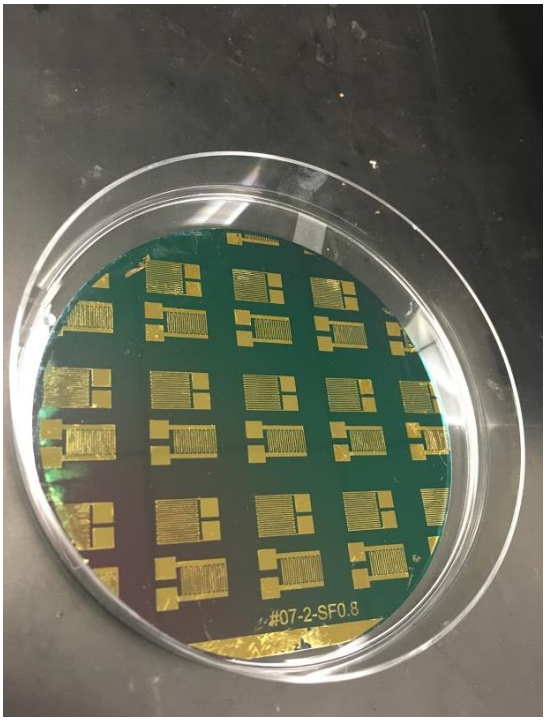

Figure 68. Fabricated temperature sensor on silicon wafer

For comparison purposes, sensors of other sizes were also fabricated during this test.

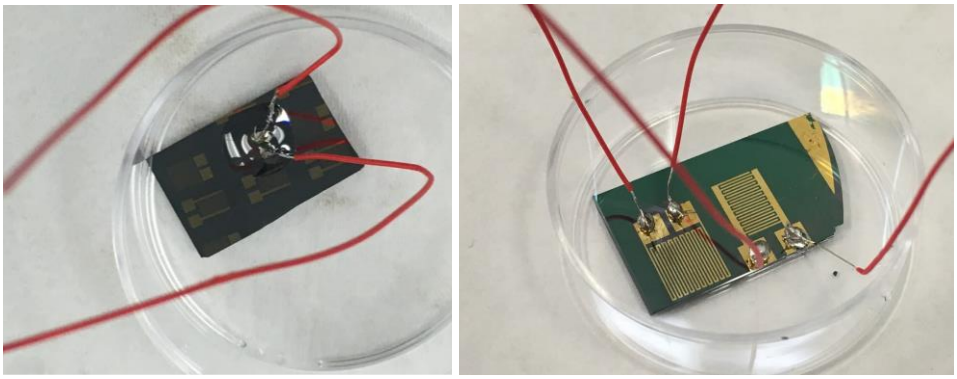

Figure 69. Different sizes of fabricated temperature sensors on silicon substrate

To test sensor response, the sensor was directly embedded into a mortar sample. The resistance reading from the sensor showed a linear relationship with the temperature of the mortar sample. The results of the temperature response test are presented in the following chapter, which describes testing in concrete samples.

PROTOTYPES OF MEMS SENSOR SYSTEMS

Temperature Sensors and Water Content Sensors

Both temperature and water content sensors were fabricated on a single substrate. To improve the sensor's lifespan, the top of the temperature sensor was protected by PDMS, while the water content sensor was directly exposed to concrete.

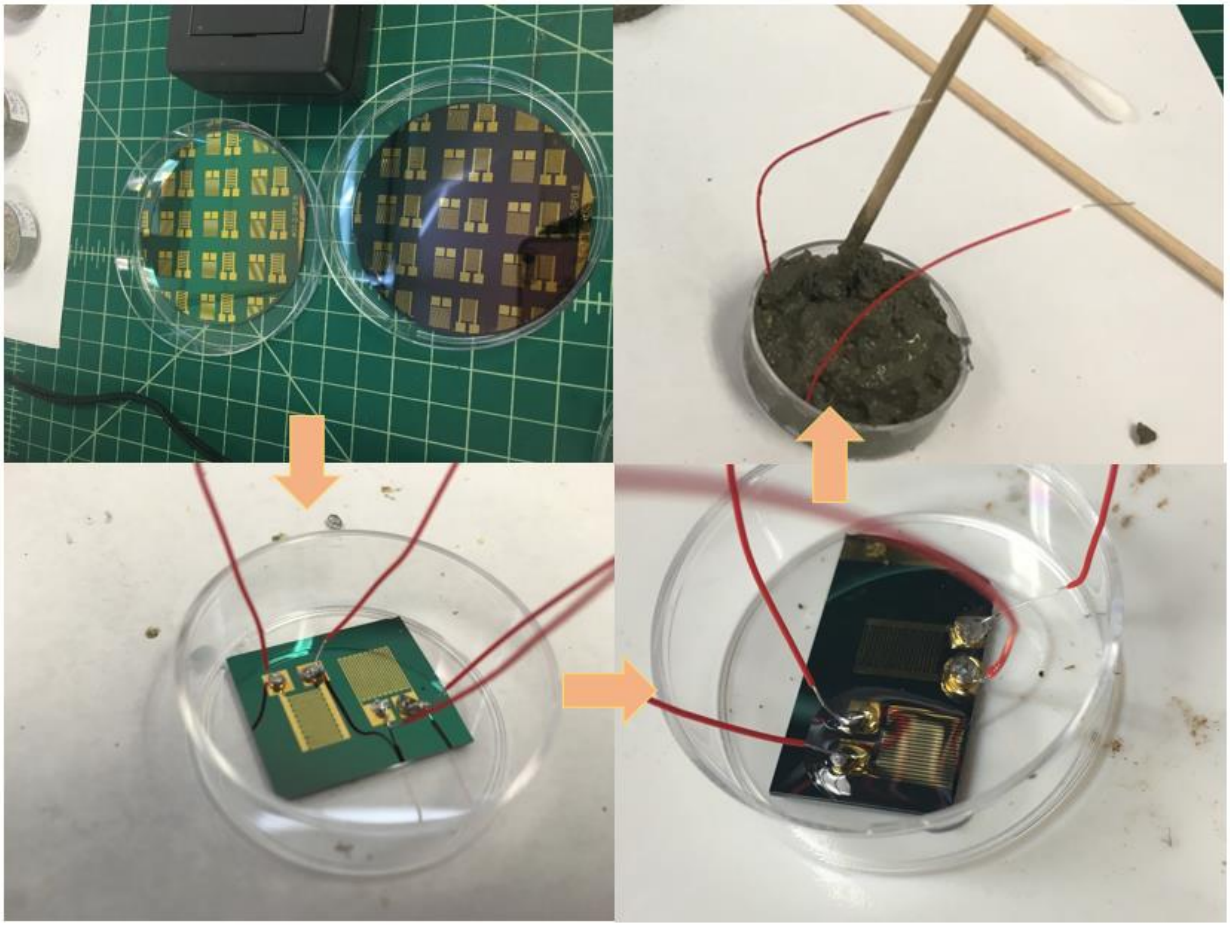

Figure 70. Installation of water content sensor and temperature sensor inside mortar

After the temperate sensor was installed inside the mortar, the mortar block was heated on a hotplate to change its temperature. The results shown in Figure 71provide resistance data reflecting sensor performance. The results indicate that the higher the temperature, the larger the sensor resistance.

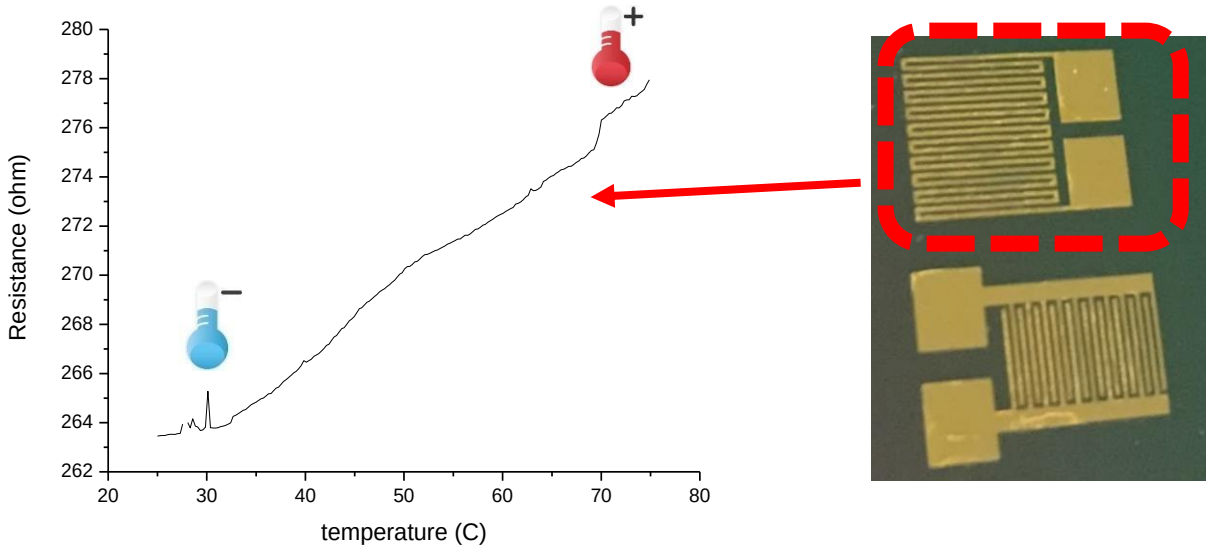

Figure 71. Resistance response of temperature sensor inside mortar versus temperature

The water content over time in the mortar was also tested, and the real-time results are shown in Figure 72 and Figure 73 for the water adding and water evaporation processes, respectively.

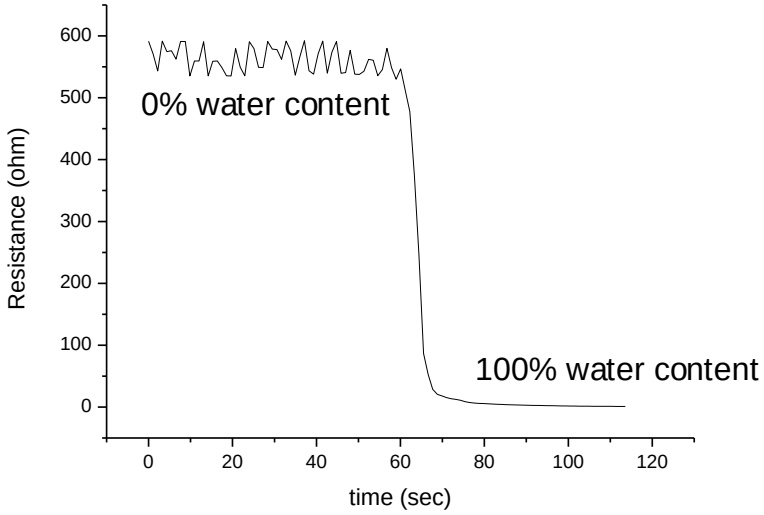

Figure 72. Resistance response of water content sensor when water was added at the 60th second

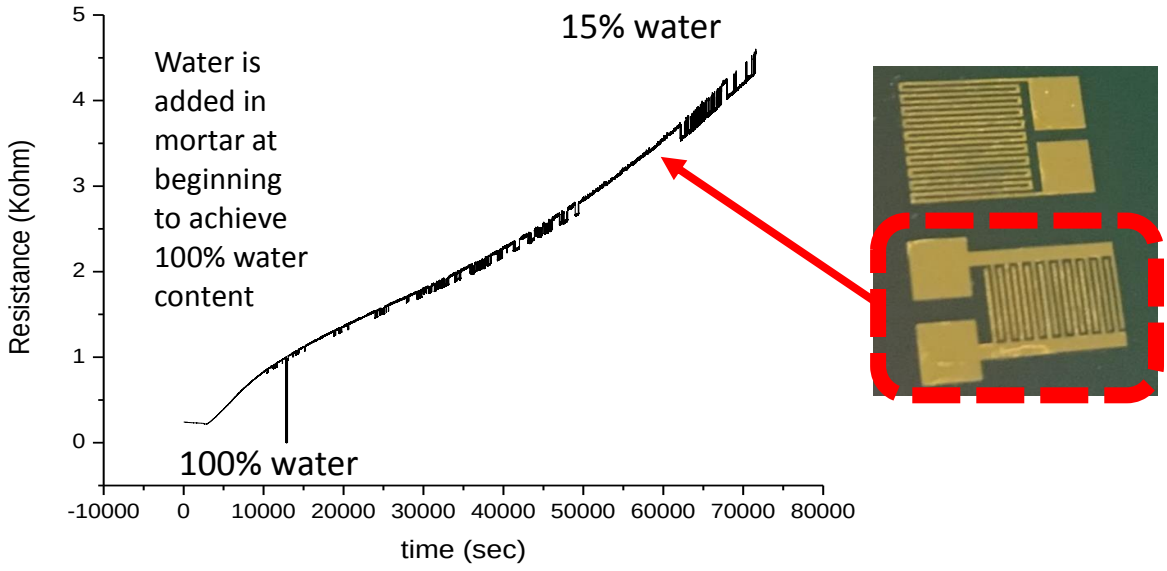

Figure 73. Resistance response of water content sensor inside mortar block over evaporation time

The water content inside the mortar sample evaporated over time, so the resistance response of the water content sensor followed the water content percentage over time. The longer the time elapsed from start, the lower the water content and the larger the sensor resistance.

The resistance of the water content sensor versus the actual water content percentage in the concrete sample was measured, and the results are shown in Figure 74.

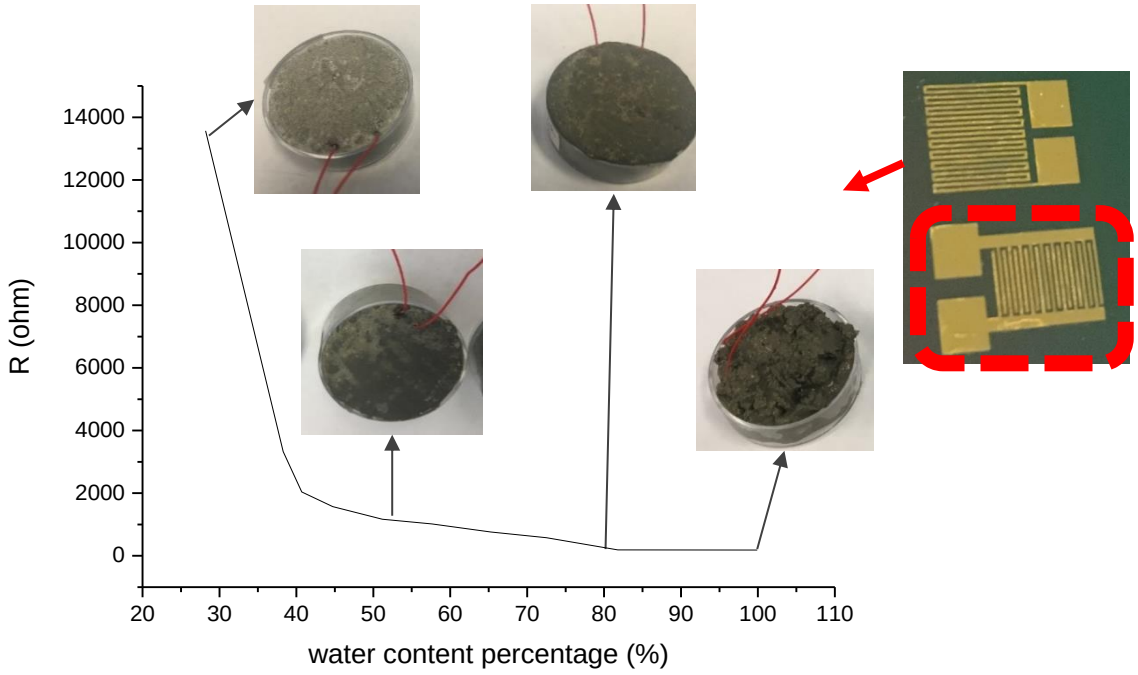

Figure 74. Resistance of water content sensor in mortar versus water content percentage

The actual water content was calculated from the weight of the total water added and the amount of evaporated water. The results show that the lower the water content, the higher the resistance of the water content sensor. These results are also consistent with the real-time water content monitoring plot.

Strain Sensors

Strain sensors were installed in both concrete and mortar for load and unload tests. Figure 75 shows the sensor installed on the surface of a concrete cylinder, inside a concrete cube where the sensor is fixed by two wooden sticks, and inside a concrete cube where the sensor is fixed on two metal mesh pieces.

Figure 75. Installation and testing of the unidirectional graphene strain sensor

Figure 75 depicts the installation and testing of the unidirectional graphene strain sensor with liquid metal interconnections in a concrete strain-sensing application. The sensor was horizontally attached to the surface of a concrete cylinder, and an external force was vertically loaded onto the cylinder. As the load was applied, the concrete cylinder reacted by expanding in the horizontal plane, so the sensor indicated a stretch strain as the concrete expanded. The resistance of the sensor and the force load on the concrete were both recorded. The testing results indicate that the sensors react in a pattern similar to the given load.

Figure 76 demonstrates the results of installing and testing the unidirectional graphene strain sensor with liquid metal interconnections in a concrete strain-sensing application.

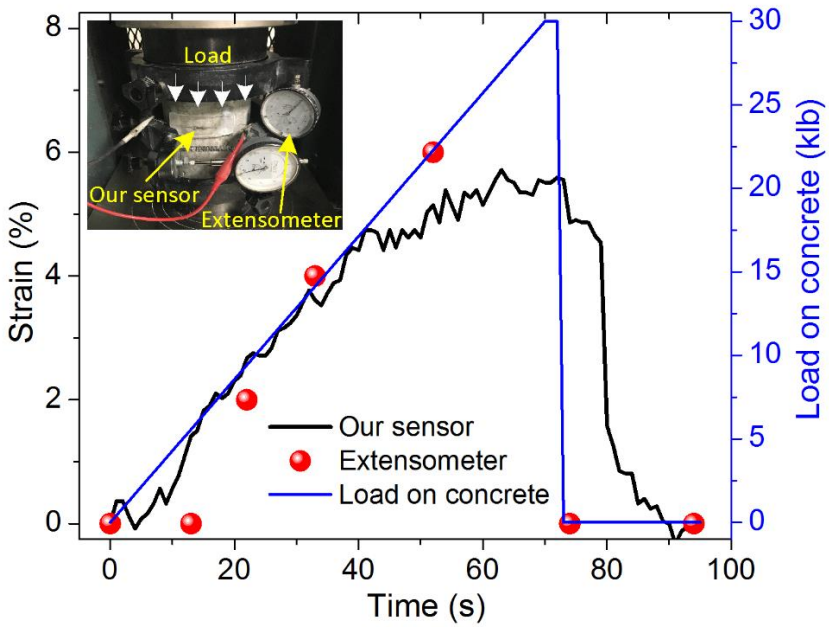

Figure 76. Unidirectional graphene strain sensor in a concrete strain-sensing application: (a) setup for monitoring strain changes of a concrete cylinder during loading and unloading processes, (b) relative resistance change and load on the concrete cylinder over a period of time (~140 seconds)

A 50 mm by 20 mm cut with a 3 mm by 9 mm graphene strip sensor was used because it was fully flexible and thus able to be horizontally attached at the curved surface of a concrete cylinder. Both the sensor's ends were glued to the concrete, and a commercial strain frame (4 in. × 8 in. compressometer-extensometer) was installed for strain calibration. An external force (from 0 to 30000 pounds) was vertically applied to the cylinder by a loading machine. As the load was applied, the concrete cylinder reacted by expanding in the horizontal plane, so the sensor detected a stretch strain as the concrete expanded. The resistance of the developed sensor, the readings from a commercial strain sensor, and the force load on the concrete were all recorded. The commercial sensor indicated a concrete surface perimeter expansion of up to 8%. When the concrete was subjected to tensile strain, the resistance reading from this sensor behaved consistently with the added load.

Smart Sensing System

A homemade wireless readout module for small-strain MEMS sensors was developed (Figure 77).

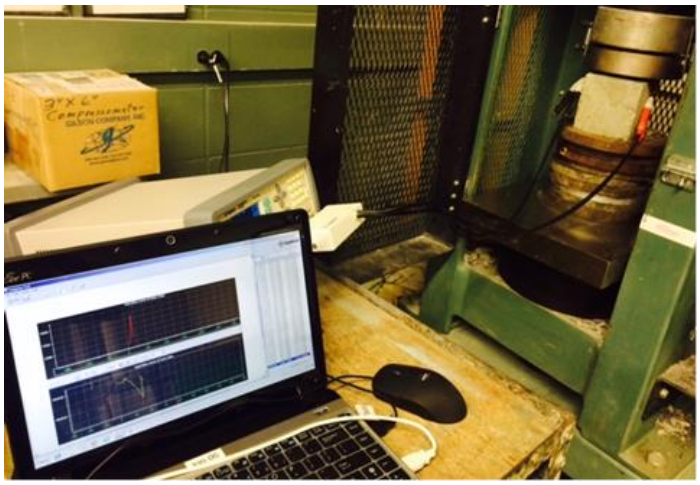

Figure 77. Wireless readout module for small-strain MEMS sensors

In this system, the maximum transmission distance was 50 m. The module read and transmitted data every 1 second and produced an output signal voltage ranging from 0 to 5 V. This system can display and record pressure signals via a PC, with multiple data type conversions in the following sequence: (1) the pressure is detected by the sensor inside the concrete (pressure signal), (2) the signal goes to the readout circuit (resistance signal), (3) the signal is transmitted wirelessly (voltage signal), (4) the signal goes to an XBee receiver (voltage signal), (5) the signal goes to the PC (pressure signal).

The wireless transmission system is based on an Arduino board (Redboard, Sparkfun Electronics) and an XBee receiver. The overall concept sketch is presented in the Figure 78.

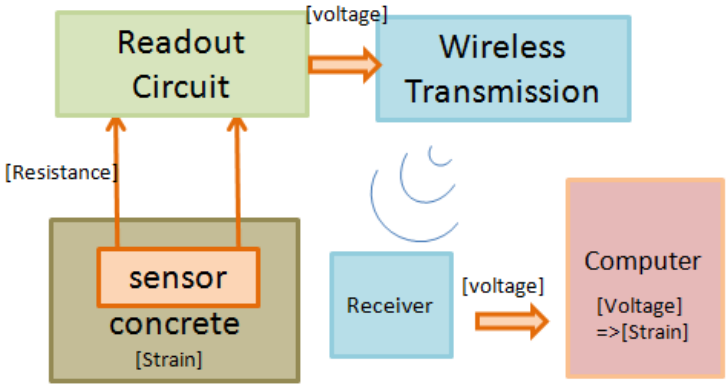

Figure 78. Concept sketch of wireless transmission

The sensor was first placed inside a concrete cube with extra protection at the contacts, and resistance was read through the output wires, as shown in Figure 79.

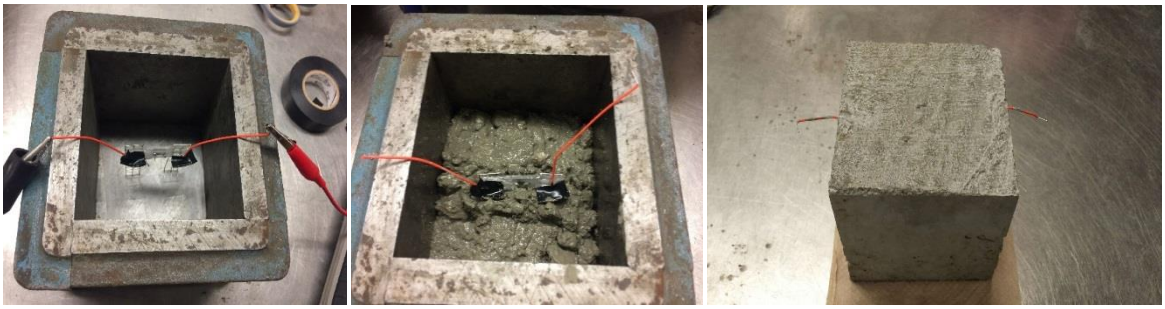

Figure 79. Strain sensor embedded in concrete specimen

A readout circuit was constructed to convert the resistance signal to a voltage signal between 0 and 5 V that can be read by the wireless transmission device. The readout circuit is based on a Wheatstone bridge configuration and can be followed by an optional amplifier. A potentiometer is provided to support calibration of the offset installation resistance difference between the sensors. The readout circuit and amplifier are shown in Figure 80.

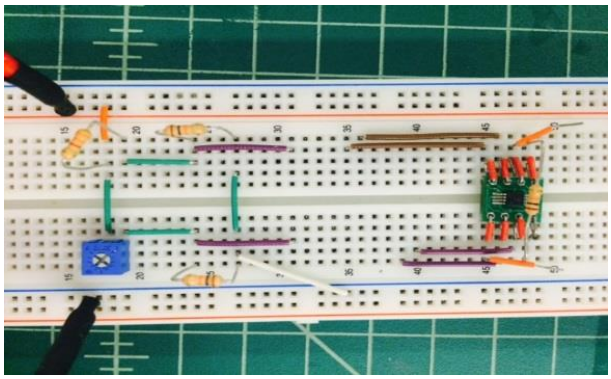

Figure 80. Readout circuit and amplifier in breadboard

As noted above, the readout circuit was built using a Wheatstone bridge readout circuit structure and can be followed by an optional amplifier. This circuit accepts input resistance values ranging from 4 kOhm to 40 kOhm, with the resistance change range corresponding to a strain of 1% to 10%. The output of the circuit is 0 to 5 V. This circuit contains two fixed resistors (560 Ohm) and one potentiometer (0 to10 kOhm) that can be used to adjust the voltage starting from 0 to 5 V to calibrate the initial strain level of the graphene during installation.

The wireless transmission follows the readout circuit, with the data receiver attached to a computer through a standard USB connection. At the computer, the received voltage signal is converted back into strain information. The overall system is shown in Figure 81.

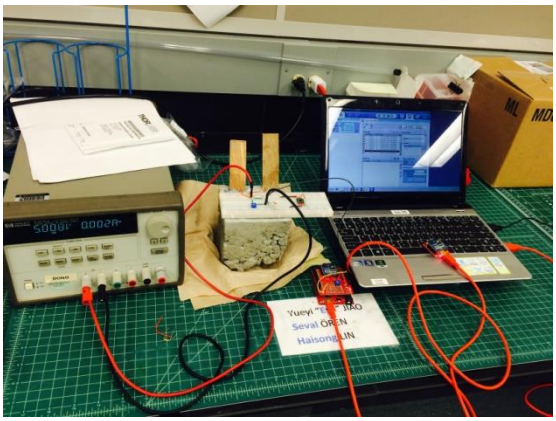

Figure 81. Wireless transmission with Arduino-controlled XBee receiver

Table 4 illustrates the cost estimation for the strain sensor with the wireless transmission component.

Table 4. Cost approximation of strain sensor with wireless transmission component

Item	Unit Cost ($)	100+ Units Cost ($)*
Liquid metal	2.06	2.06
Graphene	5.56	5.56
PDMS	0.93	0.68
Metal connection	2.19	1.75
$FeCl_3$	0.13	0.02
Arduino RedBoard	4.99	4.24
1x XBee Shield	3.74	3.18
1x XBee Explorer USB	N/A	N/A
2x XBee Modules	12.48	11.32
1x Arduino stackable header kit	0.38	0.34
Box	8.95	8.95
Wires and resistors	0.87	0.68
Power	N/A	N/A
Electrical insulating tape	0.02	0.02
Sum	**$42.30**	**$38.80**

* Unit price of the item for orders over 100 units

SUMMARY AND RECOMMENDATIONS

Key Findings

The findings from this study can be summarized as follows:

Overall MEMS-Based Sensor Development

- Seven types of MEMS sensors were developed in this research for measuring moisture, temperature, strain, and pressure in concrete: (1) nanofiber-based moisture sensors, (2) GO-based moisture sensors, (3) flexible graphene strain sensors with liquid metal interconnections, (4) graphene strain and pressure sensors, (5) 3D planar and helical-shaped graphene strain sensors, (6) temperature sensors, and (7) water content sensors. In addition, MEMS temperature sensors and MEMS water content sensors were integrated into one sensing unit as a multifunctional sensor. A wireless signal transmission system was built for collecting MEMS sensor signal readings.

- The nanofiber-based moisture sensor is a novel relative humidity/moisture sensor with a sensitivity about three times higher than that of conventional moisture sensors.

- The GO-based moisture sensor exhibits a high sensitivity to humidity with a short transient response time and good repeatability. It is a cost-effective method for forming large-area GO films for sensing applications.

- The flexible graphene strain sensor with liquid metal interconnections can measure either unidirectional or multidirectional strain changes in concrete.

- The graphene-based medium-strain and pressure sensors on polyimide adhesive tape have the unique advantages of easy installation, structural flexibility, and simple cost-effective fabrication procedures.

- The 3D planar and helical-shaped graphene large-strain sensors have the capability to sense applied strain and pressure from all directions.

- The different sizes of the developed MEMS-based temperature sensors can be used either as single sensors or as part of a multifunctional sensor system.

- A multifunctional MEMS system developed using these sensor techniques can simultaneously measure both temperature and water content inside concrete.

- An in-house wireless signal transmission system built to read MEMS sensor signals demonstrated reliable communication at distances of up to 160 ft.

MEMS-Based Moisture Sensors

- The key findings regarding the nanofiber-based moisture sensors are as follows:

    - A novel relative humidity/moisture sensor with a sensitivity about three times higher than that of conventional moisture sensors was developed.
    - The moisture sensor's structure was successfully transitioned from a parallel plate capacitor (PPC) configuration to a planar interdigital capacitor (PIC) configuration.
    - Nanofibers were successfully fabricated with a low concentration of PMMA solution. The diameter and shape of the fibers resulting from different concentrations were studied using SEM photographs.
    - The reaction speed of the developed moisture sensor is three seconds, which is quicker than most conventional moisture sensors.
    - The capacitance is linearly proportional to environmental humidity level, and the rate dose is not affected by temperature.

- Impedance-based analysis showed that a GO-based sensor exhibits a high sensitivity to humidity with a short transient response time and good repeatability. This research provides an effective and low-cost method for forming large-area GO films for sensing applications. Key findings regarding this sensor are as follows:

    - The developed SSC method produced a uniform GO coating on 8 in. diameter wafers, thus overcoming technological barriers to obtaining large arrays of sensors at a low cost.
    - The developed GO coating method significantly improved the capability of batch-fabricating GO sensors with a uniform performance distribution over a large area, thus minimizing the need for sensor calibration.

MEMS-Based Strain Sensors

- The key findings regarding the flexible graphene strain sensor with liquid metal interconnections and wiring are as follows:

    - The developed strain sensors were made using flexible materials, including graphene, liquid metal, and elastomer.
    - Flexible liquid metal interconnections for strain sensors were used as an interconnection material for patterned graphene.
    - A unidirectional strain sensor was developed and tested both inside and on the surface of a concrete cylinder.
    - The proposed strain sensor design allows for enhanced structural flexibility and reliability and a reduced risk of connection- and wiring-induced failures.
    - A multidirectional rosette-type strain sensor capable of measuring strains in a multidirectional strain field was developed.

- The key findings regarding the MEMS-based strain sensor on polyimide tape are as follows:

- A patterned graphene strain and pressure sensing unit was fabricated using only a "sticking and peeling off" process, which is a simple, reliable, and cost effective fabrication method.
- Form strain sensors based on inexpensive Kapton polyimide tape with silicone adhesive are compatible with a wide temperature range of up to 269°C.
- An annealing process was developed to further improve the adhesion of the tape, thereby facilitating sensor installation.
- Submicron-scale feature resolution of strain-sensitive graphene was achieved, giving a potential mechanism for feasibly measuring 3D strain distribution with a high spatial resolution.

- The key findings regarding the MEMS 3D helical strain sensor are as follows:

  - A microfluidic-based fabrication process was developed to obtain spiral graphene structures for large strain and torque measurements.
  - Sensors similar to springs were developed that had compressible and stretchable features and a large working range.

Prototypes of MEMS Sensor Systems

- The key findings regarding the MEMS multifunctional sensor system for temperature and water content measurements are as follows:

  - An easy and cost effective fabrication process was developed to fabricate both temperature and water content sensors in a single substrate.
  - A sensor with a fast response to the temperature of the sample (within 1 second) was embedded inside a mortar sample.

- The key findings regarding the wireless MEMS strain sensor system are as follows:

  - A wireless signal transmission system was built for data center signal transmission from sensors embedded inside concrete.

Recommendations

Based on the findings of this research, the following recommendations are proposed for future improvements and implementation of the MEMS-based sensors developed in this study for pavement infrastructure systems:

- Future research directions for MEMS-based transportation infrastructure research applications include the development of a chloride ion detection sensor for monitoring rust-inducing salts in concrete structures, detection of wrong-way vehicle entry, overcoming

challenges to pavement health monitoring using smart sensing technologies, and cost evaluation of smart pavement health monitoring systems.

- The proposed SSC method allows for the large-scale fabrication of moisture sensing elements. This technology overcomes the technological barriers of existing fabrication methods to create large arrays of sensors and may be moved into industrial semiconductor manufacturing process lines for the large-scale manufacturing of GO-based sensors for structural health monitoring systems.

- The proposed method for patterning graphene on a highly stable polyimide tape provides an opportunity to fabricate submicron-scale elements or array sensing units. The ability to make microscale sensors on tape will facilitate sensor installation and the measurement of strain and other important parameters on the surface of structures. Embedding such sensors into the concrete is also feasible. The submicron-scale feature resolution of strain-sensitive graphene gives a potential mechanism for feasibly measuring 3D strain distribution with a high spatial resolution.

- With a high electrospinning speed, a thinner PDMS substrate can be produced for use in strain sensors to further improve sensor sensitivity and lower the cost.

- The fiber morphology of the nanofiber-based moisture sensor influences the sensor's stability. A sensor with very thick layers of PMMA fibers can be fabricated to minimize the influence of capacitance caused by morphology changes in the top-layer fibers.

- An array of flexible and even wearable strain sensors was developed for monitoring the 3D distribution of strains with a high spatiotemporal resolution.

- Investigation of a more effective assembly method will allow the developed sensing elements to be integrated into a single package for convenient installation and data readout, which may require, to some extent, involvement of the semiconductor and MEMS packaging industries.

The research team has been tasked with expanding the findings and accomplishments related to infrastructure health monitoring from the Phase I and Phase II studies into other areas of transportation infrastructure systems, such as the following, in future research efforts:

- Flexible and composite pavement systems
- Geo-foundation systems
- Bridge structures and systems
- Mass concrete applications
- Construction quality control (QC) and quality assurance (QA)
- Construction management
- Critical infrastructure condition monitoring and pre-alert systems
- Monitoring of viaducts, drainage, and water channels

- Applications in unpaved and low-volume county and city roads, such as determining freezing and thawing cycles and thawing periods using sensor systems, spring load restriction (SLR) guidance based on sensor data, and other applications
- Overweight/heavy vehicle loading pre-alert and detection systems
- Detection of pavement reflection cracking using radio frequency identification (RFID)–based sensors
- Management of difficult-to-locate transportation assets using RFID-based and other sensors
- Use of smart sensors and systems in vehicle-to-vehicle and vehicle-to-infrastructure control

REFERENCES

Bae, S., H., Y. Lee, B. K. Sharma, H. J. Lee, J. H. Kim, and J. H. Ahn. 2013. Graphene-based transparent strain sensor. *Carbon* 51: 236-242.

Bi, H., K. Yin, X. Xie, J. Ji, S. Wan, L. Sun, M. Terrones, and M. S. Dresselhaus. 2013. Ultrahigh humidity sensitivity of graphene oxide. *Scientific Reports* 3(2714).

Chang, H., S. Zhenhua, Q. Yuan, and Z. Zheng. 2010. Thin-film field effect phototransistors from bandgap-tunable, solution-processed, few-layer reduced graphene oxide films. *Advanced Materials* 22(43): 4872-4876.

Chatzandroulis, S., A. Tserepi, D. Goustouridis, P. Normand, and D. Tsoukalas. 2002. Fabrication of single crystal Si cantilevers using a dry release process and application in a capacitive-type humidity sensor. *Microelectronic Engineering* 61: 955-961.

Chen, Z., and C. Lu. 2005. Humidity sensors: a review of materials and mechanisms. *Sensor Letters 3*(4): 274-295.

Chiechi, R. C., E. A. Weiss, M. D. Dickey, and G. M. Whitesides. 2008. Eutectic Gallium-Indium (EGaIn): A moldable liquid metal for electrical characterization of self-assembled monolayers. *Angewandte Chemie* 120(1): 148-150.

Dolleman, R. J., D. Davidoviky, S. J. Cartamil-Bueno, H. S. J. Van der Zant, and P. G. Steeneken. 2016. Graphene squeeze film pressure sensors. *Nano Letters* 16: 568-571.

Dua, V., S. P. Surwade, S. Ammu, S. R. Agnihotra, S. Jain, K. E. Roberts, S. Park, R. S. Ruoff, S. K. Manohar. 2010. All-organic vapor sensor using inkjet-printed reduced graphene oxide. *Angewandte Chemie* 122(12): 2154-2157.

Eda, G. G. Fanchini, and M. Chhowalla. 2008. Large-area ultrathin films of reduced graphene oxide as a transparent and flexible electronic material. *Nature Nanotechnology* 3: 270-274.

Electronics Engineering Herald. 2006. Introduction and Application Areas for MEMS. www.eeherald.com/section/design-guide/mems_application_introduction.html. Last Accessed June 28, 2016.

Engel, J., N. Chen, C. Tucker, C. Liu, S. H. Kim, and D. Jones. 2006. Flexible multimodal tactile sensing system for object identification. Proceeding of the *5th IEEE Conference on Sensors,IEEE*: 563-566.

Fang, Z., Z. Zhao, Y. Wu, B. Zhang, and Y. Wang. 2004. Integrated temperature and humidity sensor-based MEMS. *Proceedings of the Information Acquisition, International Conference on IEEE*: 84-87.

Frank, O., G. Tsoukleri, I. Riaz, K. Papagelis, J. Parthenios, A. C. Ferrari, and C. Galiotis. 2011. Development of a universal stress sensor for graphene and carbon fibres. *Nature Communications* 2: 255.

Fu, X. W., Z. M. Liao, J. X. Zhou, Y. B. Zhou, H. C. Wu, R. Zhang, and D. Yu. 2011. Strain-dependent resistance in chemical vapor deposition grown graphene. *Applied Physics Letters* 99(21).

Hempel, M., D. Nezich, J. Kong, and M. Hofmann. 2012. A novel class of strain gauges based on layered percolative films of 2D materials. *Nano letters* 12(11): 5714-5718.

Hernandez, G. A., D. Martinez, C. Ellis, M. Palmer, and M. C. Hamilton. 2013. Through Si vias using liquid metal conductors for re-workable 3D electronics. *Proceedings of the 63rd Electronic Components and Technology Conference, IEEE*: 1401-1406.

Hu, H., K. Shaikh, and C. Liu. 2007. Super flexible sensor skin using liquid metal as interconnect. *Sensors, IEEE*: 815-817.
Jiang, S., X. Gong, X. Guo, and X. Wang. 2014. Potential application of graphene nano mechanical resonator as pressure sensor. *Solid State Communications* 193: 30-33.
Jing, Z., G. Y. Zhang, and D. X. Shi. 2013. Review of graphene-based strain sensors. *Chinese Physics B* 22(5).
Jobs, M., K. Hjort, A. Rydberg, and Z. Wu. 2013. A tunable spherical cap microfluidic electrically small antenna. *Small 9*(19): 3230-3234.
Kim, H. J., C. Son, and B. Ziaie. 2008. A multiaxial stretchable interconnect using liquid-alloy-filled elastomeric microchannels. *Applied Physics Letters 9*2(1).
Kim, J. H., S. M. Hong, J. S. Lee, B. M. Moon, and K. Kim. 2009. High-sensitivity capacitive humidity sensor with a novel polyimide design fabricated by MEMS technology. *Proceedings of the 4th IEEE International Conference on Nano/Micro Engineered and Molecular Systems (NEMS), IEEE*: 703-706.
Kim, W. G., J. S. Lee, D. G. Bucknall, W. J. Koros, and S. Nair. 2013. Nanoporous layered silicate AMH-3/cellulose acetate nanocomposite membranes for gas separations. *Journal of Membrane Science* 441: 129-136.
Kovac, M. G., D. Chleck, and P. Goodman. 1977. A new moisture sensor for in situ monitoring of sealed packages. *Proceedings of the 15th International Reliability Physics Symposium*: 85-91.
Kumar, P. 2012. Effect of colletor on electrospinning to fabricate aligned nano fiber. Ph.D. Dissertation, National Institute of Technology, Rourkela, India.
Laconte, J., V. Wilmart, J. P. Raskin, and D. Flandre. 2003. Capacitive humidity sensor using a polyimide sensing film. *Proceedings of the Symposium on Design, Test, Integration and Packaging of MEMS/MOEMS, IEEE*: 223-228.
Lawrence, M. G. 2005. The relationship between relative humidity and the dewpoint temperature in moist air: A simple conversion and applications. *Bulletin of the American Meteorological Society* 86(2): 225-233.
Lazarus, N., S. S. Bedair, C. C. Lo, and G. K. Fedder. 2010. CMOS-MEMS capacitive humidity sensor. *Journal of Microelectromechanical Systems*, 19(1): 183-191.
Lee, C., X. Wei, J. W. Kysar, and J. Hone. 2008. Measurement of the elastic properties and intrinsic strength of monolayer graphene. *Science* 321(5887): 385-388.
Li, Z., H. Zhang, W. Zheng, W. Wang, H. Huang, C. Wang, A. G. MacDiarmid, and Y. Wei. 2008. Highly sensitive and stable humidity nanosensors based on LiCl doped TiO2 electrospun nanofibers. *ACS Publications* 130(15): 5036-5037.
Lin, T. 2011. *Nanofibers - Production, Properties and Functional Applications*. InTech, Rijeka, Croatia.
Liu, W. W., B. Y. Xia, X. X. Wang, J. N. Wang. 2012. Exfoliation and dispersion of graphene in ethanol-water mixtures. *Material Science* 6:176-182.
Malshe, H., A. P. Malshe, and W. Jiang. 2011. Design, fabrication and testing of an electrospinning apparatus for the deposition of PMMA polymer for future biomedical applications. *Inquiry* 12: 70-76.
Maluf, N. 2000. *An Introduction to Microelectromechanical Systems Engineering*. Artech House, Boston, MA.

Mei, Q., and Z. Zhang. 2012. Photoluminescent graphene oxide ink to print sensors onto microporous membranes for versatile visualization bioassays. *Angewandte Chemie* 51: 5602-5606.

Mkhoyan, K. A., A. W. Contryman, J. Silcox, D. A. Stewart, G. Eda, C. Mattevi, S. Miller, and M. Chhowalla. 2009. Atomic and electronic structure of graphene oxide. *Nano Letters* 9(3): 1058-1063.

MEMS and Nanotechnology Exchange (MNX). (2016). What is MEMS Technology. www.mems-exchange.org/MEMS/what-is.html. Last Accessed June 28, 2016.

Morley, N. B., J. Burris, L. C. Cadwallader, and M. D. Nornberg. 2008. GaInSn usage in the research laboratory. *Review of Scientific Instruments* 79(5).

Pan, L., A. Chortos, G. Yu, Y. Wang, S. Isaacson, R. Allen, Y. Shi, R. Dauskardt, and Z. Bao. 2013. An ultra-sensitive resistive pressure sensor based on hollow-sphere microstructure induced elasticity in conducting polymer film. *Nature Communications* 5: 3002.

Pham, V. H., T. V. Cuong, S. H. Hur, E. W. Shin, J. S. Kim, J. S. Chung, and E. J. Kim. 2010. Fast and simple fabrication of a large transparent chemically converted graphene film by spray-coating. *Carbon* 48: 1945-1951.

Rahman, M. S. A., S. C. Mukhopadhyay, and P. L. Yu. 2014. *Novel sensors for food inspection: Modelling, fabrication and experimentation*. Springer International Publishing, Switzerland.

Shan, C., H. Yang, D. Han, Q. Zhang, A. Ivaska, and L. Niu. 2010. Graphene/AuNPs/chitosan nanocomposites film for glucose biosensing. *Biosens Bioelectron* 25(5): 1070-1074.

Shi, J., V. K. Hsiao, T. R. Walker, and T. J. Huang. 2008. Humidity sensing based on nanoporous polymeric photonic crystals. *Sensors and Actuators B: Chemical* 129(1): 391-396.

Shi, Q., N. Vitchuli, L. Ji, J. Nowak, M. McCord, M. Bourham, and X. Zhang. 2011. A facile approach to fabricate porous nylon 6 nanofibers using silica nanotemplate. *Journal of Applied Polymer Science* 120(1): 425-433.

So, J. H., and M. D. Dickey. 2011. Inherently aligned microfluidic electrodes composed of liquid metal. *Lab on a Chip* 11(5): 905-911.

Stankovich, S., D. A. Dikin, R. D. Piner, K. A. Kohlhaas, A. Kleinhammes, Y. Jia, Y. Wu, S. T. Nguyen, and R. S. Ruoff. 2007. Synthesis of graphene based nanosheets via chemical reduction of exfoliated graphite oxide. *Carbon* 45: 1558-1565.

Stankovich, S., R. D. Piner, S. T. Nguyen, and R. S. Ruoff. 2006. Synthesis and exfoliation of isocyanate-treated grapheneoxide nanoplatelets. *Carbon* 44: 3342-3347.

Starke, E., A. Türke, M. Krause, and W. J. Fischer. 2011. Flexible polymer humidity sensor fabricated by inkjet printing. *Proceedings of the 16th International Solid-State Sensors, Actuators and Microsystems Conference, IEEE*: 1152-1155.

Rotronic Instrument Corp. 2005. *The Rotronic Humidity Handbook*. Rotronic Instrument Corp., Hauppauge, NY.

Thomas, P., R. E. Ravindran, and K. B. R. Varma. 2012. Dielectric properties of Poly(methyl methacrylate) (PMMA)/$CaCu_3Ti_4O_{12}$ composites. *Proceedings of the 10th International Conference on the Properties and Applications of Dielectric Materials (ICPADM), IEEE:* 1-4.

Van Heeren, H., and P. Salomon. 2007. MEMS: Recent Developments, Future Directions. Electronics Enabled Products Knowledge Transfer Network, Wolfson School of Mechanical and Manufacturing Engineering, Loughborough University. www.lboro.ac.uk/microsites/mechman/research/ipm-ktn/pdf/Technology_review/mems-recent-developments-future-directions.pdf. Last Accessed June 28, 2016.

Wang, X., X. Li, L. Zhang, Y. Yoon, P. K. Weber, H. Wang, J. Guo, and H. Dai. 2009. N-doping of graphene through electro thermal reactions with ammonia. *Science* 324(5928):768-771.

Wang, Y., R. Yang, Z. Shi, L. Zhang, D. Shi, E. Wang, and G. Zhang. 2011. Super-elastic graphene ripples for flexible strain sensors. *ACS Nano* 5(5): 3645-3650.

Wu, A. T., and M. J. Brett. 2001. Sensing humidity using nanostructured SiO posts: mechanism and optimization. *Sensors and Materials*, 13(7): 399-431.

Yamada, T., Y. Hayamizu, Y. Yamamoto, Y. Yomogida, A. Izadi-Najafabadi, D. N. Futaba and K. Hata. 2011. A stretchable carbon nanotube strain sensor for human-motion detection. *Nature Nanotechnology* 6(5): 296-301.

Yang, S., P. Liu, M. Yang, Q. Wang, J. Song, and L. Dong. 2016. From flexible and stretchable meta-atom to metamaterial: A wearable microwave meta-skin with tunable frequency selective and cloaking effects. *Scientific Reports* 6: 21921.

Yao, Y., X. Chen, H. Guo, and Z. Wu. 2011. Graphene oxide thin film coated quartz crystal microbalance for humidity detection. *Applied Surface Science* 257: 7778-7782.

Yao, Y., X. Chen, H. Guo, Z. Wu, and X. Li. 2012a. Humidity sensing behaviors of graphene oxide silicon bi layer flexible structure. *Sensors and Actuators B: Chemical* 161: 1053-1058.

Yao, Y., X. Chen, J. Zhu, B, Zeng, Z. Wu, and X. Li. 2012b. The effect of ambient humidity on the electrical properties of graphene oxide films. *Nanoscale Research Letters* 7: 363.

Yao, Y., and W. Ma. 2014. Self-assembly of polyelectrolytic/graphene oxide multilayer thin films on quartz crystal microbalance for humidity detection. *IEEE Sensors Journal* 14: 4078-4084.

Zambrozi, P., and F. Fruett. 2012. Relative-air humidity sensing element based on heat transfer of a single micromachined floating polysilicon resistor. *Journal Integrated Circuits and Systems* 7(1): 130-136.

Zang, Y., F. Zhang, C. Di, and D. Zhu. 2015. Advances of flexible pressure sensors toward artificial intelligence and health care applications. 2: 140-156.

Zhang, B., Q. Dong, C. E. Korman, Z. Li, and M. E. Zaghloul. 2013a. Flexible packaging of solid-state integrated circuit chips with elastomeric microfluidics. *Scientific Reports* 3: 1098.

Zhang, Y., L. Zhang, and C. Zhou. 2013b. Review of chemical vapor deposition of graphene and related applications. *Accounts of Chemical Research* 46(10): 2329-2339.

Zhao, C. L., L. Xing, J. Xiang, and F. Li. 2014. Formation of uniform reduced graphene oxide films on modified PET substrates using drop-casting method. *Particuology* 17: 66-73.

Zhao, C. L., M. Qin, W. Li, and Q. Huang. 2011. Enhanced performance of a CMOS interdigital capacitive humidity sensor by graphene oxide. *Proceeding of the 16th International Solid-State Sensors, Actuators and Microsystems Conference, IEEE*.

Zhou, M., Y. Wang, Y. Zhai. J. Zhai. W. Ren, F. Wang, and S. Dong. 2009. Controlled synthesis of large-area and patterned electrochemically reduced graphene oxide films. *Chemistry: A European Journal* 15: 6116-6120.

APPENDIX A. LIST OF ABBREVIATIONS

AZ: One type of image reversal photoresist
CPMMA: Concentration of the precursor PMMA solution
CVD: Chemical vapor deposition
DC: Direct current
DI: Deionized
FRET: Fluorescence resonance energy transfer
rGO: Reduced graphene oxide
GO: Graphene oxide
HDMS: Hexamethyldisilazane
IBA: Isobornyl acrylate
IDEs: Interdigital microelectrodes
LCR meter: Inductance (L), capacitance (C), and resistance (R) meter
MEMS: Micro-electromechanical sensors and systems
MRC: Microelectronics Research Center at Iowa State University
PAA: Poly(acrylic acid)
PDDA: Poly(dimethyldiallyammonium) chloride
PDMS: Polydimethylsiloxane
PET: Polyethylene terephthalate
PIC: Planar interdigital capacitor
PMMA: Poly(methyl methacrylate)
PPC: Parallel plate capacitor
PSI: Pounds per square inch
QCM: quartz crystal microbalances
rGO: Reduced graphene oxide
RF: Radio frequency
RH: Relative humidity
SEM: Scanning electron microscopy
SSC: Spinning-assisted spray coating
SU-8: Epoxy-based negative photoresist
UV: Ultraviolet
WMS: Wireless MEMS multifunction sensor